Multi-scale hydro-mechanical modeling of coalbed methane recovery

Ahmad Mostafa

To cite this version:

Ahmad Mostafa. Multi-scale hydro-mechanical modeling of coalbed methane recovery. Civil Engineering. Université de Lorraine, 2023. English. NNT : 2023LORR0384 . tel-04718449

HAL Id: tel-04718449
https://hal.univ-lorraine.fr/tel-04718449v1

Submitted on 2 Oct 2024

Ecole doctorale Sciences et Ingénierie des Ressources Naturelles (SiReNa)

THESE DE DOCTORAT

Présentée et soutenue publiquement pour l'obtention du titre de

DOCTEUR DE l'UNIVERSITE DE LORRAINE

Mention : Mécanique et Génie Civil

Présentée par

Ahmad Nemer MOSTAFA

Sous la direction de : Fabrice GOLFIER et Luc SCHOLTES

Multi-scale hydro-mechanical modeling of coalbed methane recovery

Soutenance le 19 Décembre 2023

Membres du jury :

Directeurs de thèse:	M. Fabrice GOLFIER	Professeur, GeoRessources, Université de Lorraine
	M. Luc SCHOLTES	Maître de Conférences, LMV, Université Clermont-Auvergne
Président de jury :	M. Jacques PIRONON	DR CNRS, GeoRessources
Rapporteurs:	M. Matthieu VANDAMME	Professeur, NAVIER, École des Ponts ParisTech
	M. Frédéric DONZE	Professeur, ISTerre, Université Grenoble Alpes
Examinateurs:	M. Jacques PIRONON	DR CNRS, GeoRessources
	Mme. Laura BLANCO MARTIN	Maîtresse de Conférences, Centre de Geosciences, MINES ParisTech

Abstract

Nowadays, the increasing demand of energy, as well as the growing concerns about global warming, has resulted in a search for alternative energy sources. While considered a non-*renewable* energy resource, coalbed gas or coalbed methane (CBM) may contribute to this diversification and take part to the future energy mix. Currently, CBM is a valuable source of energy in the USA, China and Australia. The significant estimated gas reserves in Lorraine, in the northeast of France ($3.7\text{x}10^{11}$ m^3 against $2.3\text{x}10^{13}$ m^3 for the total USA CBM resources) represent an attractive and promising target for CBM exploitation, as highlighted by the REGALOR project. Based on the reuse of abandoned flooded coal mines, methane production is driven by the decrease of pore pressure in the coal seam during water pumping. Nevertheless, the sorption induced mechanisms at stake in coal reservoirs make CBM exploitation slightly more complex than in conventional hydrocarbon reservoirs, hence the need for better prediction tools able to describe all the processes involved.

The objective of this PhD thesis was to develop a conceptual and hydro-mechanically coupled numerical model giving a detailed description of methane desorption and gas transport within coal seams. Part of the difficulty is related to the highly complex multiscale nature of coal. Indeed, coal is a dual-porosity system characterized by a network of orthogonal fractures, so-called cleats, through which water and gas can percolate, as well as by a microporous matrix where methane is mainly trapped as an adsorbed layer and where diffusion prevails. Moreover, the matrix tends to swell or shrink as a result of sorption induced processes, adding therefore complexity to the already complex multi-physics processes at stake in such environment. The efficiency of methane recovery is thus driven by the coupling between gas flow dynamics with sorption/desorption mechanisms, as well as by compaction/deformation processes related to effective stress changes. Here, I propose a hydro-mechanical 3D pore-scale model combining a discrete element method (DEM) and a finite volume method (PFV) to investigate these coupled processes. The DEM is used to represent the solid phase as a collection of bonded particles while the PFV is used to simulate the transport processes at stake within the pore space, i.e., Knudsen and surface diffusions in the microporous matrix, and convection within the cleats. In addition, we included sorption on the solid particles. The PFV mesh is built upon a Delaunay triangulation of the particles centers with cleats identified as discrete interfaces. The model is coupled in the sense that it describes the deformations induced by pore pressure changes that, in turn, directly impact the hydraulic properties of the system. Sorption induced deformation is also taken into account through the definition of an additional pressure term, the so-called solvation pressure, which is directly related to sorbed quantities. Through different case studies, I was able to validate our model considering firstly the matrix by itself (Mostafa et al., Fuel, 2023), and, secondly, a cleat-matrix system (Mostafa et al., in prep.).

Résumé

De nos jours, la demande croissante en énergie, ainsi que les préoccupations grandissantes concernant le réchauffement climatique, ont conduit à la recherche de sources d'énergie alternatives. Bien que considéré comme une ressource énergétique non renouvelable, le gaz de houille ou le méthane de houille (CBM) peut contribuer à cette diversification et jouer un rôle dans le futur mix énergétique. Actuellement, le CBM est une source précieuse d'énergie aux États-Unis, en Chine et en Australie. Les importantes réserves de gaz estimées en Lorraine, dans le nord-est de la France ($3,7 \times 10^{11}$ m3 contre $2,3 \times 10^{13}$ m3 pour les ressources totales de CBM aux États-Unis) représentent une cible attrayante et prometteuse pour l'exploitation du CBM, comme le souligne le projet REGALOR. Basée sur la réutilisation des anciennes mines de charbon inondées, la production de méthane est stimulée par la baisse de la pression des pores dans le gisement de charbon lors du pompage de l'eau. Néanmoins, les mécanismes induits par la sorption dans les réservoirs de charbon rendent l'exploitation du CBM légèrement plus complexe que dans les réservoirs d'hydrocarbures conventionnels, d'où la nécessité de meilleurs outils de prédiction capables de décrire tous les processus impliqués.

L'objectif de cette thèse de doctorat était de développer un modèle numérique conceptuel couplé hydro-mécaniquement fournissant une description détaillée de la désorption du méthane et de la récupération du gaz dans les couches de charbon. Une partie de la difficulté est liée à la nature multi-échelle hautement complexe du charbon. En effet, le charbon est un système à double porosité caractérisé par un réseau de fractures orthogonales, appelées *cleats* en anglais, à travers lesquelles l'eau et le gaz peuvent percoler, ainsi que par une matrice microporeuse où le méthane est principalement piégé sous forme de couche adsorbée et où la diffusion prédomine. De plus, la matrice a tendance à se dilater ou à se contracter en raison des processus induits par la sorption, ajoutant ainsi de la complexité aux processus multi-physiques déjà complexes en jeu dans un tel environnement. L'efficacité de la récupération du méthane est donc déterminée par le couplage entre la dynamique de l'écoulement du gaz et les mécanismes de sorption/désorption, ainsi que par les processus de compression/déformation liés aux variations de contrainte effective. Ici, je propose un modèle à l'échelle des pores en 3D couplant une méthode des éléments discrets (DEM) et une méthode de volume à l'échelle des pores (PFV) pour étudier ces processus couplés. Le DEM est utilisé pour représenter la phase solide comme une collection de particules liées, tandis que le PFV est utilisé pour simuler les processus de transport en jeu dans l'espace poreux, c'est-à-dire les diffusions de Knudsen et de surface dans la matrice microporeuse, ainsi que la convection dans les fractures. De plus, nous avons inclus la sorption sur les particules solides. Le maillage PFV est construit sur la base d'une triangulation de Delaunay des centres des particules, avec les fractures identifiés comme des interfaces discrètes. Le modèle est couplé dans le sens où il décrit les déformations induites par les changements de pression des pores qui, à leur tour, ont un impact direct sur les propriétés hydrauliques du système. La déformation induite par la sorption est également prise en compte grâce à la définition d'un terme de pression supplémentaire, appelé pression de solvation, qui est directement lié aux quantités adsorbées. À travers différentes études de cas, j'ai pu valider ce modèle en considérant d'abord la matrice seule (Mostafa et al., Fuel, 2023), et, ensuite, un système fracture-matrice (Mostafa et al., en préparation).

Acknowledgment

I am deeply honored to extend my heartfelt gratitude to my esteemed supervisors, Professor Fabrice GOLFIER and Dr. Luc SCHOLTES, for their unwavering support and invaluable guidance that have been instrumental in the successful completion of my thesis journey. Without their profound understanding, boundless patience, and active involvement at every stage of this process, this achievement would have remained an elusive dream. I am profoundly thankful for the wealth of knowledge I have acquired from them over the years, particularly in the fields of Geosciences, Hydrogeology, and Geomechanics.

Words truly fail to convey the depth of my gratitude for their willingness to oversee my PhD thesis, their responsiveness to my inquiries, even during the late hours of the night, and their constant encouragement to maintain scientific rigor in the analysis and conclusions. Their insightful feedback has been instrumental in refining my thought processes, shaping my methodology, and fine-tuning the results and composition of this final thesis report for the defense.

I would also like to extend my heartfelt thanks to the Regalor project (Ressources Gazières de Lorraine) for their invaluable financial support, which has made this work possible. Additionally, I wish to express my profound appreciation to the esteemed members of the Jury for their willingness to review the manuscript and evaluate this work.

Furthermore, I want to extend my sincere gratitude to all my colleagues and friends at HGM-Georessources for their steadfast support, the memorable moments of camaraderie, shared laughter, and the enjoyment of delicious meals and coffee breaks. This appreciation extends to all those with whom I've had the privilege of forming connections during my time here and throughout the progress of this work.

Lastly, I would like to offer my deepest gratitude to my family for their unwavering trust, boundless support, and fervent prayers throughout this journey. I am profoundly grateful for my spouse, whose unwavering support has been a constant source of strength. I see the glow of pride in her eyes, and I am unable to adequately express my love for her and my immense pride in her.

Contents

Table of Figure

Résumé en français

i. Contexte général de la thèse

La demande mondiale en énergie ne cesse de croître à mesure que la population augmente, et il existe une forte corrélation entre le mode de vie et la consommation d'énergie (Administration de l'information sur l'énergie des États-Unis, 2010). Par exemple, si les États-Unis consomment actuellement 20 % de l'énergie mondiale, on peut en déduire que leur demande en énergie serait considérablement plus élevée si leur population atteignait 450 millions dans le futur.

Les combustibles fossiles ont été une source d'énergie durable pour l'humanité, issus de la matière organique décomposée de plantes et d'animaux qui ont été enfouis et soumis à la chaleur et à la pression pendant des millions d'années. Ces combustibles, contenant du carbone et de l'hydrogène, se trouvent dans la croûte terrestre et sont brûlés pour produire de l'énergie.

Les économies des pays développées sont toutefois de plus en plus préoccupées par la pollution causée par la combustion des combustibles fossiles et l'augmentation subséquente des émissions de dioxyde de carbone (CO2), qui contribuent significativement au changement climatique mondial. En conséquence, ces pays cherchent de nouvelles sources d'énergie plus propres. Par exemple, les nations européennes visent à augmenter progressivement leur utilisation d'énergie renouvelable pour réduire leurs émissions de CO2. Cependant, l'utilisation de sources d'énergie renouvelable telles que l'énergie solaire et éolienne en mer est nettement plus coûteuse par rapport à l'utilisation du charbon, et ces sources ne peuvent être produites que de manière intermittente (Maradin, 2021 ; Ringel, 2006 ; Administration de l'information sur l'énergie des États-Unis, 2010). Cela soulève des questions de stabilité économique et de rentabilité, car des factures d'énergie plus élevées peuvent dissuader les entreprises d'investir dans des sources d'énergie plus coûteuses, mais plus propres. Les crises géopolitiques récentes qui ont conduit à une hausse brutale du pétrole et du gaz ont accentué aussi le besoin de souveraineté énergétique et de comment planifier la transition vers les énergies renouvelables.

Face aux défis posés par l'équilibre entre la stabilité économique et la protection de l'environnement, de nouvelles approches sont développées dans le monde entier. Parmi ces approches, les formations de charbon font l’objet d’un renouveau d’intérêt. La récupération améliorée du méthane des gisements de charbon (ECBM) qui consiste à injecter du gaz CO2 dans le charbon afin d'améliorer l'extraction du méthane tout en réduisant les émissions de CO2,est une des pistes qui peut contribuer à cette réflexion. Cette approche vise à offrir une solution viable et plus respectueuse de l’environnement qui puisse satisfaire à la fois les partisans des énergies renouvelables tout en permettant l’exploitation des ressources du sous-sol à un coût acceptable. D’autre part, le stockage souterrain d'hydrogène dans les veines de charbon est considéré comme une option pour le stockage de l'hydrogène à grande échelle compte tenu de la structure des micro/nano-pores du charbon qui peut adsorber une énorme quantité de gaz (dont l'hydrogène) et qui peut être retirée en cas de besoin.

De toute évidence, les processus impliqués dans ces techniques d’exploitation ou de stockage sont assez complexes et exigent une meilleure compréhension de la physique générale régissant la réponse du charbon aux phénomènes induits par la sorption (c'est-à-dire le gonflement et le rétrécissement) résultant de l'écoulement et du transport des gaz dans ses pores. À travers ce travail de thèse, nous visons à obtenir une compréhension plus complète du comportement hydromécanique du charbon lorsqu'il est soumis à l'écoulement et au transport de gaz.

En conclusion, l'utilisation des combustibles fossiles continue de jouer un rôle important dans la satisfaction de la demande mondiale en énergie, représentant plus de 80 % de la consommation mondiale actuelle d'énergie (Furfari, 2017). Pour prendre des décisions éclairées, il convient d'examiner attentivement les préoccupations concernant la stabilité économique et la protection de l'environnement. La recherche de doctorat proposée vise à fournir des informations qui pourraient éventuellement équilibrer ces deux facteurs importants.

ii.Récupération du méthane des gisements de charbon

La récupération du méthane des gisements de charbon (CBM) devient de plus en plus populaire en tant que source d'énergie en raison de ses propriétés de combustion propre et du potentiel de réduction des émissions de gaz à effet de serre. Dans le charbon, le méthane est essentiellement piégé sous forme d'une couche adsorbée sur la phase solide à l'intérieur des blocs de matrice qui sont entourés par un réseau de fractures saturées d'eau appelées claves (Figure 1) (Harpalani and Chen, 1997 ; Lu and Connell, 2007 ; Warren and Root, 1963).

Le processus d'extraction implique la mobilisation de l'eau dans le réseau de claves pour désorber le méthane de la matrice de charbon, afin de le drainer vers le puits. Lorsque le gaz est piégé dans des réservoirs non conventionnels tels que les gisements de charbon, il ne peut pas être récupéré efficacement à l'aide de méthodes de drainage traditionnelles. Au lieu de cela, de nouvelles technologies doivent être utilisées pour collecter le gaz à partir de zones inaccessibles. Deux stratégies couramment utilisées pour augmenter l'extraction de gaz sont la fracturation hydraulique et l'amélioration de la récupération du gaz (EGC).

- Fracturation hydraulique :

Dans le processus de fracturation hydraulique, le puits est rempli d'un mélange d'eau, de sable et de produits chimiques soumis à une forte pression. Cette pression provoque la fracture de la roche environnante, créant un réseau de fissures. Bien que considérée comme une technique efficace pour augmenter la production de gaz, la fracturation hydraulique a été associée à plusieurs impacts négatifs potentiels, tels que la contamination des sols et de l'eau, la pollution environnementale, voire des tremblements de terre. Par exemple, des études ont documenté des cas de contamination élevée des sols et de l'eau à haut risque, ainsi que de la pollution environnementale dans l'État de New York et des tremblements de terre dans le nord-est de l'Arkansas (Eaton, 2013 ; Ewen et al., 2012 ; Horton, 2012 ; Sang et al., 2014). Il est essentiel de comprendre que, bien que la fracturation hydraulique soit considérée comme une méthode efficace pour augmenter la production de gaz, il est également important de prendre en considération les conséquences possibles de cette technique sur l'environnement et les communautés locales. Malgré la maîtrise de tous les risques potentiels, le forage de 300 puits et la réalisation de 4 000 opérations de fracturation hydraulique pour le gaz de schiste consommeront toujours une quantité importante d'eau, estimée à environ 6 millions de mètres cubes (Ewen et al., 2012). Pour mettre cela en perspective, cette quantité d'eau équivaut à la consommation annuelle d'eau d'une ville de 165 000 habitants, telle qu'Osnabrück. Il est important de noter que ce processus d'extraction à grande échelle a le potentiel d'avoir un impact significatif sur les ressources en eau locales et sur l'environnement.

- Amélioration de la récupération du gaz (EGC) :

L'ECBM est un type d'EGC qui désigne la récupération du méthane à partir des couches de charbon par injection de gaz plutôt que d'eau uniquement. L'ECBM implique généralement l'injection de CO2 dans le gisement de charbon pour déplacer l'eau de manière plus efficace et désorber davantage de méthane de la matrice (Figure 2). Le CO2 est plus efficace que l'azote ou l'air dans ce processus en raison de sa densité plus élevée et de sa solubilité accrue dans l'eau (Bertrand et al., 2017 ; Ottiger et al., 2008 ; Vandamme et al., 2010 ; Wu et al., 2010). Par rapport à d'autres formes d'EGC, l'ECBM a le potentiel d'être une alternative plus respectueuse de l'environnement car le CO2 peut être capturé et stocké dans le gisement de charbon grâce à la technologie de capture et de stockage du carbone (CSC), réduisant ainsi l'empreinte carbone du processus d'extraction.

iii. Le CBM dans le monde

Le CBM a acquis une importance mondiale, comme le montre la présence de sites opérationnels de CBM dans différents pays, notamment le Canada, l'Australie, l'Inde et la Chine (Figure 3).

Le bassin de San Juan aux États-Unis abrite certains des plus grands producteurs de CBM, notamment BP et ConocoPhillips. BP seul exploite plus de 1500 puits dans la région, tandis que ConocoPhillips en possède plus de 800 en production. Ces puits sont utilisés pour extraire du gaz naturel des couches de charbon, et le bassin de San Juan est particulièrement attrayant pour la production de CBM en raison de ses importantes réserves de charbon et de la teneur élevée en gaz dans le charbon. L'infrastructure existante de la région et son réseau de pipelines bien développé facilitent également le transport du gaz extrait vers d'autres parties du pays, ce qui permet à BP et ConocoPhillips de s'imposer comme des acteurs majeurs de l'industrie du CBM aux États-Unis, avec des réserves importantes et des capacités de production étendues (pour plus de détails, voir (Ayers, 2002 ; Palmer, 2010 ; Pashin, 2014)).

En Australie, les réserves de charbon faciles à exploiter ont maintenu artificiellement bas le prix du gaz, rendant difficile la concurrence du méthane de gisement de charbon (CBM). Cependant, les grandes entreprises énergétiques se sont depuis regroupées avec des entreprises locales de CBM et ont annoncé la construction de plusieurs usines de gaz naturel liquéfié (GNL) destinées à l'exportation vers des pays tels que le Japon, ce qui a contribué à augmenter le prix du gaz CBM et à renforcer l'industrie. Les champs de CBM en Australie avec une perméabilité plus élevée ont le potentiel de produire des quantités importantes de gaz, le puits le plus productif produisant environ 12 millions de pieds cubes par jour. Pour maximiser le rendement des puits de CBM, les opérateurs ont fait preuve de polyvalence pour trouver les meilleures pratiques en matière de complétions, y compris des techniques telles que le ré-entoilage, la création de cavités, la fracturation à l'eau et le forage horizontal en strate superficielle. Ces approches font du CBM une source d'énergie plus compétitive sur le marché australien (pour plus de détails, voir (Australie, 2014 ; Faiz et Hendry, 2006 ; Freij-Ayoub, 2012 ; Palmer, 2010)).

Les données sur la production de méthane de gisement de charbon (CBM) en Chine sont difficiles à obtenir et souvent peu fiables. Cependant, il est largement admis que des milliers de puits de développement ont été forés dans le pays, bien que l'utilisation commerciale du gaz soit plus localisée par rapport à d'autres pays disposant de réseaux de pipelines de CBM plus importants. La production de CBM en Chine est principalement issue des charbons de rang élevé dans les bassins d'Ordos et de Qinshui, qui se trouvent dans différentes régions du pays. Les données de production de CBM rapportées sont considérées comme indicatives au mieux, les rapports de presse généraux indiquant que la production de CBM était légèrement supérieure à 1 milliard de pieds cubes en 2006 et a augmenté à 51 milliards de pieds cubes en 2010. Ces réservoirs sous-estiment probablement la production réelle et ne reflètent peut-être que le taux d'augmentation des grands projets de production de CBM en Chine au cours des cinq dernières années. Malgré les difficultés à obtenir des données fiables, la production de CBM en Chine devrait augmenter de manière significative en raison des vastes ressources de charbon du pays et de la demande croissante en énergie, ce qui pourrait rivaliser avec d'autres pays producteurs majeurs de CBM dans le monde (pour plus de détails, voir (Ewen et al., 2012 ; Fuyuan Mu et al., 2015 ; Moore, 2012 ; Palmer, 2010)).

iv.Le CBM en Lorraine

Les gisements de charbon dans la région de Lorraine sont restés inexploités depuis la fermeture de la mine de Houve en 2004. Cependant, la région renferme toujours d'abondantes ressources en gaz naturel, y compris le CBM.

Des études initiales menées par IFP Énergies Nouvelles ont estimé en 2013, sur la base des données de La Française de l'Énergie, que 370 milliards de mètres cubes de gaz de charbon étaient enfouis sous nos pieds. Une deuxième étude a été réalisée par l'Institut allemand de recherche sur l'énergie et l'environnement (IFEU). Le rapport de 2016 a estimé que l'empreinte carbone du gaz de charbon était 10 fois plus faible que celle du gaz actuellement importé.

L'exploration de la récupération de CBM en Lorraine (France) s'inscrit dans la tendance mondiale de recherche de gaz naturel non conventionnel. On s'attend à ce que ces ressources servent de solution de transition vers une économie à faible émission de carbone où les sources d'énergie renouvelable prédomineront.

Piégé dans les couches de charbon inondées de Lorraine, plus de 95 % de ce gaz est du méthane. Les mouvements tectoniques ont complètement fragmenté le sous-sol lorrain (Figure 3). Le gaz peut donc s'échapper des veines sans fracturation hydraulique, mais en pompant l'eau (Figure 4).

v.Projet Regalor

Le projet Regalor a été lancé en 2012 à l'initiative de la région Grand Est et a bénéficié d'un soutien financier du Fonds européen de développement régional (FEDER). Le projet est dirigé par le laboratoire GeoRessources (Université de Lorraine - CNRS) et est réalisé en partenariat avec une entreprise mosellane, La Française de l'Énergie. Il s'agit d'une opportunité unique pour les scientifiques de collaborer avec les industriels et de fournir des orientations avant le début éventuel des opérations d'extraction.

L'objectif du projet est d'évaluer la viabilité de l'extraction de gaz de charbon dans la région de Lorraine, en mettant l'accent sur les impacts environnementaux, territoriaux et sociaux associés, afin de prendre une décision éclairée à la fin du projet. Les résultats du projet sont censés assurer une bonne intégration territoriale de l'exploitation, de la perception sociale aux opportunités de réindustrialisation.

vi.Motivation Objectifs du travail dethèse et méthodologie proposée

Le potentiel de gonflement du charbon est un facteur crucial à prendre en compte lorsqu'il s'agit de la récupération du méthane des gisements de charbon, car il induit des évolutions de perméabilité qui sont propres au réservoir de charbon (Figure 8).

La capacité de prédire avec précision le comportement du charbon lors des processus d'injection et d'extraction de gaz est essentielle pour l'extraction réussie et efficace du méthane des gisements de charbon (CBM). Afin de réaliser une analyse économique appropriée de la récupération améliorée du méthane des gisements de charbon (ECBM), il est nécessaire d'avoir des projections précises des taux d'injection de CO2 et d'extraction de CH4, ce qui ne peut être réalisé qu'en utilisant un modèle approprié.

Ce modèle doit tenir compte de la variabilité de l'injectivité observée sur le terrain et décrire avec précision le gonflement qui se produit en raison de l'adsorption. Malheureusement, de nombreuses études expérimentales menées pour mieux comprendre le comportement du charbon lors de l'injection et de l'extraction de gaz sont incomplètes et n'estiment pas complètement tous les paramètres impliqués (comme décrit dans les études de Day et al., 2008b ; Ottiger et al., 2008 ; Robertson et Christiansen, 2005). Cela est dû à la nature complexe du comportement du charbon, qui résulte de l'interaction entre différents processusphysico-chimiques et réponses hydro-mécaniques.

Les mécanismes de transport qui déplacent les molécules de gaz à travers les espaces poraux du système de charbon, ainsi que le comportement résultant de l'isotherme d'adsorption et de sa déformation induite par le gonflement, sont quelques-uns des facteurs qui rendent difficile la compréhension complète du comportement du charbon. L'isotherme d'adsorption et la déformation induite par le gonflement jouent un rôle important dans l'affectation de la perméabilité du système, et il est important de prendre en compte ces facteurs lors de la création d'un modèle de réservoir approprié. Le défi de comprendre pleinement et de prédire le comportement des réservoirs de charbon lors de l'injection et de l'extraction de gaz souligne l'importance de la recherche continue et de l'expérimentation dans ce domaine.

Pour approfondir notre compréhension du comportement du charbon, notre objectif initial est de décrire le charbon en tant que matériau au chapitre 2, en fournissant une revue exhaustive de la littérature sur son comportement et les différents processus physiques impliqués dans ses réponses hydromécaniques lorsqu'il est soumis à l'écoulement de gaz. Ensuite, nous présenterons les différentes approches numériques proposées pour modéliser son comportement hydromécanique.

Le chapitre 3 se concentre sur notre approche proposée pour modéliser le comportement hydromécanique de la matrice de charbon. Nous présenterons l'approche de modélisation basée sur le couplage d'une méthode des éléments discrets (DEM) avec une méthode de volume fini à l'échelle des pores (PFV), où nous avons mis en œuvre les mécanismes de transport et les processus de déformation induite par l'adsorption. Nous montrerons comment nous avons validé le modèle et comment ses prédictions se comparent aux observations expérimentales. Nous montrerons également que le modèle peut être utilisé pour étendre davantage nos connaissances sur la réponse du charbon en termes de dynamique.

Au chapitre 4, l'accent sera mis sur le système de fractures dans le charbon et la combinaison des échelles de fractures et de matrice. L'objectif de ce chapitre est de se concentrer sur l'échange de flux entre les fractures et la matrice et sur l'évolution de la perméabilité des fractures en tenant compte du gonflement et du rétrécissement de la matrice de charbon et de l'évolution des concentrations de gaz à travers la matrice et les claves. La loi de Darcy est prise en compte à travers les fracturess et divers mécanismes de transport à travers la matrice. Les résultats de cette analyse fourniront des informations précieuses sur le comportement des réservoirs de méthane des gisements de charbon et orienteront vers des stratégies améliorées pour la récupération améliorée du gaz.

La dernière section de notre travail sera consacrée à la démonstration des conclusions et des travaux futurs qui amélioreront le modèle.

vii. Principaux résultats

Les principaux résultats de ce travail, qui constituent le cœur des Chapitres 3 et 4, sont le développement de modèles couplées à l'échelle de la matrice de charbon tout d'abord puis du charbon fracturé. Ils sont résumés ci-dessous.

Modèle hydro-mécanique à l'échelle de la matrice du charbon

Nous avons tout d'abord développé modèle 3D couplant un modèle à éléments discrets et un modèle de réseau de pores spécifiquement développé pour décrire les différents mécanismes de diffusion en jeu dans la matrice de charbon ainsi que les déformations associées induites par l'adsorption. Le matériau est supposé être saturé en gaz et la diffusion se produit par la combinaison de la diffusion de Knudsen dans l'espace poreux, de la diffusion de surface au niveau des grains et de l'adsorption-désorption à l'interface gaz-solide. Le modèle est couplé hydro-mécaniquement dans le sens où les changements dans la pression des pores produisent des forces hydrostatiques qui déforment le squelette solide, tandis que la déformation de l'espace des pores induit des changements dans la pression des pores qui favorisent l'écoulement entre les pores. Les déformations induites par la sorption sont prises en compte en considérant un terme de pression supplémentaire lié à la concentration de gaz dans le milieu (la pression dite de solvatation). Les modèles de transport mis en œuvre sont tout d'abord vérifiés par rapport aux solutions analytiques décrivant la diffusion dans les milieux poreux avec et sans sorption-désorption, et une comparaison est faite avec une expérience de gonflement réalisée sur un spécimen de charbon pour illustrer la pertinence de l'approche proposée pour décrire la déformation induite par l'adsorption. Il résulte de cette première partie que le nouveau modèle proposé à l'échelle du pore offre un moyen précis d'évaluer la déformation induite par la sorption de la matrice de charbon et contribue à la compréhension des mécanismes en jeu durant l'exploitation du CBM. Le travail réalisé à fait l'objet d'une publication parue dans *Fuel*.

Modèle hydro-mécanique à l'échelle de l'échantillon de charbon fracturé

D'une manière générale, le charbon peut être décrit comme un système à double porosité, les fractures régissant la perméabilité globale du charbon et les micropores de la matrice abritant les processus de diffusion tels que la diffusion de Knudsen, l'adsorption/désorption et la diffusion de surface. Par exemple, lors d'un scénario d'injection, le gaz s'écoule typiquement à travers les fractures, se diffuse dans la matrice du charbon, puis se fixe sur la phase solide, ce qui entraîne un gonflement de la matrice. Afin d'étendre notre modèle, nous avons considéré que le méthane est présent partout au début de la simulation, ce qui se traduit par un écoulement monophasique dans le système de fractures.

Le comportement des fractures est régi par les mêmes lois d'élasticité-cohésivité-friction que celles utilisées pour la matrice Dans le présent travail, nous nous contentons d'attribuer des propriétés spécifiques aux liaisons constituant les fractures. Ce choix permet de définir l'extension transversale des fracturess sur plusieurs couches de particules au lieu de deux seulement avec la logique de contact lisse. Dans ce cas, les particules situées à l'intérieur d'une fracture sont simplement considérées comme des points matériels qui ne participent pas au schéma de transport de masse tout en assurant la réponse mécanique de la discontinuité. Le transport de masse s'effectue à l'intérieur des fractures par advection entre les pores des fractures, et entre les fractures et la matrice par une combinaison de diffusion de Knudsen entre les pores des fractures et les pores de la matrice, et d'adsorption/désorption entre les pores des fractures et les particules solides de la matrice. Enfin, les fractures peuvent s'ouvrir et se fermer mécaniquement grâce au réseau de contact reliant leurs parois opposées. Les résultats obtenus montrent un comportement cohérent du modèle en termes de réponse mécanique (déformation) et hydraulique (évolution de la perméabilité).

Chapter 1

Introduction

Chapter 1 : Introduction

1.1.General context

The world's energy demand is continuously growing as the population increases, with there being a strong correlation between lifestyle and energy consumption (U.S. Energy information administration, 2010). For instance, if the United States currently consumes 20% of the world's energy, it can be inferred that its energy demand would be significantly higher if its population were to reach 450 million in the future.

Fossil fuels have been a longstanding source of energy for mankind, derived from the decomposed organic matter of plants and animals that have been buried and subjected to heat and pressure over millions of years. These fuels, containing carbon and hydrogen, are found in the earth's crust and are combusted for energy generation.

Developed economies are facing growing concerns over pollution caused by the combustion of fossil fuels and the resulting increase in carbon dioxide (CO_2) emissions, which drastically contribute to global climate change. As a result, these countries are seeking new, cleaner energy sources. For example, European nations aim to increase their use of renewable energy over time to reduce their CO_2 emissions. However, the use of renewable energy sources such as solar and offshore wind power is significantly more expensive compared to the use of coal, and these sources can only be produced intermittently (Maradin, 2021; Ringel, 2006; U.S. Energy information administration, 2010). This leads to questions of economic stability and cost-effectiveness, as higher energy bills may deter businesses from investing in the more expensive, yet cleaner, energy sources. The recent geopolitical crises that have led to a sharp rise in oil and gas prices have also accentuated the need for energy sovereignty and how to plan the transition to renewable energies.

Given the challenges posed by balancing economic stability and environmental protection, new innovative ways of producing and storing energy are being developed around the world with a renewed interest in coal formations. Indeed, enhanced coal bed methane (ECBM) recovery consists in injecting CO_2 gas into coal so as to enhance methane extraction while reducing CO_2 emissions. This approach seeks to offer a viable and environmental-friendly energy production solution while allowing underground resources to be exploited at an acceptable cost. Another promising use of coal formations is for the underground storage of hydrogen. Coal seams are seen as a suitable option for large-scale hydrogen storage, given the micro/nano-pore structure of coal, which can adsorb huge quantities of gas (including hydrogen) and be withdrawn when needed (Keshavarz et al., 2022). Obviously, theses exploitation or underground storage techniques are rather complex and demand for a better understanding of the overall physics governing the coal response to sorption induced phenomena (i.e., swelling and shrinkage) resulting from the flow and transport of gases within its pores.

In conclusion, the utilization of fossil fuels still plays a significant role in meeting the world's energy demand, accounting for more than 80% of the current global energy consumption (Furfari, 2017). To make informed decisions, both the economic stability and environmental protection concerns should be thoroughly examined, in conjunction with a better understanding of the physical processes involved. The proposed PhD research aims to provide insights into the latter that could eventually balance these two important concerns.

1.1.1.Coal bed methane recovery

In coal, methane is basically trapped as an adsorbed layer on the solid phase within the matrix blocks that are surrounded by a network of water saturated fractures called cleats (Figure 1) (Harpalani and Chen, 1997; Lu and Connell, 2007; Warren and Root, 1963).

The extraction process involves mobilizing water in the cleat network to desorb methane from the coal matrix, so as to drain it toward the wellbore. When gas is trapped in unconventional reservoirs such as coalbeds, traditional pumping methods can be somewhat limited. Hence, new technologies may be used to collect gas from inaccessible areas. These technologies aim to increase methane production by enhancing rock permeability or gas desorption. Two commonly used strategies for increasing gas extraction are rock stimulation (including fracking banned in France since 2011) and Enhanced Gas Recovery (EGC).

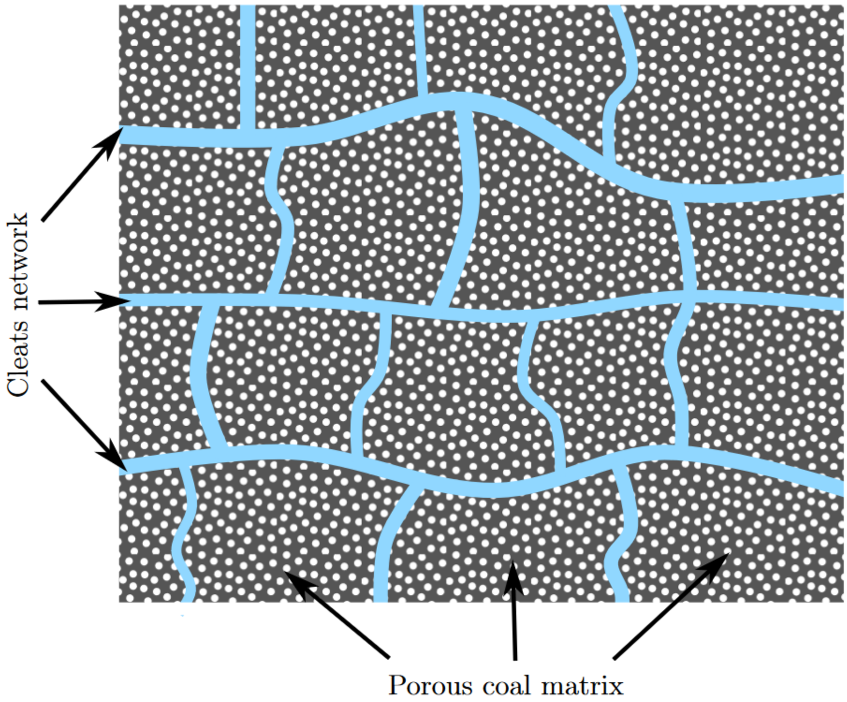

Figure 1 A conceptual representation of a coal seam (adapted from (Brochard et al., 2011)).

- Fracking:

Although coal is a naturally highly fractured rock, unlike very compact formations as shales, rock stimulation techniques (including hydraulic fracturing or “hydrofracking”) may be necessary to optimize the volume of coal seam gas extracted. This rock stimulation techniques aims to increase gas desorption which varies according to the permeability of the medium. In the hydrofracking process, the wellbore is filled with a mixture of water, sand, and chemicals that is subjected to high pressure. This pressure causes the surrounding rock to fracture, creating a network of fractures where fluid can percolate more easily. Despite being considered as an effective technique for increasing gas production, hydrofracking has also been associated with several potential negative impacts, such as soil and water contamination, environmental contamination, and even earthquakes. For example, studies have documented instances of high-risk soil and water contamination, as well as environmental contamination in New York, and earthquakes in north-central Arkansas (Eaton, 2013; Ewen et al., 2012; Horton, 2012; Sang et al., 2014). It is thus crucial to understand that while hydrofracking has been seen as an effective method for boosting gas output, it is also important to take into consideration the possible consequences of the technique on the environment and local communities. In addition to all the potential risks, hydrofracking operations for shale gas need a significant amount of water (Ewen et al., 2012) which has the potential to significantly impact the local water resources and the environment. In coal seams, however, hydraulic fracturing is not necessarily needed, unlike in shale reservoirs. As with deep geothermal energy, it is possible to stimulate the already existing fractures within the coal seam without the need to create new fractures in the rock.

- Enhanced Gas Recovery (EGC):

ECBM is type of EGC that refers to the recovery of methane from coal seams through the injection of gases instead of water only. ECBM usually involves injecting CO2 into the coalbed to displace water more efficiently and to desorb more methane from the matrix (Figure 2). CO2 is more effective than nitrogen or air in this process due to its higher density and increased solubility in water (Bertrand et al., 2017; Ottiger et al., 2008; Vandamme et al., 2010; Wu et al., 2010). Compared to other forms of ECG, ECBM has the potential to be a more environmentally friendly alternative because CO2 can be captured and stored in the coalbed using carbon capture and storage (CCS) technology, reducing therefore the carbon footprint of the extraction process.

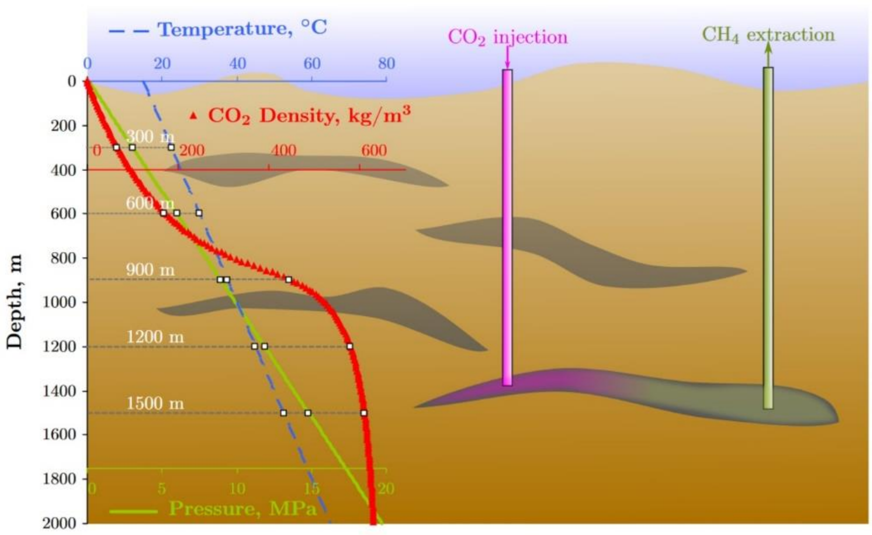

Figure 2 CO2 injection improves coal bed methane recovery (Brochard et al., 2011).

.

1.1.2.Underground hydrogen storage in coal bed formations

A more recent but growing interest in coal bed formations is due to their potential use as reservoirs for hydrogen storage. Indeed, hydrogen underground storage (UHS), where H_2 is stored in underground geological formations, e.g. salt caverns or depleted oil and gas reservoirs, is a key step towards the hydrogen economy to replace fossil fuels. Recent studies have highlighted the suitability of coal formations for geological hydrogen storage due to coal adsorption properties and its specific hydrogen affinity (Keshavarz et al., 2022)

1.1.3.CBM Worldwide

CBM has gained worldwide importance, as demonstrated by the appearance of operational CBM sites in various countries, including Canada, Australia, India, and China (Figure 3).

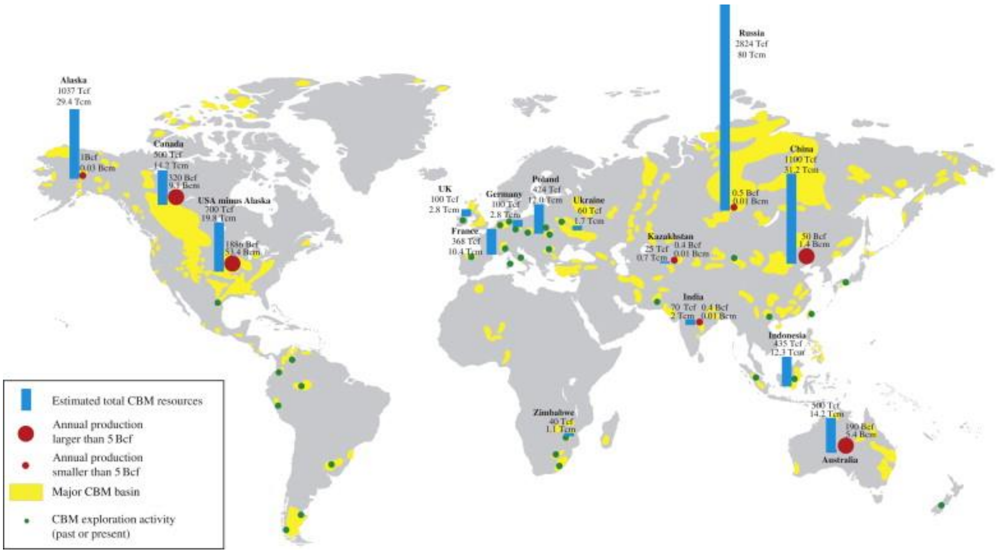

Figure 3 CBM resources worlwide (https://www.sciencedirect.com/topics/earth-and-planetary-sciences/coal-bed-methane-resource)

The San Juan basin in the United States is home to some of the biggest CBM producers, including BP and ConocoPhillips. BP alone operates over 1500 wells in the region, while ConocoPhillips possesses over 800 producing wells. These wells are used to extract natural gas from coal seams, and the San Juan basin is particularly attractive for CBM production due to its large coal deposits and the high gas content in the coal. The region's existing infrastructure and well-developed pipeline network also make it easier and more cost-effective to transport the extracted gas to other parts of the country. As a result, BP and ConocoPhillips have been able to establish themselves as major players in the CBM industry in the United States, with significant reserves and extensive production capabilities (for more details see (Ayers, 2002; Palmer, 2010; Pashin, 2014)).

In Australia, easy-to-mine coal reserves kept the price of gas artificially low, making it difficult for Coalbed Methane (CBM) to compete. However, major energy companies have since merged with local CBM companies and announced the construction of several Liquefied Natural Gas (LNG) plants for export to countries such as Japan, which has helped to raise the price of CBM gas and bolster the industry. CBM fields in Australia have the potential to produce significant amounts of gas, with the most productive well producing around 12 million cubic feet per day. To maximize the yield of CBM wells, operators have been versatile in finding best practices for completions, including techniques such as under-reaming, creating cavities, water fracking, and surface-in-seam horizontal drilling. These approaches make CBM a more competitive source of energy in the Australian market (for more details see (Australia, 2014; Faiz and Hendry, 2006; Freij-Ayoub, 2012; Palmer, 2010)).

Data on CBM production in China is difficult to obtain and often unreliable. However, it is widely believed that thousands of wells have been drilled in the country, although the commercial use of the gas is localized compared to other countries with larger CBM pipeline networks. CBM production in China is mainly derived from the high-rank coals in the Ordos and the Qinshui basins. Reported CBM production are considered to be indicative at best, with general press reports stating that CBM production was just over 1 BCF in 2006 and increased to 51 BCF in 2010. These reservoirs likely underestimate the actual production and may only reflect the rate of increase in large CBM production projects in China over the last five years. Despite the challenges in obtaining reliable data, CBM production in China is expected to increase significantly due to the country's vast coal resources and growing energy demands, potentially rivalling other major CBM producing countries in the world (for more details see (Ewen et al., 2012; Fuyuan Mu et al., 2015; Moore, 2012; Palmer, 2010)).

1.1.4.CBM in Lorraine

The coal deposits in the Lorraine region have remained unexploited since the closure of the Houve mine in 2004. However, it still contains abundant natural gas resources, including CBM.

Initial studies by IFP Énergies Nouvelles estimated in 2013, based on data from La Française de l'Énergie, that 370 billion m^3 of coal gas were buried in the Lorraine underground.

Exploring CBM recovery in Lorraine is part of the global trend of searching for unconventional natural gas. These resources are expected to act as a transitional solution towards a low-carbon economy where renewable sources of energy will dominate.

Trapped in flooded coal seams in Lorraine, over 95% of this gas is methane. Besides, tectonic activity has completely fragmented the Lorraine undeground over the geological history (Figure 4). The gas can therefore escape from the veins without the need for hydraulic fracturing techniques, but only by pumping out the water (Figure 5).

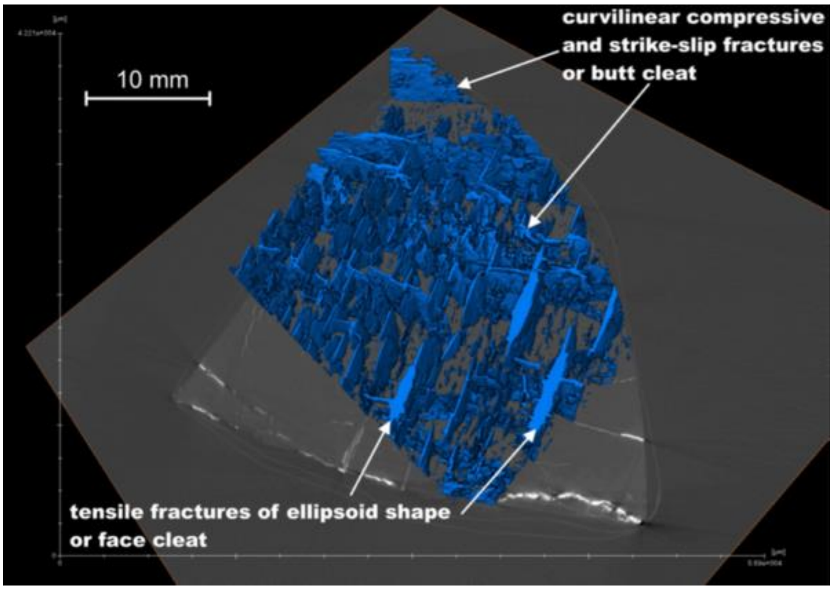

Figure 4 Natural fracture and cleat patterns in Lorraine basin coalbed reservoirs, preliminary study by Prof. Dr. Vitaliy Pryvalov (Regalor project).

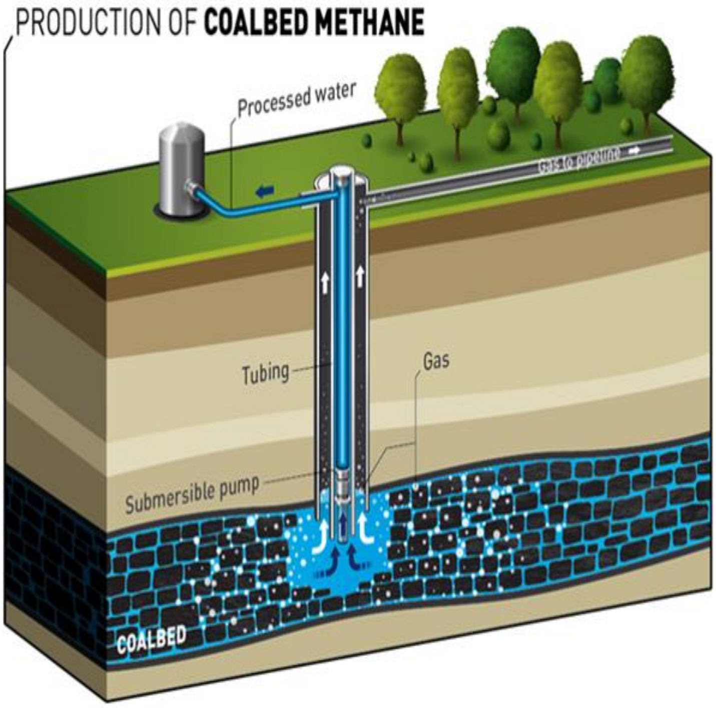

Figure 5 CBM recovery from pumping (http://www.total.com/fr/energies-savoir-faire)

In Lorraine, the Carboniferous basin is suspected to be a significant resource for CBM. As shown in Figure 6, the Lorraine Carboniferous Basin spans approximately 200 km in length and 80 km in width. Its sedimentary fill comprises around 8 km of fluvio-lacustrine deposits. The Westphalian strata (315-308 Ma), which predominantly contain coal deposits, are overlaid by fluvio-lacustrine series of the Stephanian (307-302 Ma), where coal is less abundant. Carboniferous-Permian strata lie beneath a Mesozoic cover ranging from 500 to 1800 m in thickness as shown in Figure 7 (Izart et al., 2016).

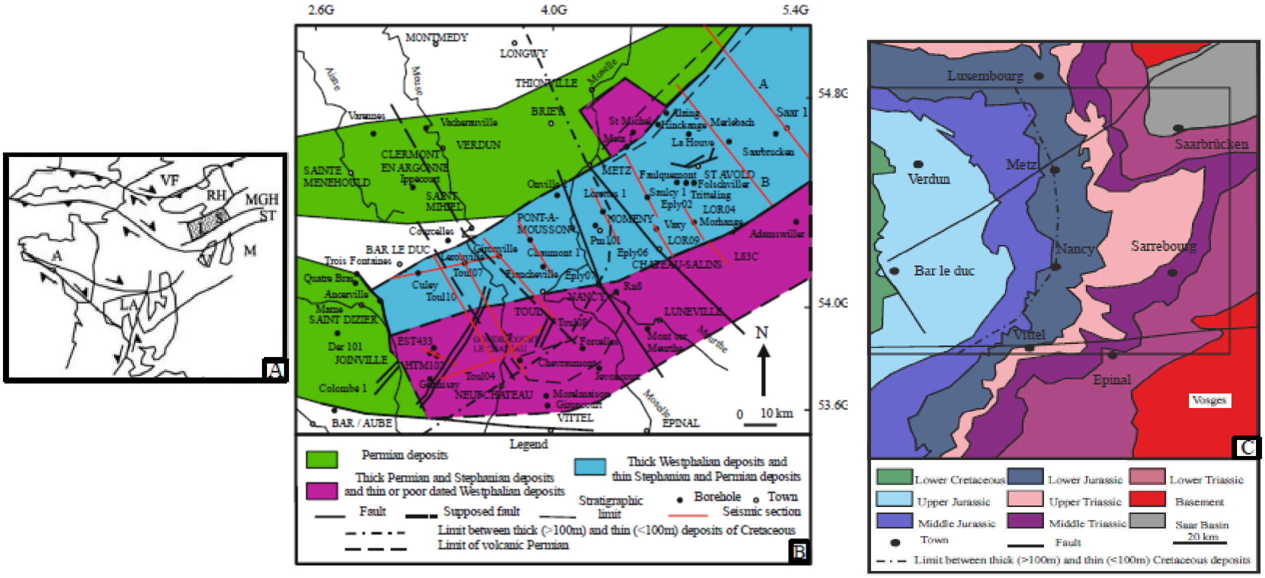

Figure 6 Location of the Lorraine Basin in the Variscan chain (A). Geological map of carboniferous and Permian basins (B) and geological map of Mesozoic cover (C). A: Armorican zone, L: Lorraine coal basin, LA: Liguro arvern zone, M : Moldanubian zone, MGH : mid German high, RH : Saxo Thuringian zone, V : vosges, VF : Hercynian foredeep. The rectangle in C corresponds to the contour of the map (Izart et al., 2016).

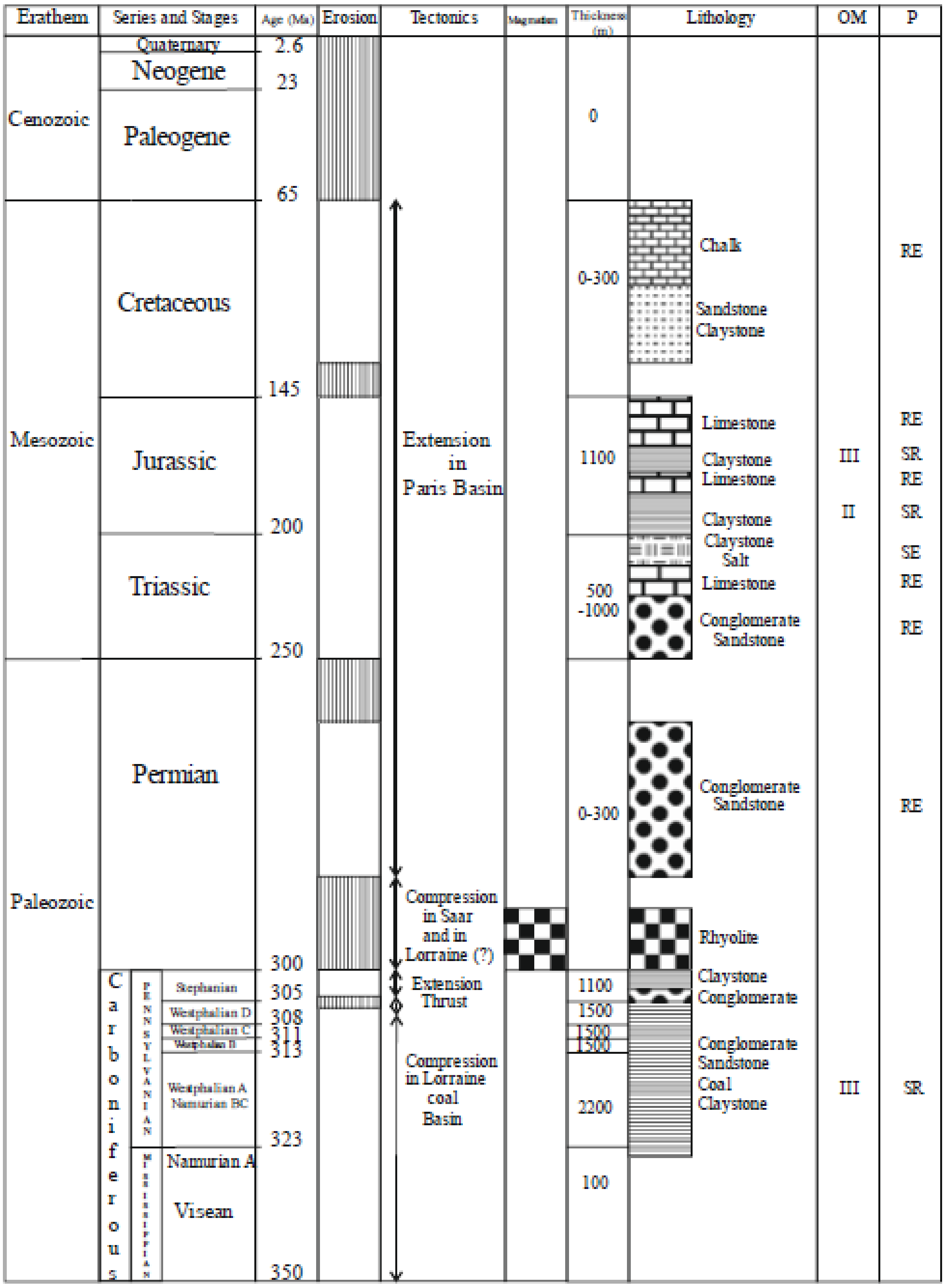

Figure 7 Chrono and lithostratigraphy from the Lorraine basin. Major erosional and tectonic events are shown.

OM : Organic matter type, P: petroleum type, RE: reservoir rock, SE: source rock (Izart et al., 2016)

1.1.5.Regalor project

The Regalor (Gas Resources in Lorraine) project was initiated in 2012 on the Grand-Est region‘s initiative and is supported with funding support from the European Regional Development Fund (ERDF). The project is held by GeoRessources laboratory (Université de Lorraine, CNRS) and is carried out in partnership with a Mosellan company, la Française de l’Énergie. It is a unique opportunity for scientists to collaborate with industrialists and provide guidance prior to the commencement of eventual extraction operation.

The objective of the project is to assess the viability of extracting coal gas in the Lorraine region with emphasis put on the associated environmental, territorial, and social impacts, to eventually make a well-informed decision at the end of the project. The outcomes of the project is expected to ensure a good territorial integration of the exploitation, from social perception to chances of re-industrialization. My thesis work is a part of this research project.

1.2.Research motivation and outline of the thesis

The swelling potential of coal is a crucial factor to consider when it comes to CBM recovery as it induces permeability evolutions that are peculiar to coal reservoirs (Figure 8).

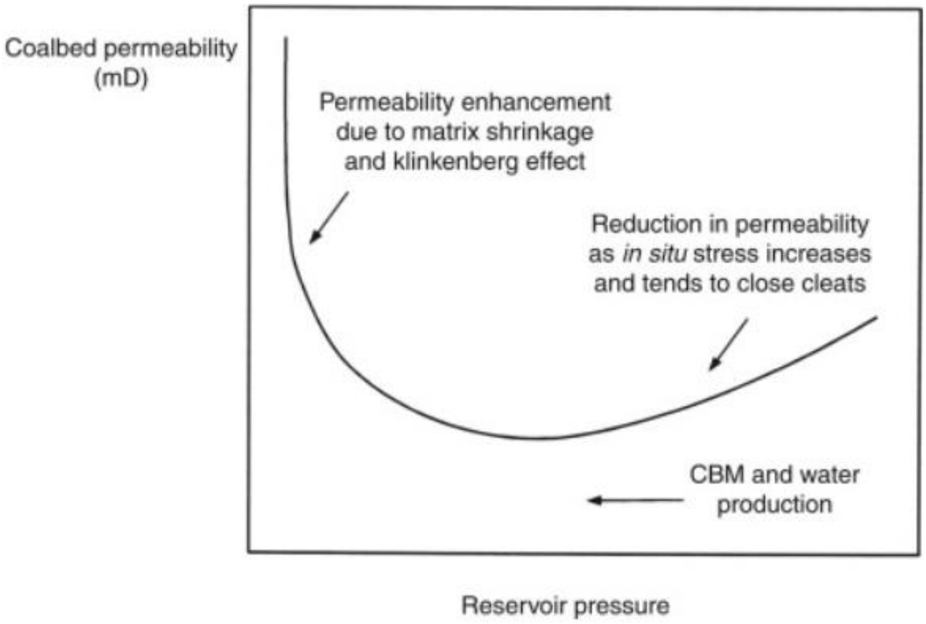

Figure 8 Permeability changes in coalbed with pressure decline due to changes in in situ stress, closure of cleats at the earlier stages, followed by the shrinkage of coal matrix and Klinkenberg effect at later stages.(Satter and Iqbal, 2016)

The ability to accurately predict the behavior of coal during gas injection and extraction processes is essential for the successful and efficient extraction of CBM. In order to perform a proper economic analysis of Enhanced Coalbed Methane (ECBM), it is necessary to have accurate projections of CO_2 injection and CH_4 extraction rates, which can only be achieved by using an appropriate model.

This model must take into account the variability in injectivity observed in the field and accurately describe the swelling that occurs as a result of adsorption. Unfortunately, many experimental studies conducted to better understand the behavior of coal during gas injection and extraction are incomplete and do not fully link and estimate all the parameters involved (as described in studies by Day et al., 2008b; Ottiger et al., 2008; Robertson and Christiansen, 2005). This is due to the challenging nature of the behavior of coal, which is a result of the interplay between several complex processes and mechanical responses.

Transport mechanisms that move gas molecules through the poral spaces of the coal system, as well as the behavior resulting from the adsorption isotherm and its induced swelling deformation, are some of the factors that make it difficult to fully understand the behavior of coal. The adsorption isotherm and the induced swelling deformation play a significant role in affecting the permeability of the system, and it is important to take these factors into account when creating an appropriate reservoir model. The challenge of fully understanding and predicting the behavior of coal reservoirs during gas injection and extraction highlights the importance of continued research and experimentation in this field.

To further our understanding of the behavior of coal, our initial objective is to describe coal as a material in **Chapter 2**, providing a comprehensive literature review about its behavior and the different physical processes involved in its hydro-mechanical responses when subjected to gas flow. Then, we will present the different numerical approaches that were proposed to model its hydro-mechanical behavior.

Chapter 3 focuses on our proposed approach for modeling the HM behavior of the coal matrix. We will present the modeling approach based on the coupling of a discrete element method (DEM) with a pore-scale finite volume method (PFV) where we implemented the transport mechanisms and sorption induced deformation processes. We'll present how we validated the model and how its predictions stack up with experimental observations. We'll also show that the model can be used to further expand our knowledge of coal response in terms of dynamics.

In **Chapter 4**, the focus will be on the cleat system in coal and the combination of the cleat and matrix scales. The aim of this chapter is to focus on the flux exchange taking place between cleat and matrix and on the evolution of permeability in the cleat taking into consideration the swelling potential of the coal matrix and the evolution of gas concentrations through the fractured medium. Darcy's law describes gas flow through the cleats and exchanges between cleats and matrix is governed by some of the transport mechanisms occurring within the matrix (described in Chapter 3). The outcome of this analysis will provide valuable insights into the behavior of coalbed methane reservoirs, especially for what concerns their permeability changes induced by sorption induced deformations.

The final chapter, **Chapter 5**, will be dedicated to demonstrate the conclusions and some future works that would be needed to further enhance the model capabilities.

Chapter 2

Literature Review

Chapter 2 : Literature Review

2.1.Formation and Occurrence of Coal

Coal is formed from the remains of plants and other organic materials that have undergone a process of transformation over millions of years. The formation of coal begins with the accumulation of plant debris in a swampy depositional environment, such as a river delta or a coastal plain (Scott, 1999). In these environments, the plant debris becomes buried under layers of sediment, and over time, it undergoes physical and chemical changes that transform it into coal (Diessel, 1992).

The first stage in the formation of coal is the accumulation of plant debris in a swampy environment to form a soft, spongy sediment called peat. Peat is composed of partially decomposed plant material that is rich in carbon and other organic compounds (Ward and Suárez-Ruiz, 2008). The accumulation of peat requires the presence of stagnant water and a lack of oxygen, which inhibits the decay of organic material by microbes.

Over time, the peat becomes buried under layers of sediment, and as the pressure and temperature increase with burial, the peat begins to undergo a process of transformation called coalification or rank advance. The first stage in coalification is the formation of lignite, a brownish-black coal with a relatively low energy content (Riazi and Gupta, 2015). As the pressure and temperature increase further, the lignite is transformed into sub-bituminous coal, bituminous coal, and finally anthracite, a hard, shiny coal with a high energy content (Winschel, 1990).

The process of coalification involves a complex series of physical and chemical changes that result in the concentration of carbon and other organic compounds in the coal as represented in Figure 9. The main factors that influence coalification are the type and amount of plant material, the temperature and pressure conditions during burial, and the length of time over which the coal has been forming (Scott, 1999). Other factors that can affect coal quality include the presence of minerals, such as sulfur and ash, which can affect combustion efficiency and produce harmful emissions when burned (Vamvuka et al., 2006).

In summary, coal is a type of sedimentary rock that is formed from the lithified remains of plants and other organic materials. The process of coalification involves physical and chemical changes that transform the original plant material into coal over millions of years. The quality and characteristics of coal depend on a variety of factors, including the type and amount of plant material, the burial conditions, and the length of time over which the coal has been forming.

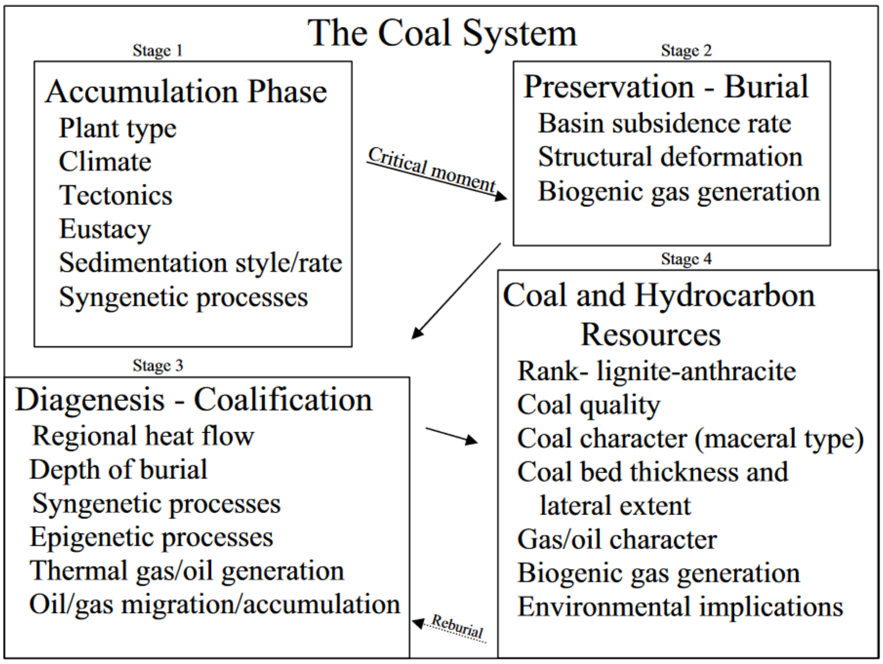

Figure 9 Outlines of coal formation. (Warwick, 2005)

2.1.1.Coal Fundamentals

To understand the recovery of CBM, it is crucial to have a thorough understanding of the fundamental properties of coal. Coal is a sedimentary rock formed as rock strata (what we call a “coal seam”) composed of three main components: the coal matrix, the cleats, and the mineral matter. The coal matrix is the organic component of coal, while the cleats are the void pores, and the mineral matter is the inorganic component (Yao et al., 2009). Each component has unique properties that impact gas recovery from coal.

2.1.1.1.Matrix

The coal matrix is made up of various macerals, including vitrinite, inertinite, and liptinite. Coal can be classified into banded and non-banded coals based on their macroscopic appearance. Banded coals contain alternating bands of bright and dull materials, while non-banded coals have a uniform appearance (Anggara et al., 2014). Most coals are banded and consist of multiple lithotypes originating from different plant materials (Flores, 2013; Warwick, 2005). The composition and properties of the coal matrix significantly impact coal quality and the efficiency of energy extraction processes (Dindarloo et al., 2015; Thomas, 2002).

Several systems are used to describe the macroscopic attributes of coal, including the terminology proposed by (Stopes, 1919) (Table 1). This system consists of four macro-lithotypes: vitrain, clarain, durain, and fusain. Vitrain is a bright, glassy material with a shiny lustre, characterized by fine cracks at right angles, creating a blocky appearance. In contrast, durain is a grey to black material with a dull lustre, and its fractures have rougher surfaces than those of vitrain. Clarain is bright with a silky lustre between vitrain and durain, composed of alternating thin layers (<1 mm). Fusain is a black material with a silky lustre, which is soft and friable, usually occurring as lenses that are several milli-meters thick.

(Schopf, 1960) proposed a new terminology adopted by the US Geological Survey (USGS) in which attrital coal was introduced to represent all types that are not defined as vitrain or fusain. Attrital coal is subdivided into five levels: bright, moderately bright, midlustrous, moderately dull, and dull (Table 2). Similarly, the Australian coal industry uses bright and dull coal instead of vitrain and fusain, respectively. Coals are graded according to the constituents of bright and dull materials, as shown in Table 2 (Dindarloo et al., 2015; Dutcher, 1978; Flores, 2013; Thomas, 2002).

Table 1

Coal macro-lithotypes described by (Stopes, 1919).

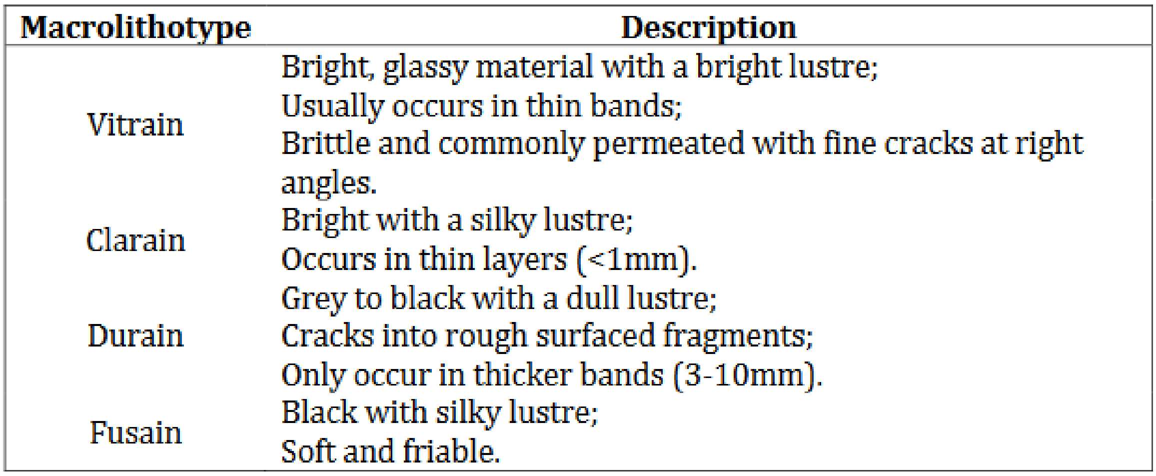

Macrolithotype	Description
Vitrain	Bright, glassy material with a bright lustre; Usually occurs in thin bands; Brittle and commonly permeated with fine cracks at right angles.
Clarain	Bright with a silky lustre; Occurs in thin layers (<1mm).
Durain	Grey to black with a dull lustre; Cracks into rough surfaced fragments; Only occur in thicker bands (3-10mm).
Fusain	Black with silky lustre; Soft and friable.

Table 2

Coal macro-lithotypes classifications (Dutcher, 1978; Schopf, 1960)

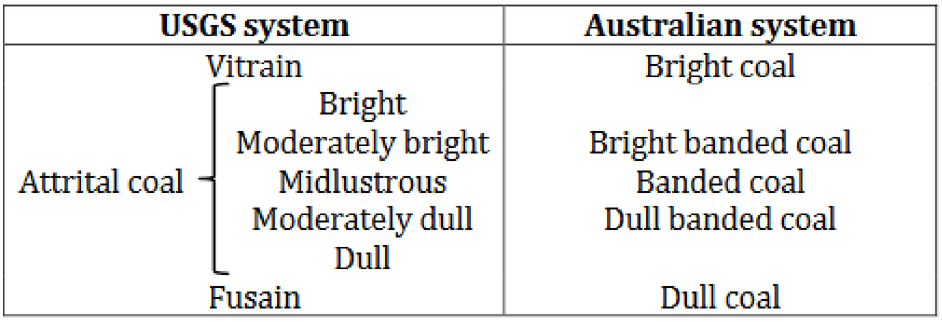

USGS system		Australian system
Vitrain		Bright coal
Attrital coal	Bright	
	Moderately bright	Bright banded coal
	Midlustrous	Banded coal
	Moderately dull	Dull banded coal
	Dull	
Fusain		Dull coal

2.1.1.2.Cleats

Coal is a naturally fractured rock, which means that it contains a complex network of fractures, also known as "cleats”. Cleats are the main pathways for fluids, and they control the permeability of coal and the production of coal seam gas (CSG) (Balucan et al., 2018; Gamson et al., 1993; Pattison et al., 1996). The cleats are categorized into two major classes: bright cleats and dull cleats, depending on the lithotype they are embedded into (Esterle et al., 2002, 1994).

Bright cleats occur in two sets of sub-parallel cleats: face cleats and butt cleats. Face cleats constitute the dominant fracture set, comprising well-developed and persistent parallel fractures (Figure 10). They form first during coalification and are more conspicuous in hand specimens because they extend longer (Gamson and Beamish, 1992; Kendall and Briggs, 1934). Butt cleats occur later due to the relaxation of the original stress field and are characterized as shorter and roughly parallel fractures. They commonly terminate at face cleats, presenting a "T-junction" connectivity pattern in an organized bright cleat system (Dawson and Esterle, 2010; Mostaghimi et al., 2017). Both sets of cleats are perpendicular to the bedding planes. Bright cleats only penetrate within a single bright band and are bounded by dull bands. Thus, cleat heights tend to vary with the thickness of their host bright band. The band thickness is proportional to the average cleat spacing, where thicker bands have larger cleat spacing.

Dull cleats, on the other hand, are poorly developed and appear to be short, discontinuous, and unidirectional. They only exist within dull bands without cutting any bright layers. Dull bands do not have a systematic cleat network, and face cleats are hardly recognized and poorly developed (Jing et al., 2017a; Ting, 1977).

2.1.1.3.Minerals (inorganic components)

Minerals found in coal can be categorized into two main groups based on when they formed. Syngeneic minerals are those that developed during the initial accumulation of peat, while epigenetic minerals formed after the coal had matured (Singh and Naik, 2015). The formation of these minerals is closely tied to the processes of peat accumulation and changes in subsurface fluids (Ward, 2002). Epigenetic minerals, which often include kaolinite, illite, pyrite, and calcite, are typically found in the cleats within coal formations. These minerals can be present either within the coal matrix itself or within the cleats, as indicated by various studies (Dai et al., 2006; Daniels et al., 1996; Dawson et al., 2012; Misra and Reddy, 2004).

Minerals can be found in either the coal matrix or the cleats, as indicated by (Dawson et al., 2012). When minerals are distributed within the cleats, they often exhibit well-developed morphological characteristics, as observed by (Deng et al., 2015; Zhang et al., 2016). (Zhang et al., 2016) noted that the morphology of mineral fillings within cleats closely resembles the network of coal cleats. This includes the presence of 'T-junction' connections, which resemble the connectivity pattern of face and butt cleats. Additionally, mineral fillings within cleats are typically oriented perpendicular to the bedding plane.

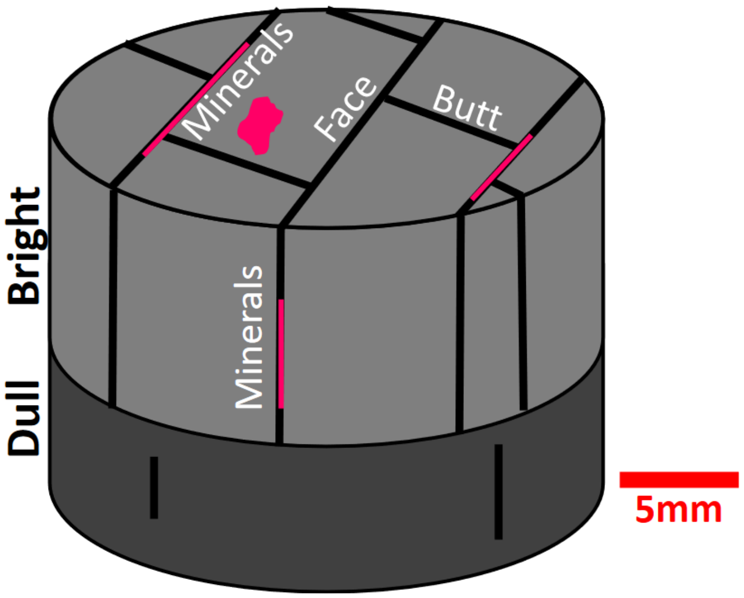

Figure 10 Coal structures: the bright band exhibits a distinct cleat network characterized by the orthogonal connection of face and butt cleats, forming a 'T-junction' pattern. Minerals can be found in either the cleats or the coal matrix. Minerals within the cleats share a morphology similar to that of the cleats themselves (Jing, 2017).

2.1.2.Coal characteristics

Coal properties can be studied and understood in terms of three independent geological parameters: rank, type, and grade (Scott, 1999).

The rank of coal is determined by the degree of coalification or metamorphism that the original plant debris has undergone during its burial history. This depends on the maximum temperature and time it has been exposed to, the depth of burial, and the geothermal gradient in the basin. Heat flow from nearby igneous intrusions can also play a part. The classification of coal into different ranks based on properties such as carbon content, volatile matter content, calorific value, and moisture content (Figure 11) is important for understanding its potential uses. As coal progresses through the maturation process, its properties change in a predictable way, with higher-rank coals having a higher carbon content, lower oxygen and hydrogen content, lower volatile matter content, and higher calorific value.

The type of coal reflects the nature of the plant debris from which the original peat was derived, including the mixture of plant components involved and the degree of degradation to which they were exposed before burial. The individual plant components occurring in coal, and in some cases fragments or other materials derived from them, are referred to as macerals. Different types of coal can have different proportions of macerals, which can affect their properties and uses (O’Keefe et al., 2013).

The grade of coal reflects the extent to which the accumulation of plant debris has been kept free of contamination by inorganic material, including mineral matter. High-grade coal is a coal with a low overall proportion of mineral matter and a high organic matter content, regardless of its rank or type. High-grade coal is typically more desirable for energy production and other applications (Ward and Suárez-Ruiz, 2008).

Other factors that can affect coal properties include the burial conditions and the length of time over which the coal has been forming. These factors can affect the porosity, density, and other physical and chemical properties of coal (Vamvuka et al., 2006).

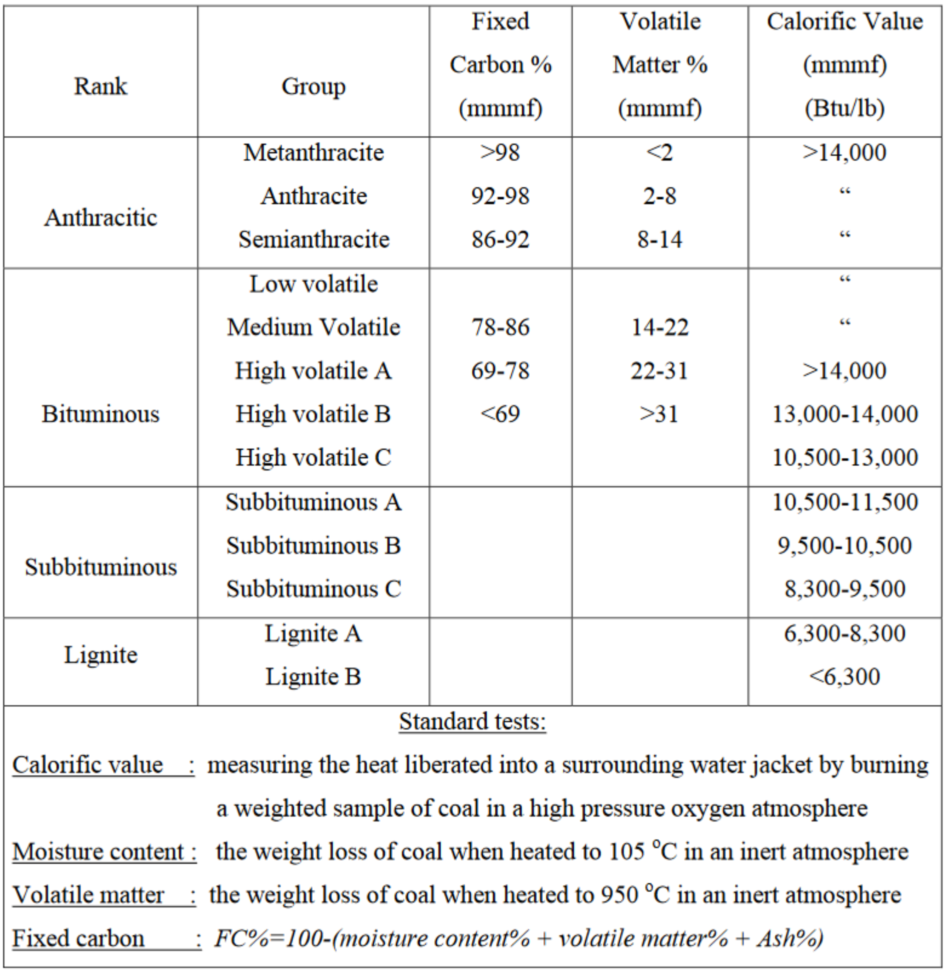

Rank	Group	Fixed Carbon % (mmmf)	Volatile Matter % (mmmf)	Calorific Value (mmmf) (Btu/lb)
Anthracitic	Metanthracite	>98	<2	>14,000
	Anthracite	92-98	2-8	“
	Semianthracite	86-92	8-14	“
Bituminous	Low volatile			“
	Medium Volatile	78-86	14-22	“
	High volatile A	69-78	22-31	>14,000
	High volatile B	<69	>31	13,000-14,000
	High volatile C			10,500-13,000
Subbituminous	Subbituminous A			10,500-11,500
	Subbituminous B			9,500-10,500
	Subbituminous C			8,300-9,500
Lignite	Lignite A			6,300-8,300
	Lignite B			<6,300

Standard tests:

Calorific value : measuring the heat liberated into a surrounding water jacket by burning a weighted sample of coal in a high pressure oxygen atmosphere

Moisture content : the weight loss of coal when heated to 105 $^{\circ}$C in an inert atmosphere

Volatile matter : the weight loss of coal when heated to 950 $^{\circ}$C in an inert atmosphere

Fixed carbon : *FC%=100-(moisture content% + volatile matter% + Ash%)*

Figure 11 ASTM Classification of coal rank (Schobert, 2013).

2.1.2.1.Pores

Coal beds are dual porosity systems having micro pores that provide the main site of gas storage and macropores formed by the cleats that provide the essential path for fluid flow. Macropores are defined as being > 50 nm in diameter, mesopores > 2 and 50 nm, and micro pores < 2 nm (Gan et al., 1972).

The rank of coal influences the volume of its pores and their frequency (Bustin and Clarkson, 1998; Gan et al., 1972). Levine, (1996) found that macropores decrease and micropores increase with rank as illustrated in Figure 12.

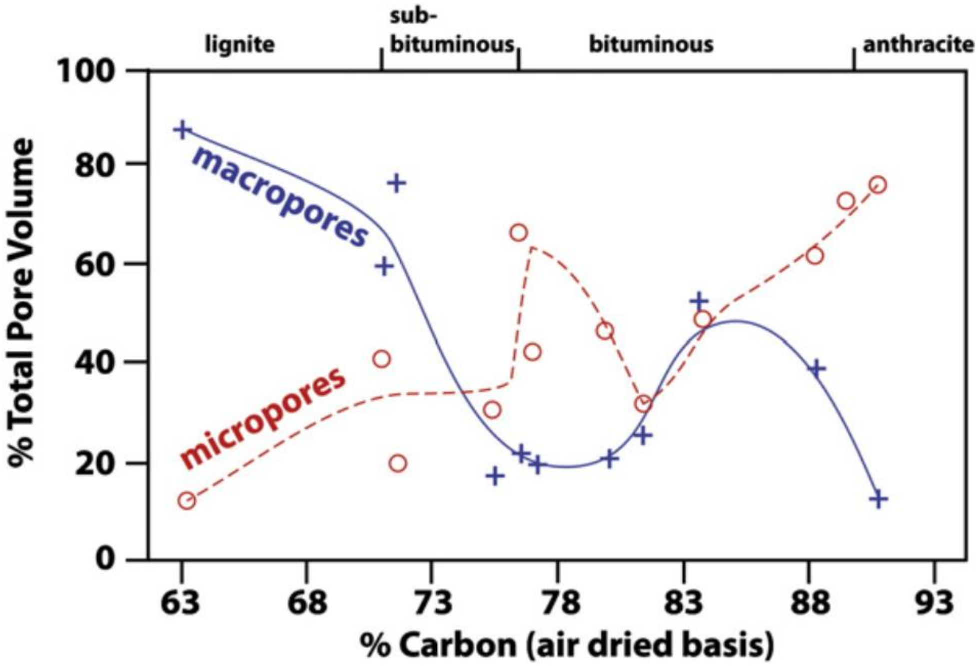

Figure 12 Contribution to the total pore volume of macropores and micropores as a function of the coal rank. Modified from Levine (1996).

The measurement of pore volume in coal is a challenging task, and the results are often plagued by inaccuracies. Historically, mercury intrusion porosimetry (MIP) was the standard method for measuring pore volumes in various materials, including coal. However, MIP has limitations and lacks repeatability when applied to coal samples, which has led to its decreasing use in recent years.

Instead of MIP, researchers have turned to alternative techniques for estimating pore volume in coal, such as small-angle X-ray scattering (SAXS) and small-angle neutron scattering (SANS). These methods offer more quantitative and reliable assessments of pore volume in coal. SAXS and SANS are powerful tools for characterizing the nanoscale and microscale structures of materials, making them suitable for studying the pores in coal.

The porosity values used for modeling gas flow in coal samples typically range from 1% to 5%, as reported in studies like (Close et al., 1993; Zarrouk and Moore, 2009). However, it is worth noting that some research using SAXS and SANS techniques has indicated higher porosity values, ranging from 16% to 25%, as reported in (Mares et al., 2009).

The variation in reported porosity values underscores the complexity of understanding the nature of pores in coal. Coal is a heterogeneous material with a wide range of pore sizes and shapes, and the choice of measurement technique can greatly impact the results.

2.1.2.2.Permeability

The permeability of many CBM reservoirs exhibits anisotropy, meaning that the permeability is greater in one direction than in another. This anisotropy is believed to result from the influence of differential in situ stress on cleats, as discussed by (Gash et al., 1992; Paul and Chatterjee, 2011). Understanding this directionality of permeability is crucial for optimizing well placement in CBM reservoirs.

The primary reason behind the anisotropy of permeability is often attributed to the greater continuity of the face cleats, which run in one direction, compared to that of the butt cleats, which run in a nearly perpendicular direction. However, it's worth noting that the specific nature of connectivity between the butt and face cleats may also play a significant role in controlling permeability anisotropy, as highlighted by (Law and Rice, 1993).

To illustrate this phenomenon, a study conducted by (Gash et al., 1992) using coal from the La Plata mine in the San Juan Basin, under a pressure of 6.895 MPa, revealed interesting findings. Parallel to the bedding plane, the permeability was observed to be in the range of 0.6 to 1.7 millidarcies (mD) in the direction of the face cleats, and of 0.3 to 1.0 mD in the direction of the butt cleats. However, the permeability in the direction normal to the bedding plane was significantly lower, measuring just 0.007 mD.

These results underscore the significance of understanding permeability anisotropy in CBM reservoirs, as it directly impacts decisions related to well placement and reservoir development strategies. The interplay between cleat orientation and connectivity is a complex factor that influences the directional permeability of these reservoirs.

2.1.3.Coalbed Methane Recovery

Methane gas is mainly stored in the coal matrix as an adsorbed layer (Gray, 1987; White et al., 2005), with around 95-98% of the trapped methane ultimately remaining in the coal matrix. The rest of methane is either dissolved into the pore water or present as free gas phase in fractures and the largest pores. This trapped methane can be recovered as natural gas, referred to as CBM, through a process called CBM production.

CBM production involves recovering methane from coal beds upon desorption. This is achieved by reducing gas and water pressure in the cleat network, which allows the production of methane. However, coal beds have low permeability compared to conventional natural gas reservoirs like sandstone formations, which makes the extraction of methane challenging. To increase the amount of methane that can be extracted, enhanced coalbed methane (ECBM) production methods are used (Bahadori, 2018; Mazzotti et al., 2009), in which other gases such as N2, CO2, and flue gas are injected into the coal bed. These gases help to increase the methane desorption, making it easier to extract methane.

Of these gases, CO2-ECBM is of particular interest because coal preferentially adsorbs CO2 over CH4 (Liu et al., 2015; Merkel et al., 2015; Ottiger et al., 2008). This means that by injecting CO2 into the coal bed, methane can be displaced, allowing it to be extracted. Hence, coal is a potential lithology for combining ECBM and geological storage of CO2, which means that CO2 can be stored underground in coal seams, reducing its release into the atmosphere and helping to mitigate climate change. During CO2-ECBM production, a challenge arises where the partial replacement of CH4 by CO2 causes a net swelling due to a new equilibration with the gas/fluid mixture in the coal seam. This leads to swelling or shrinkage effects related to sorption and desorption of both CO2 and CH4 that greatly affect the permeability of coal seams (Harpalani and Chen, 1997, 1997; Levine, 1996; Puri and Seidle, 1992; Robertson and Christiansen, 2005). The impact of mixed gas sorption, such as CO2-CH4 and CO2-N2 mixtures, on the swelling of coal matrix material is not yet fully understood.

Sorption experiments (such as those conducted by Busch and Gensterblum, (2011)) have demonstrated that the quantity of nanoscale and polyaromatic porosity in this size range increases proportionally with the amount of crystalline carbon content.

2.2.Gas flow and transport in coal

The flow process in coal is a complex physical phenomenon that encompasses two primary transport mechanisms as illustrated in Figure 13: advection and diffusion (Bird et al., 2002). The total gas flux can be decomposed as:

$$J_g = J_{g,Dif} + J_{g,Adv} \tag{2.1}$$

where $J_{g,Dif}$ and $J_{g,Adv}$ are the advective and diffusive components of the flux, respectively.

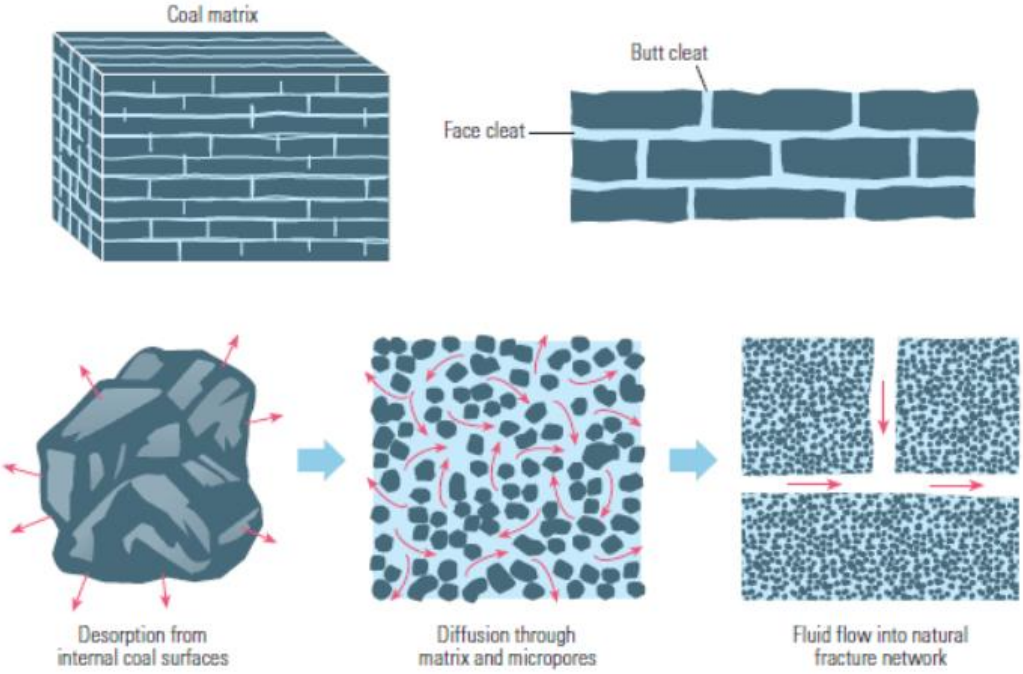

Figure 13 Different scales of flow in coal (Al-Jubori et al., 2009)

2.2.1.Gas transport through the matrix

The process of gas desorption from the coal matrix to the cleat is a complex phenomenon that involves gas being desorbed from the solid phase toward the pores and diffusing through the pores to reach cleats. This process is crucial for the extraction of gas from coal beds, as it determines the rate and amount of gas that can be produced.

Within porous media, there are three distinct diffusion mechanisms that govern the movement of gas molecules: molecular diffusion, Knudsen diffusion, and surface diffusion as represented in Figure 14. The dominant mechanism depends on factors such as pore size, system pressure, and the strength of adsorption.

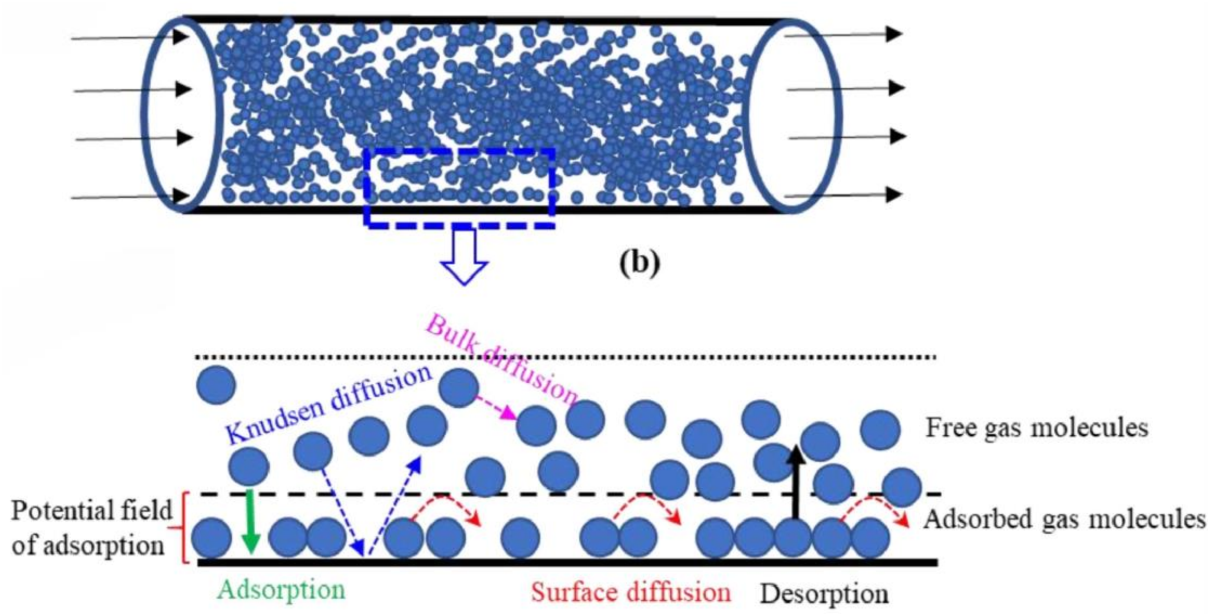

Figure 14 Transport mechanisms occurring in the pores of the coal matrix (Liu et al., 2020)

Molecular diffusion occurs when gas molecules move due to inter-molecular collisions, and this mechanism is significant in large pore and/or high system pressures. In contrast, Knudsen diffusion is important when the mean free path of the gas molecules is greater than the pore size, and gas molecules collide with the pore walls to move through the system.

Surface diffusion is the third mechanism, and it occurs when adsorbed molecular species move along the pore wall surface. This mechanism is significant for micropores with strongly adsorbed species, such as in coal beds.

A generalised Fick's law of diffusion (Fick, 1855) used to describe the diffusion of the gas species can be expressed as:

$$J_{g,Dif} = -D_g \nabla c_g \tag{2.2}$$

where c_g is the concentration of gas and D_g is the diffusion coefficient that depends on the type of diffusion that is taken into consideration.

2.2.2.Gas transport through the cleats

Intrinsic permeability refers to a medium's capacity to transport a single fluid phase. However, coal beds involve two fluid phases, gas and water. In multiphase fluid systems, we use two key terms: intrinsic permeability, denoting the medium's ability to transmit a specific fluid, and relative permeability, which is the ratio of effective permeability at a given saturation to intrinsic permeability for that particular fluid.

2.2.2.1.Single phase flow models

The advective movement of bulk gases within porous materials is powered by the pressure difference and is typically described by Darcy's law (Darcy, 1865). The overall advective flow can be formulated as:

$$J_{g,Adv} = cU \tag{2.3}$$

with $$U = \frac{k}{\mu}(\nabla P - \rho g) \tag{2.4}$$

where U is the bulk gas velocity, c is the concentration of gas, μ the dynamic viscosity, and P the fluid pressure.

2.2.2.2.Two phase flow models

The classical two-phase flow model is an empirical extension of Darcy's model, which was originally developed for single-phase flows. It is based on the assumption of local capillary equilibrium, which means that, within the study of a representative elementary volume, the distribution of phases is governed exclusively by capillarity, without any influence from viscous effects.

The succession of capillary equilibria is described by the pressure differential between the liquid and gas phases $P_c(S) = P_g - P_l$, where P_c is the capillary pressure, which depends solely on saturation (a direct consequence of the initial assumption), P_g is the gas pressure, and P_l is the liquid pressure. Hysteresis effects are often disregarded. The underlying idea behind this strong assumption is that each fluid follows its own path through a portion of the pore space reserved for it, without being influenced by the other fluid. Consequently, permeability depends solely on saturation. In this manner, the filtration velocities of each phase can be defined as in Darcy's law:

$$U_l = \frac{k_l(S_l)}{\mu_l}(\nabla P_l - \rho_l g) \tag{2.5}$$

$$U_g = \frac{k_g(S_g)}{\mu_g}(\nabla P_g - \rho_g g) \tag{2.6}$$

where U_l and U_g are the fluid velocities, μ_l and μ_g are the dynamic viscosities, ρ_l and ρ_g are the mass densities, and k_l and k_g are the effective permeabilities of each phase. Classical curves of relative permeabilities as a function of saturation are presented in Figure 15. We transition from relative permeability to effective permeability K by multiplying the intrinsic permeability k of the porous medium for each phase:

$$K_l(S) = kk_{rl}(S) \tag{2.7}$$

$$K_g(S) = kk_{rg}(S) \tag{2.8}$$

where k_{rl} and k_{rg} are the effective permeabilities of each phase

In addition to this, we add the system of continuity equations for a closed system:

$$n\frac{\partial \rho_g S_g}{\partial t} + \nabla \rho_g U_g = 0 \tag{2.9}$$

$$n\frac{\partial \rho_l S_l}{\partial t} + \nabla \rho_l U_l = 0 \tag{2.10}$$

with n representing porosity, both phases completely occupying the pore space, S_g+ S_l = 1.

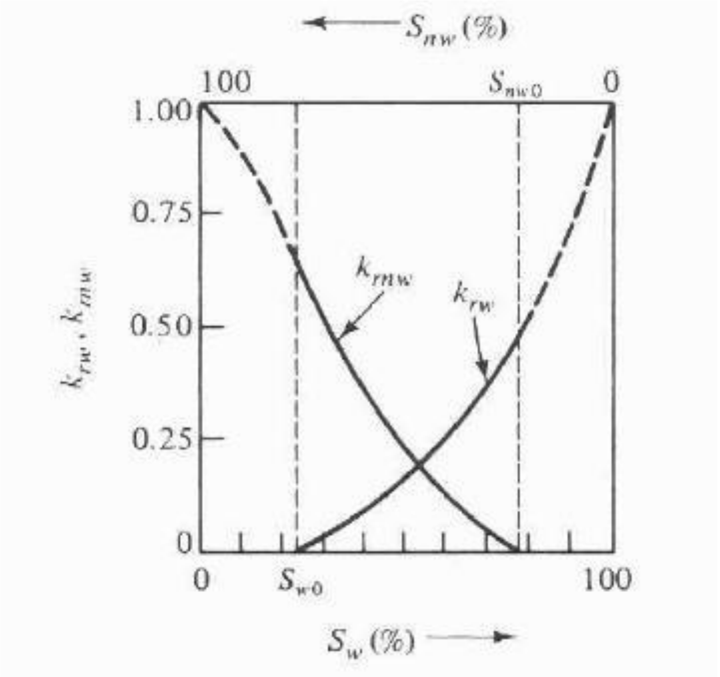

Figure 15 Evolution of relative permeabilities with saturation (the index 'w' corresponds to the wetting fluid, and the index 'nw' to the non-wetting fluid) (Lefort P., 2014)

2.3.Adsorption in coal

Adsorption is a complex process that occurs when a gas or vapor comes into contact with a solid adsorbent, leading to the gas molecules adhering to the surface of the solid. Adsorption should not be mistaken with "absorption" which refers to the penetration of gas molecules into the mass of a solid. Also, the term "sorption" is often used to emphasize the adsorption on a surface, absorption by penetration into the lattice of the solid, and/or capillary condensation within the pores (Gregg and Sing, 1982).

Physical adsorption (physisorption) and chemical adsorption (chemisorption) are the two main types of adsorptions. In chemisorption, the adsorbate forms a chemical bond with the solid surface. In contrast, physisorption occurs due to Van der Waals and electrostatic forces between the adsorbate and adsorbent surface. Because physical adsorption does not involve a chemical bond, it is a reversible process. At low pressures, physical adsorption usually occurs as a monolayer on the surface, while at higher pressures, multilayers can form, depending on the adsorbent and the adsorbate used.

Adsorption of gas can be described based on different isotherms. I present below the most commonly used for describing adsorption in coal:

- Langmuir isotherm

The Langmuir isotherm (Langmuir 1918) assumes homogeneous surfaces where adsorption is local, specific, and occurs on a limited number of sites where a monolayer of adsorption is formed. It can be expressed as:

$$K_{att}\ P\ S(1-\theta) = K_{det}\ \ P\ \theta \tag{2.11}$$

where S is the number of adsorption sites, θ is the surface fraction coverage, and K_{att} and K_{det} represent the adsorption and desorption constants, respectively.

Equation (2.11) can be rewritten as:

$$\theta = \frac{q}{q_m} = \frac{\alpha P}{1+\alpha P} \tag{2.12}$$

with q the amount of gas adsorbed, q_m the maximum amount of gas adsorbed, and $\alpha = \frac{K_{att}}{K_{det}}$

- Toth isotherm

The Toth isotherm is a modification of the Langmuir isotherm. The Toth isotherm takes into account the heterogeneity of the adsorbent surface and the non-uniform energy distribution of the adsorption sites (Toth 1962).

The Toth isotherm can be expressed as:

$$\frac{q}{q_m} = \frac{\propto_t P}{\left[1+(\propto_t P)^{\delta}\right]^{1/\delta}} \tag{2.13}$$

where q is the amount of gas adsorbed, q_m is the maximum amount of gas adsorbed, $\alpha = \frac{K_{att}}{K_{det}}$, and δ is Toth isotherm constant (0< δ <1).

- Temkin isotherm

The Temkin isotherm assumes that the heat of adsorption of all molecules in the layer decreases linearly with coverage due to adsorbent-adsorbate interactions (Asnin et al., 2001). The Temkin isotherm can be expressed as:

$$\frac{q}{q_m} = \frac{RT}{Q} \ln(KP) \tag{2.14}$$

where R is the ideal gas constant, T is the temperature, Q is related to heat of adsorption, and K is the equilibrium building constant.

Huddleston et al., (1995) conducted a study focusing on methane adsorption at a temperature of 51 °C and a pressure of 15 MPa. Their findings revealed a notable influence of particle size on gas sorption capacity. Specifically, an increase in particle size resulted in a corresponding increase in sorption sites, leading to enhanced sorption capacity. In their analysis, they found that the Langmuir sorption isotherm provided the best fit for the results under low-pressure conditions. However, for the entire range of the isotherm, a third-order polynomial function was found to be a suitable model.

Hall et al., (1994) conducted experiments to measure the adsorption behavior of methane, nitrogen, and carbon dioxide. Their analysis led them to conclude that the Langmuir model was found to be less accurate in describing the adsorption behavior.

Harpalani and Pariti, (1993) conducted a study focusing on the adsorption behavior of a multicomponent gas mixture consisting of methane and carbon dioxide. Their findings revealed that during the desorption process of methane, the concentration of methane decreased while that of carbon dioxide increased. They determined that the extended Langmuir isotherm provided the best fit for their experimental results.

Stevenson et al., (1991) conducted experiments to measure the adsorption isotherms of methane, carbon dioxide, and nitrogen on coal at a temperature of 30 ℃ and a pressure of 5 MPa. Their findings demonstrated that the quantity of gas adsorbed was influenced by both the gas type's composition and the system's pressure.

One notable study conducted by (Yang and Saunders, 1985) involved the examination of methane adsorption isotherms on coals over a wide temperature range (22 to 300 ℃) and at pressures ranging from 0 to 7 MPa. Their findings were well-fitted to the Langmuir isotherm. In the case of Canadian coals, Patching and Mikhail, (1986) developed an isotherm that accounted for factors such as temperature, moisture content, gas type, and coal type. They concluded that both Langmuir and Freundlich isotherms were suitable for describing their data. Similarly, Mavor et al., (1990) studied American coals and found that the Langmuir adsorption model provided the best fit for their data.

However, it is important to note that there are instances where the early stages of Langmuir adsorption do not apply. In the case of British coal, as highlighted by Moffat and Weale, (1955), Langmuir isotherms did not adequately represent their results due to various limitations.

In summary, while the Langmuir isotherm is widely considered the most effective model for describing gas adsorption behavior in most coal types for methane gas, there are occasional exceptions and limitations. Nonetheless, it remains the preferred choice for many researchers in this field.

2.4.Hydro-mechanical couplings in coal

2.4.1.Poroelasticity theory

The poroelasticity theory first presented by (Biot, 1941), and later reformulated by (Coussy, 2004; Detournay and Cheng, 1993), provides a framework for understanding small deformations in fluid-saturated porous solids. It serves as an extension of elasticity theory tailored to the specific conditions of interest, which involve porous rocks undergoing small, reversible strains. Two additional parameters become necessary to fully describe the state of the fluid: its pressure and its volume (or mass).

It is important to note, however, that the classic poroelasticity theory describes deformations in non-swelling materials. The original governing equations do not hold true for swelling materials. In the following sections, we will outline the primary equations used to characterize stresses and strains in both non-swelling and swelling materials.

2.4.1.1.Hydro-mechanical response of non-swelling porous media

According to the poroelasticity theory, the contribution of the pore pressure p to the overall deformation of non-swelling homogeneous isotropic elastic porous media is defined through the effective stress such as

$$\sigma' = \sigma - bp \tag{2.15}$$

where σ' is the effective stress, σ is the total stress, and b is the Biot coefficient equal to $1 - \frac{K}{K_s}$ with K the bulk modulus of the medium, and K_s the bulk modulus of the solid phase.

The deformation can be expressed as:

$$\varepsilon_{ij} = \frac{1}{2G}\sigma_{ij} - \left(\frac{1}{6G} - \frac{1}{9K}\right)\sigma_{kk}\delta_{ij} + \frac{b}{3K}p\delta_{ij} \tag{2.16}$$

where G is the shear modulus, $\sigma_{kk} = \sigma_{11} + \sigma_{22} + \sigma_{33}$, and δ_{ij} is the Kronecker symbol.

A derivation of equation (2.16) leads to the total matrix volumetric strain of non-swelling materials defined as:

$$\varepsilon_v = -\frac{1}{K}(\sigma - bp) \tag{2.17}$$

where ε_v is the total volumetric strain and σ is the mean compressive stress.

2.4.1.2.Hydro-mechanical response of swelling porous media

The effective stress for swelling materials has an additional term to account for the sorption induced deformation of the coal matrix (Gor and Neimark, 2010; Kowalczyk et al., 2008; Ustinov and Do, 2006; Yang et al., 2010):

$$\sigma' = \sigma - bp \tag{2.18}$$

with

$$p = p_f + p_s \tag{2.19}$$

where p_f is the bulk fluid pressure and p_s is the solvation pressure.

As a consequence, Equation (2.17) needs to be modified as follows:

$$\varepsilon_{ij} = \frac{1}{2G}\sigma_{ij} - \left(\frac{1}{6G} - \frac{1}{9K}\right)\sigma_{kk}\delta_{ij} + \frac{b}{3K}p\delta_{ij} + \frac{\varepsilon_s}{3}\delta_{ij} \tag{2.20}$$

where ε_s is the sorption induced swelling strain.

As a result, the volumetric strain becomes equal to:

$$\varepsilon_v = -\frac{1}{K}(\sigma - bp) + \varepsilon_s \tag{2.21}$$

An important note here is that ε_s depends on the isotherm describing adsorption within the medium. For instance, the Langmuir isotherm would lead to

$$\varepsilon_s = \varepsilon_L \frac{p}{P_L + p} \tag{2.22}$$

where ε_L and P_L are the Langmuir volumetric strain constant and the Langmuir pressure constant respectively.

2.4.2.Coal hydro-mechanical behavior

2.4.2.1.Swelling/shrinkage

Coal matrix swells or shrinks according to adsorption/desorption of gas. A lot of investigation has been made on swelling/shrinkage strains of coal considering different types of gas such as CH4, CO2, and N2.

Moffat and Weale, (1955) conducted a study examining the adsorption and desorption processes in coal. Their findings indicate that the maximum volumetric swelling occurred during CH4 adsorption, reaching 1.74%. Conversely, during CH4 adsorption, the maximum volumetric shrinkage was 1.49%. This variation in swelling occurred across a pressure range of 0 to 70 MPa for adsorption and 70 to 0 MPa for desorption. Their results revealed a discrepancy between shrinkage and swelling deformation behaviors.

Reucroft and Patel, (1986) conducted swelling experiments at a pressure of 0.1379 MPa and a temperature of 298 K, to investigate the adsorption of N2, He and CO2 on various ranks of coal. The study's findings indicated that the swelling strains varied between 0.36% and 1.07% as a result of CO2 adsorption, with coals possessing lower carbon content exhibiting a more pronounced swelling effect. Conversely, for N2 and He, minimal changes in volume were observed.

Harpalani and Schraufnagel, (1990b, 1990a) conducted CH4 desorption tests over a range of pressure cycles, varying from 0 MPa up to 6.83 MPa and then reversing the process. Their experiments revealed an initial swelling of 0.5%. Subsequently, upon desorption of gas from the same sample, a shrinkage deformation of 0.1% was observed. In contrast, with He, the coal matrix experienced a shrinkage as gas pressure increased by 0.0087%. As gas pressure decreased, the matrix then exhibited a swelling of 0.0002%, as depicted in Figure 16.

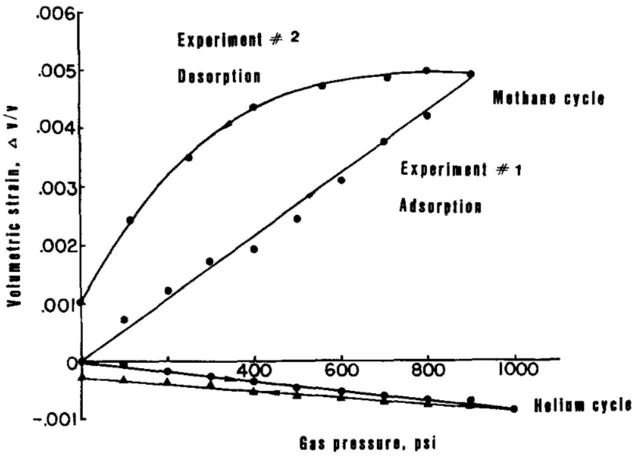

Figure 16 volumetric deformation vs pore pressure for helium and methane (Harpalani and Schraufnagel, 1990).

Levine, (1996) used high volatile bitumenious coal and observed 0.52 % swelling and shrinkage due to CH4 adsorption and desorption at 5.17 MPa, and about 1% due to CO2 adsorption and desorption at 3.1 MPa.

Ceglarska-Stefańska and Brzóska, (1998) conducted a study utilizing cubic samples to investigate the swelling/shrinkage behavior of both dry coal and pre-wetted coal during the processes of adsorption and desorption. Strain measurements were taken perpendicular to the coal's lamination. Their findings revealed that during the adsorption process, the "dry" coal exhibited a lower degree of swelling strain compared to the pre-wetted coal. In contrast, during desorption, both the dry and pre-wetted coals experienced a strain pattern characterized by an initial swelling followed by a subsequent shrinkage.

St. George and Barakat, (2001) conducted a study focusing on the volumetric deformation of Ohai coal from the South Island of New Zealand. Initially, they saturated a sample under 4 MPa of pressure for 8 hours to investigate swelling resulting from adsorption. The results indicated a swelling of 2.2% with CO2, 0.38% with CH4, 0.17% with N2 and a shrinkage of 0.05% with He. The desorption-induced shrinkage reached 2.1% for CO2, 0.435% for CH4, and 0.128% for N2.

Chikatamarla et al., (2004) found that the swelling potential of coal under gas pressure equal to 0.6 MPa is in descending order H2S > CO2 > CH4 > N2 (Figure 17).

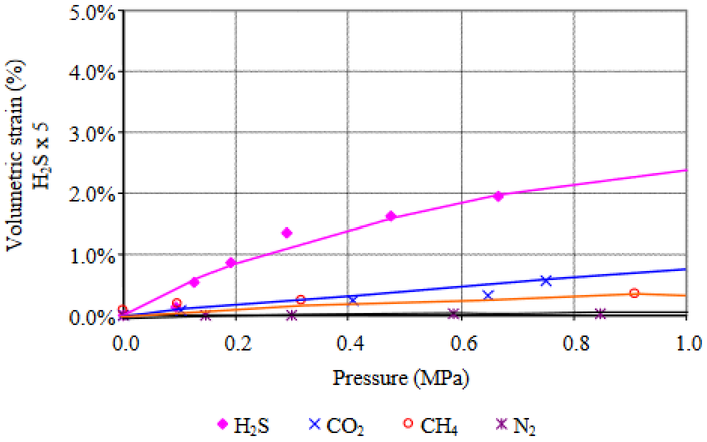

Figure 17 X-axis scale enlarged for comparing the strains at 0.6 MPa.(Chikatamarla et al., 2004)

Zutshi and Harpalani, (2004) conducted a study to assess the swelling of coal under the adsorption of CO2 and CH4 at a temperature of 45 °C, using coal samples from the USA. The results indicated that the effective strains resulting from adsorption were as follows: 1.1% for CH4 under 7.45 MPa (Figure 18), and conversely, a shrinkage of 0.26% occurred with He at a pressure of 10.34 MPa (Figure 19).

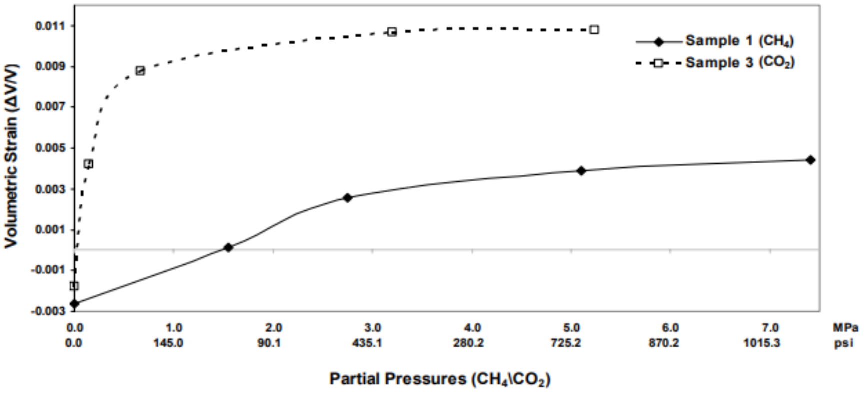

Figure 18 Adsorption induced swelling of coal subjected to CO2 and CH4 (Zutshi and Harpalani, 2004).

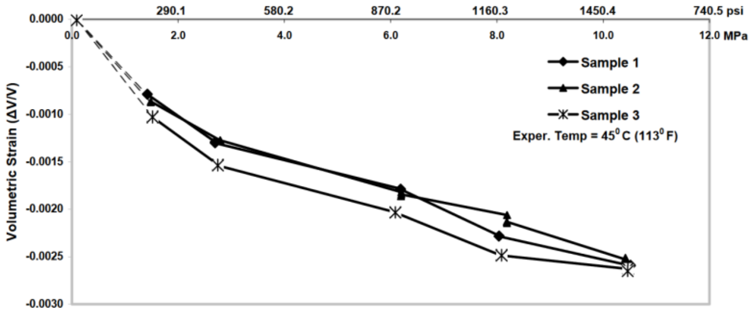

Figure 19 Adsortion induced swelling of coal subjected to He (Zutshi and Harpalani, 2004).

Robertson and Christiansen, (2005) conducted a study to measure the swelling of coal samples from Utah, USA, at a temperature of 26.7°C (80°F) and various pressures. For coal samples from the Anderson mine, the observed swelling strains were 2.13% with CO2 under 5.6 MPa, 0.48% with CH4 under 6.9 MPa, and 0.14% with N2 under 6.9. Meanwhile for coal samples from the Gilson mine, the measured linear swelling strains were 0.93% with CO2 under 5.4 MPa, 0.39% with CH4 under 6.9 MPa and 0.11% with N2 under 6.3 MPa (Figure 20).

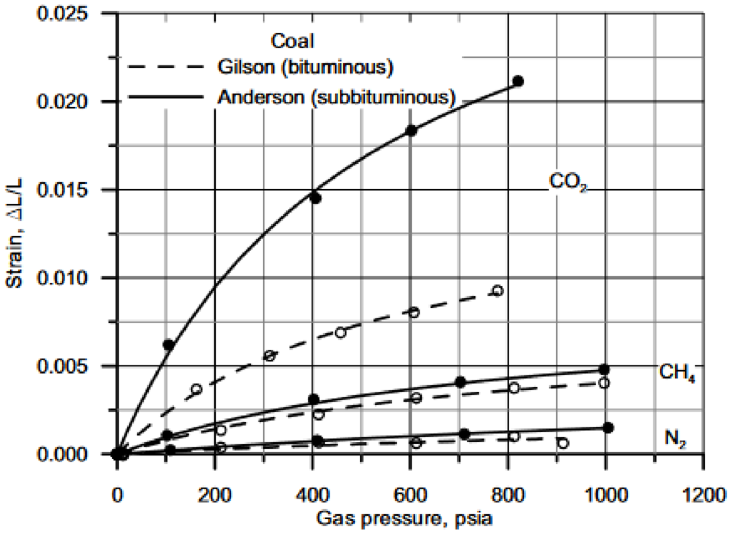

Figure 20 Adsorption induced swelling of coal subjected to different gases (Robertson and Christiansen, 2005).

(Day et al., 2008b) showed that the expansion and contraction of Australian bituminous coals in response to changes in pressure are entirely reversible. Interestingly, they observed that once the pressure exceeds 8-10 MPa, further increases have a negligible impact on the coal's swelling behavior. Up to that point, coal swelling appears to exhibit a nearly linear relationship with the amount of CO2 absorbed. Notably, significant variations in swelling were found between the perpendicular and parallel orientations with respect to the coal's bedding plane; expansion was 30-70% greater in the perpendicular direction compared to the parallel direction.

2.4.2.2.Adsorbed gas quantity and strains relationship

Several studies have examined the relationship between coal swelling strains and gas adsorption. For instance, Harpalani and Chen, (1995) conducted research using coal from the USA's San Juan Basin. They demonstrated a linear correlation between the volumetric strain of the coal matrix and CH4 adsorption, with a coefficient of 2 x 10^{-4} g/ml.

Similarly, Seidle and Huitt, (1995) investigated this phenomenon and observed that the coefficient linking matrix swelling and adsorbed gas concentration ranged from 1.87 x 10^{-5} ~ 4.7 x 10^{-5} g/ml for CO2.

Chikatamarla et al., (2004) expanded on these findings by studying various coal ranks, from subbituminous to medium-volatile coals from the Western Canadian Sedimentary Basin. They discovered that coal swelling strains were correlated with gas concentration across all coal types and gases.

Furthermore, Chikatamarla et al., (2004); Levine (1996); Robertson and Christiansen (2005) identified that the relationship between adsorbed gas and swelling strain in the coal matrix followed the Langmuir isotherm.

2.4.3.Permeability

2.4.3.1.Influence of stress

The stress sensitivity of permeability in fractured reservoirs is a widely recognized phenomenon. Cleats in coalbeds, which are natural fractures, also exhibit stress-sensitive permeability. Similar to how materials expand and contract with temperature changes, alterations in effective stress led to the deformation (expansion and contraction) of the coal matrix and to the opening and closing of cleats. These changes, in turn, cause fluctuations in coal permeability, with increases and decreases depending on the specific conditions.

Numerous studies have been conducted to comprehend the relationship between confining pressure, injection pressure, pore pressure, and stress conditions. Investigations by Somerton et al., (1975) revealed that coal permeability decreases by more than two orders of magnitude when increasing the confining pressure from 1.72 to 13.8 MPa (Figure 21). Dabbous et al., (1974) deduced that water and air permeability is reduced when increasing the overburden pressure. (Pomeroy and Robinson, 1967) studied the combined effect of pore pressure and confinement pressure increase and its effect on permeability. Their results showed that permeability increases with increasing pore pressure (injection pressure) and decreases with increasing confining pressure.

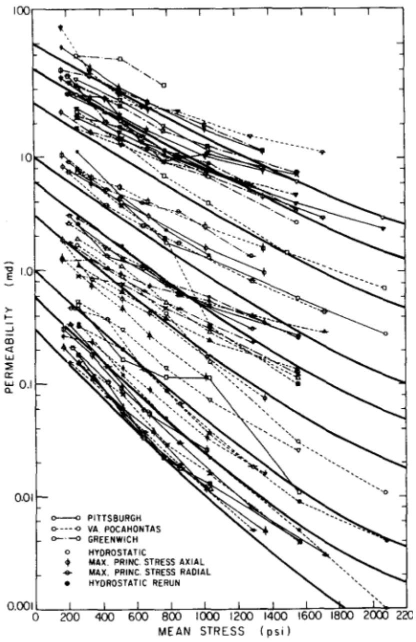

Figure 21 Permeability changes in coal specimens subjected to increasing confining pressure (Somerton et al., 1975)

2.4.3.2.Experimental evidence of permeability changes in coal

The expansion and contraction of the coal matrix has a direct impact on cleat aperture. When the matrix swells, the cleat aperture decreases, whereas during shrinkage, the cleat aperture increases, ultimately influencing permeability.

Initially, establishing the relationship between swelling/shrinkage and its impact on the permeability proved challenging. Somerton et al., (1975) observed that injecting CH4 resulted in lower permeability compared to N2 injection, deducing an average permeability decrease ranging from 20% to 40% (Figure 22) depending on the coal type due to molecular diameter or sorption of gas on coal fractured surfaces.

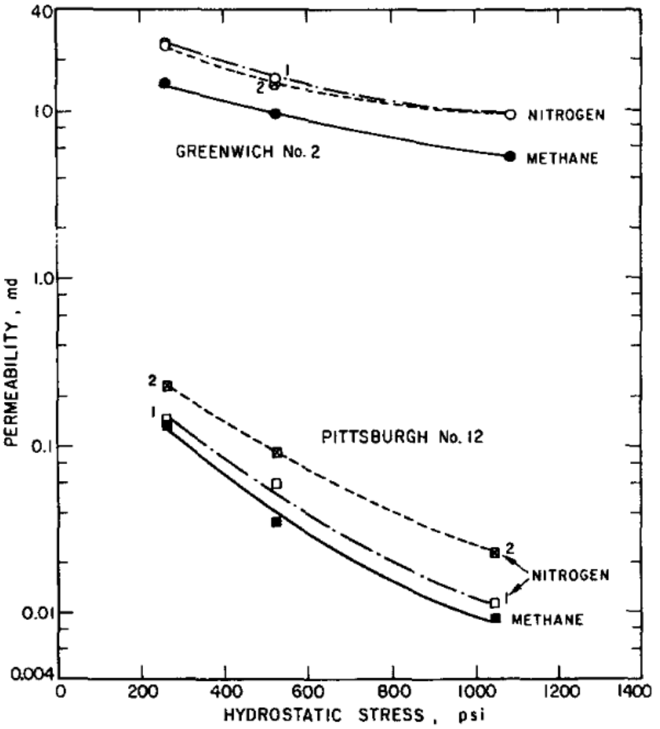

Figure 22 Permeability changes observed in coal samples subjected to CH4 and N2 respectively, as a function of the confining pressure (Somerton et al., 1975).

Harpalani and Zhao, (1989) studied the effect of gas desorption on permeability of coal samples from mines of the Piceance Basin and the Black Warrior Basin of the USA. The results showed that with CH4, permeability increases when gas starts to desorb from the coal matrix to the cleats.

Harpalani and Schraufnagel, (1990a, 1990b) studied the relationship between gas pressure, induced volumetric strain and permeability due to desorption of gas (decreased from 6.9 MPa to 0.1 MPa). They concluded that the shrinkage of coal matrix causes the permeability to increase significantly once the pressure falls below the desorption pressure (c.a. 4.1MPa) where the effect of matrix shrinkage becomes dominant, resulting in increased permeability, and so in a higher production of gas (Figure 23).

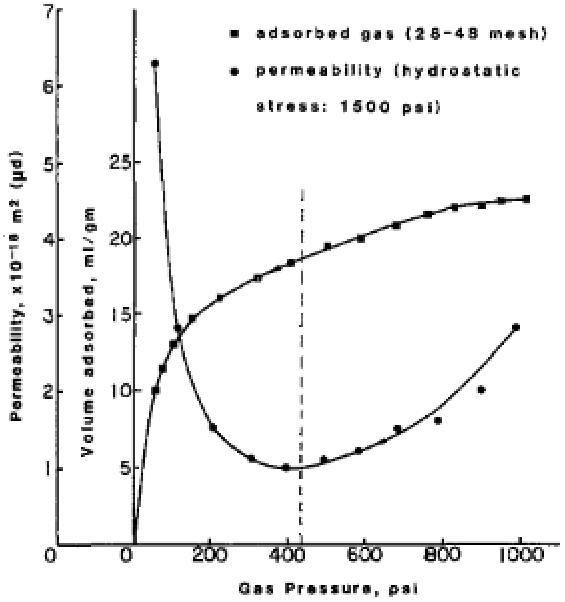

Figure 23 Variation in adsorbed gas content and permeability of coal as functions of CH4 pressure (Harpalani and Schraufnagel, 1990a).

Lin et al., (2008) measured permeability changes during the injection of N2, CH4, CO2, and mixtures of N2 and CO2, all conducted under an effective stress of 2.76 MPa. The findings revealed a ranking of permeability decrease, with N2 exhibiting the smallest decrease, followed by CH4, and then CO2.

In a study by Pini et al., (2009), permeability changes were investigated through the injection of He, N2, and CO2 at pressures ranging from 0.1 MPa to 8 MPa. The results revealed an increase in permeability as the effective pressure on the sample decreased. Furthermore, when adsorbing gases were introduced, a reduction in permeability occurred due to swelling, with CO2 exhibiting a more pronounced effect compared to N2.

Pan et al., (2010) investigated the influence of injecting CH4, CO2, and He under a pore pressure of 13 MPa on permeability. The results highlighted a notable reduction in permeability as a response to both confining pressure and pore pressure. This decline in permeability, caused by pore pressure, was directly linked to coal swelling induced by gas adsorption. It's worth noting that the measurements showed a decrease in permeability as pore pressure increased at constant effective stress, with the extent of the decrease depending on the specific gas utilized.

2.4.3.3.Permeability models for coal

Numerous efforts have been made to comprehend the changes of permeability during CBM production. Gray, (1987) is credited as one of the early researchers who ventured to elucidate the shifts in permeability associated with pressure depletion. His investigations revealed that these changes were influenced by two factors: effective stress increase and matrix shrinkage resulting from gas desorption. To address these variations, Gray proposed an empirical exponential relationship for estimating permeability under positive effective stress conditions represented in equation (2.23).

$$\sigma - \sigma_0 = \frac{v}{1-v}(p - p_0) + \frac{E}{1-v}\frac{\Delta\varepsilon_s}{\Delta p_s}\Delta p_s \qquad (2.23)$$

$$k = 0.001013e^{-0.714\sigma}$$

where p is the pressure, Δp_s is the change in sorption pressure, v is the Poisson ratio, E is the Young modulus, $\sigma - \sigma_0$ is the stress change, $\frac{\Delta\varepsilon_s}{\Delta p_s}$ is the strain caused by sorption pressure.

In a subsequent development, Sawyer et al., (1990) introduced the ARI model within the context of the GOMET simulator. This model takes into consideration not only matrix swelling and shrinkage but also gas concentration when assessing permeability. Importantly, this approach is considered more accurate and physically grounded compared to linking these effects solely to changes in pore pressure (Equation (2.24).

$$n = n_i\left[1 + C_p(p - p_\mathrm{i})\right] - C_m(1 - n_i)\left(\frac{\Delta p_i}{\Delta C_i}\right)(C - C_i)$$

with

$$\frac{\Delta p_i}{\Delta C_i} = \frac{p_{di} - 14.7}{C(p_{di}) - 14.7} \qquad (2.24)$$

$$\frac{k}{k_0} = \frac{n^3}{n_0^3}$$

where n is the porosity, Cp is the pore volume compressibility, Cm is the matrix compressibility, C is the average matrix gas concentration, p is the pressure, Δp_i is the maximum pressure change based on initial desorption pressure, ΔC_i is the maximum concentration change based on initial, p_{di} is the initial desorption pressure, and $C(p_{di})$ is the concentration at initial desorption pressure.

Puri and Seidle, (1992) introduced a model based on matchstick geometry. Their model's equation closely resembled one previously presented by McKee et al., (1988):

$$k = k_0 e^{-3c_f(\sigma - \sigma_0)} \qquad (2.25)$$

where σ is the hydrostatic pressure, σ_0 is the initial hydrostatic pressure, c_f is the cleat volume compressibility, k is the permeability, and k_0 is the initial permeability. Another equation was proposed by Seidle and Huitt (1995) where permeability is a function of porosity and pressure:

$$\frac{n}{n_0} = 1 + \left(1 + \frac{2}{n_0}\right)\varepsilon\left(\frac{Bp_0}{1 + Bp_0} - \frac{Bp}{1 + Bp}\right)$$

$$\frac{k}{k_0} = \frac{n^3}{n_0^3}$$

Based on the matchstick geometry concept, while assuming a constant reservoir volume, Harpalani and Chen, (1995) proposed a model to assess the variation in cleat porosity and permeability as a response to matrix shrinkage such as

$$\frac{k}{k_0} = \frac{1}{12}\frac{(1+2\frac{l_m \Delta p}{n_0})^3}{1-l_m \Delta p} \tag{2.26}$$

where k_0 represents the initial permeability, Δp represents the pressure difference, l_m represents the change in the matrix dimension and n_0 is the initial porosity.

Seidle and Huitt, (1995) proposed a model that relates the sorption induced strain and its effect on the permeability. This model expresses permeability as a function of pressure, Langmuir isotherm and porosity:

$$\frac{k}{k_0} = \left[1 + \left(1 + \frac{2}{n_0}\right) C_m V_E \left(\frac{Bp_0}{1+Bp_0} - \frac{Bp}{1+Bp}\right)\right]^3 \tag{2.27}$$

where B is the Langmuir constant.

Palmer and Mansoori, (1998) proposed a model aimed at simulating permeability changes in response to stress changes and matrix shrinkage. This model incorporates the Langmuir strain ε_L, allowing for micro-strain shrinkage even when there is no gas desorption, as demonstrated by (Wei and Zhang, 2010). Additionally, Palmer and Mansoori integrated a cubic relationship between porosity and permeability into their model:

$$n - n_0 = \frac{1}{M}(p - p_0) - (1 - \frac{K}{M}) \times \varepsilon_L \left(\frac{p}{p+P_\varepsilon} - \frac{p_0}{p_0+P_\varepsilon}\right) \tag{2.28}$$

$$\frac{k}{k_0} = \frac{n^3}{n_0^3}$$

where $\varepsilon_L, P_\varepsilon$ Langmuir type parameters.

One notable feature of this model is the occurrence of a permeability rebound at lower pressures, particularly prominent when a significant amount of gas has been desorbed. Mavor and Gunter, (2006) further developed the model introduced by Palmer and Mansoori to encompass enhanced coalbed methane (ECBM) recovery and carbon dioxide storage.

A comparative analysis conducted by Pekot and Reeves, (2003) between the ARI model and the Palmer and Mansoori model confirmed that they yield similar results in most cases. However, the Palmer and Mansoori model performs better in scenarios where swelling is not directly proportional to gas concentration.

Shi and Durucan, (2003a) developed a model based on a relation between permeability and stresses. This model differs from Palmer and Mansoori model where micro-strain occurs only in the case of adsorption/desorption of gas (Durucan et al., 2009; Shi et al., 2008; Shi and Durucan, 2004, 2003a):

$$n - n_0 = \frac{v}{1-v}(p - p_0) + \frac{E}{3(1-v)} \times \varepsilon_L \left(\frac{p}{p+P_\varepsilon} - \frac{p_0}{p_0+P_\varepsilon}\right) \tag{2.29}$$

$$k = k_0 e^{-3c_f(\sigma-\sigma_0)}$$

Robertson and Christiansen, (2008) introduced a model for coal that is based on a cubic geometric framework. They identified key factors influencing cleat width, including fracture compressibility, mechanical elasticity, and sorption-induced strain. Robertson and Christiansen claims that the factors significantly influence permeability changes in response to variations in pore pressure:

$$\frac{k}{k_0} = e^3\left\{C_0\frac{1-e^{\propto(p-p_0)}}{-\alpha}+\frac{3}{\mathrm{n}_0}\left[\frac{(1-2v)}{E}(p_r-p_0)\frac{\varepsilon_{max}}{p_L-p_0}\ln\left(\frac{p_L-p_r}{p_L-p_0}\right)\right]\right\} \tag{2.30}$$

Where α is the rate of change of fracture compressibility, ε_{max} is the linear strain for unconstrained sample, and p_L is the Langmuir pressure.

2.5.Numerical modelling of coal

2.5.1.Darcy scale models (continuum approaches)

Sampath et al., (2020) proposed a continuum scale hydromechanical single phase model for coal (Figure 24). This model includes the Langmuir adsorption isotherm, various transport mechanisms (Knudsen diffusion, slip flow), as well as swelling/shrinkage of coal matrix. The spatial and temporal analysis demonstrates that a larger fraction of matrix swelling occurs well before the coal matrix reaches its pressure equilibrium, confirming the fact that adsorption induced-swelling starts immediately with the coal-CO2 interaction.

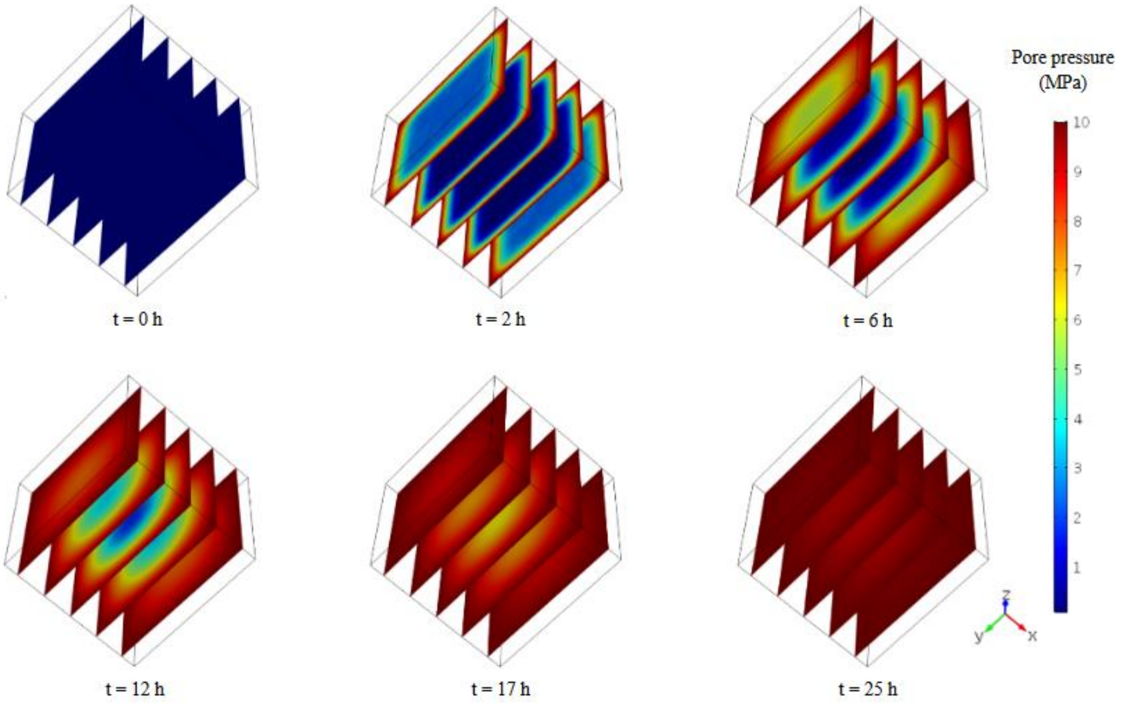

Figure 24 Simulation results showing the spatial and temporal distribution of CO2 diffusion-induced pore pressure in the coal matrix.(Sampath et al., 2020).

Wei et al., (2010) developed also a dynamic multicomponent transport (DMCT) model that deals with a multi component gas diffusion and flow in the coal. The coal matrix is represented as a cylindrical cell surrounded by fractures. The presented model has utilized the Shi and Durucan, (2003a) analytical solution to simulate the stress-dependent permeability.

Lanetc et al., (2023) presented a hybrid two-phase Darcy–Brinkman flow model (pore-scale-continuum approach). This model uses the Navier–Stokes solution in the resolved regions of the image and the continuum Darcy flow in the sub-resolved zones. The sorption processes are introduced by the Langmuir isotherm, while the transient nature of sorption is captured by the implicit combination of the Langmuir and pressure equations in the Darcy–Brinkman model. The surface diffusion is explicitly embedded in the proposed hybrid model by using the second Fick’s law. The impact of matrix swelling-shrinkage phenomenon on the coal porosity and absolute permeability is accounted for by using the Palmer–Mansoori analytical model.

Qu et al., (2012) developed a non-isothermal model. This model includes coal deformation, gas flow, thermal transport and is capable of calculating permeability with the effect of gas pressure and temperature. The sorption induced strain is defined in function of temperature. They conclude that the evolution of permeability is primarily affected by the evolution of swelling/shrinkage of the coal matrix under variable temperature and pressure.

Qu et al., (2014) has extended his previous model to include the constant confining pressure conditions. A Critical Swelling Area concept has been introduced which is the area of the coal matrix swelling at the permeability switching point, from reduction to rebound, when the external boundary starts to move outwards as the matrix swelling propagates to it (Figure 25). A thin elastic layer feature is implemented on COMSOL Multiphysics software to introduce a combination between matrix and cleat.

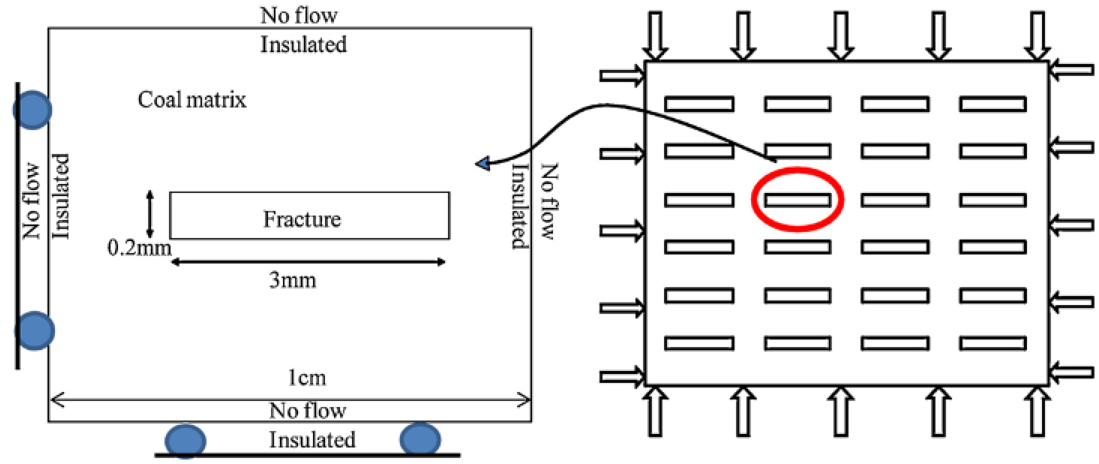

(a). Coal block with single matrix and fracture (b). Numerical model with stress-controlled boundary

Figure 25 Specifications of the numerical model proposed by (Qu et al., 2014). (a) Coal block with single matrix and fracture. (b) Numerical model with stress-controlled boundary.

Masoudian, (2013) and Masoudian et al., (2014) introduced a dual-porosity chemo-hydro-mechanical model that employs a quasi-steady state approach for approximating the matrix fracture transfer function. This model accounts for the detrimental impact of CO2 on elastic moduli and establishes a linear relationship between adsorbed gas and elastic moduli to assess this damage. The model integrates the gas flow equation with mechanical deformation through the volumetric strain rate. However, stress-strain states are calculated using two different analytical solutions. Once the flow equation is numerically solved, the mechanical subroutine is invoked, with mechanical calculations trailing one step behind the flow calculations, as outlined by Masoudian (2013). Their findings suggest that changes in elastic modulus have a direct effect on permeability.

Chen et al., (2019) introduced an explicit dual poroelastic mechanical continuum model for analyzing multi-phase flow and the transport of multiple chemical components in gas. Chen et al., (2019) conducted thorough verification and validation of this model by comparing it with pertinent analytical solutions and experimental data. Furthermore, they applied this model to investigate gas flow characteristics and structural alterations within coal. Their findings revealed that the changes in fracture porosity are not consistent and can be attributed to the interplay between effective stress and interactions occurring within the fracture-matrix system.

Chen et al., (2022a) introduced a 3D hybrid coupled model designed to efficiently and accurately simulate the interplay of flow, chemical reactions, and deformation processes within fractured reservoirs characterized by a multiscale fracture system, such as those found in coal and shale formations. This hybrid model combines two modeling approaches: a dual continuum approach to describe the natural fracture network and coal matrix, and a discrete fracture approach to explicitly represent the large fractures (Figure 26). The researchers conducted a comprehensive evaluation of the model's reliability and implementation accuracy, comparing it against both an analytical solution and a laboratory experiment. The simulation results clearly demonstrate the model's capability to effectively capture the influence of large-scale fractures and the coupled behavior during CO2 injection in coal reservoirs.

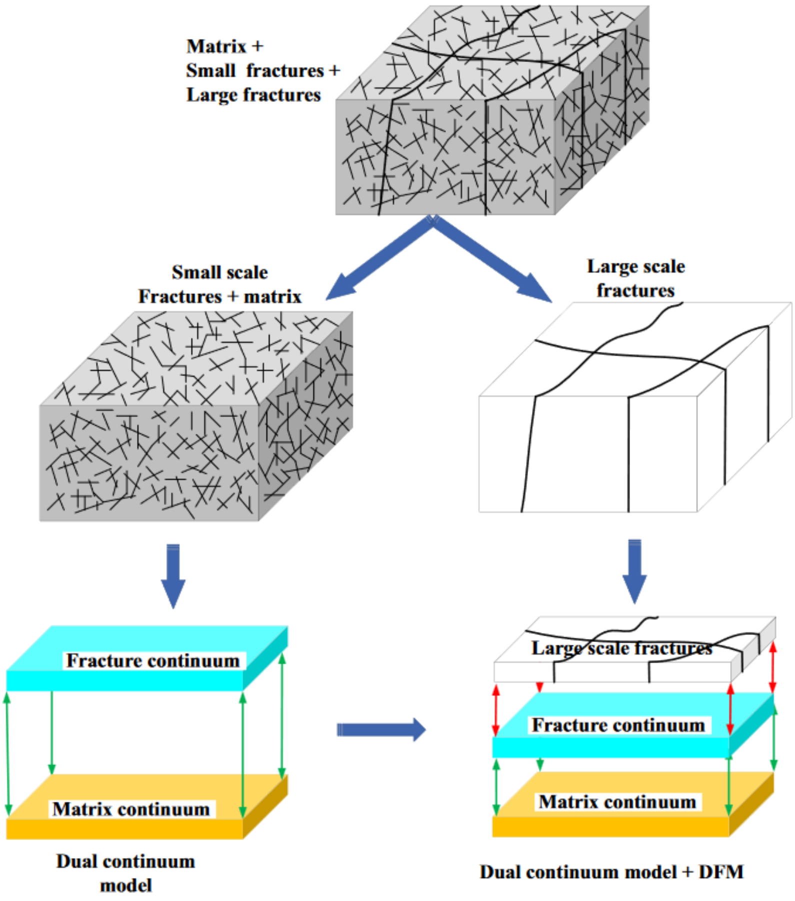

Figure 26 Conceptual development process for the hybrid dual continuum and discrete fracture model proposed by (Chen et al., 2022a).

2.5.2. Pore scale models

Continuum-scale models have found widespread use in the prediction of large-scale transport processes relevant to the field of engineering. However, these models typically employ computational elements with an average size much larger than the typical pore dimensions of porous media. As a result, the microscale heterogeneity of porous media is often overlooked in continuum models. While effective transport properties and their spatial heterogeneity at larger scales are recognized as significant factors influencing transport processes, it is important to acknowledge that microscale heterogeneity also plays a crucial role. Pore-scale processes have a profound impact and can even dominate system performance, durability, cost, and safety.

Pore-scale models offer a direct approach to solving transport processes within realistic porous structures. Pore-scale simulations explicitly resolve the microscopic porous structures of the media, obviating the need for a priori phenomenological parameters. These models yield detailed distributions of crucial variables at the pore scale, establishing a direct connection between complex transport processes and the actual porous structures. This deeper understanding of the relationships between structures, processes, and performance is a notable advantage of pore-scale modeling.

The effectiveness and efficiency of pore-scale modeling rely on four key components:

1. Precise characterization of porous structures and the detailed distribution of various components.
2. Creation of efficient numerical methods to solve the governing equations and the execution of pore-scale modeling, enabling the establishment of physicochemical models that describe transport phenomena within porous media.
3. Examining the temporal and spatial evolutions of relevant variables to gain a profound understanding of the underlying mechanisms. This analysis also investigates the impact of porous structures and interfacial characteristics on transport processes.
4. Building on pore-scale results or upscaling them to a continuum-scale, this step involves modifying porous structures, physicochemical properties, or operational conditions. These modifications are aimed at improving, altering, or controlling transport processes within porous media, ultimately leading to enhanced system performance.

2.5.2.1. Lattice Boltzmann models

The lattice Boltzmann method (LBM) is a computational technique used for simulating fluid flow and transport processes. It is based on kinetic theory and discretizes space into a lattice grid. The LBM is a mesoscale approach where fluid particles move through a series of discrete lattice nodes, and collision rules are used to simulate the macroscopic behavior of the fluid. It is particularly useful for simulating flow at the pore scale, but it doesn't explicitly model the pore structure. Instead, it focuses on simulating fluid dynamics within a grid, and it is often used for complex flows and interactions.

Peng et al., (2018) introduced a double-distribution Lattice Boltzmann model designed for solving the coupled generalized Navier-Stokes equation and advection-diffusion equation. This model was specifically developed to address the gas-solid dynamic adsorption process in the context of multicomponent gas migration within unconventional reservoirs. The simulation results indicate that, under consistent parameter conditions, both the rate of gas diffusion within the porous material and the size of the region associated with dynamic adsorption equilibrium increase as the matrix porosity/permeability rises. Similar outcomes are observed with higher saturation adsorption levels or lower Langmuir pressures. It is crucial to note that this model does not incorporate any hydromechanical coupling.

Zhao and Wang, (2019) introduced a multi scale lattice Boltzmann method for simulating flow at the pore scale. They utilized the local rate of mechanical dissipation to determine the appropriate Representative Elementary Volume (REV). Subsequently, they employed the LBM to simulate seepage flow at the REV scale. The results of the REV scale simulation, when compared with those obtained at the pore scale, provided a satisfactory solution, with consistent relative errors remaining below 6%. It's important to note that the model does not describe complete hydromechanical coupling, as it does not consider swelling or shrinkage effects.

Li et al., (2023) developed a lattice Boltzmann model that takes into account surface adsorption and diffusion effects. This model encompasses various gas flow mechanisms, including viscous flow, enhanced gas slippage (where surface diffusion plays a role in enhancing gas slippage), and surface diffusion itself. The study's findings reveal that in micropores (<2 nm) and mesopores (2–50 nm), the presence of adsorbed gas influences bulk gas flow velocity. Specifically, at low pressure, this effect leads to an increase in flow velocity, whereas at high pressure, it results in a decrease. Notably, it is important to mention that this model does not incorporate full hydromechanical coupling, nor Knudsen diffusion or molecular diffusion.

2.5.2.2.Pore network models

To maintain a manageable computational cost, describing fluid flow through porous media can be achieved through Pore-Network (PN) models. These models simplify the complex pore structures by representing them as interconnected pores, resulting in a reduced number of variables compared to LBM models. So far, only a limited number of studies have explored the integration of PN models with mechanical models, with notable contributions from (Jing et al., 2001; Nakase et al., 1999; Tarumi, 1988). While these investigations have demonstrated success, they have predominantly been limited to 2D geometries.

A noteworthy 3D pore-scale approach is the Pore-Scale Finite Volume (PFV) formulation initially designed for modeling the viscous flow of either incompressible or compressible pore fluids. This technique, introduced by (Chareyre et al., 2012), involves decomposing the pore space into pore elements and local conductance. The discretization of the pore space is carried out using Regular Triangulations and their dual Voronoi graphs, as depicted in Figure 27.

Coupled to the discrete element method (DEM), PFV models has yielded successful outcomes in addressing single-phase flow challenges and associated hydromechanical(HM) couplings, as evidenced by the studies conducted by (Catalano et al., 2014; Scholtès et al., 2015). An extension of the PFV approach, referred to as the "Two-phase Pore-scale Finite Volume - Discrete Element Method" (2PFV-DEM), was recently introduced by Yuan et al. in 2016 to deal with multi-phase flow. Recent works by (Sweijen et al., 2017; Yuan and Chareyre, 2017), highlight the capability of 2PFV-DEM in effectively addressing two-phase fluid-related challenges. This development marks a significant advancement in the modeling and simulation of such complex fluid scenarios.

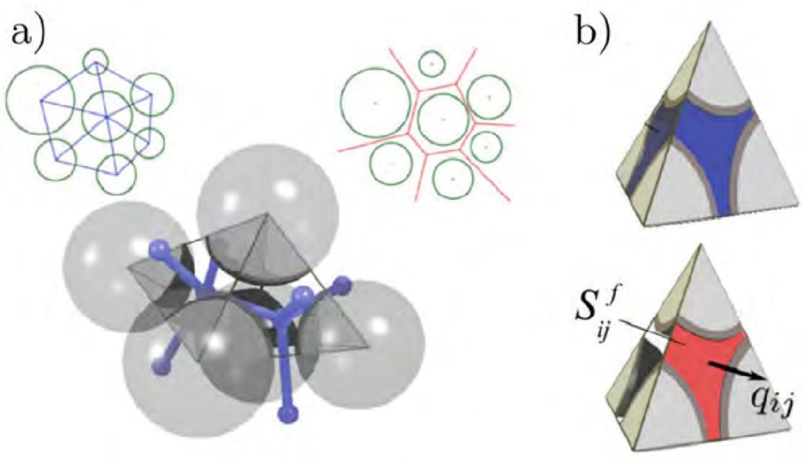

Figure 27 DEM-PFV model: a) discretization of the pores through a regular triangulation and the dual Voronoi's graph representing their interconnection, b) elementary fluid domain (tetrahedron) in a triangulated sphere assembly. Images from Chareyre et al. (2012) and Scholtès et al. (2015).

2.5.2.2.1.Discrete element method

The discrete element method (DEM), also called distinct element method, pioneered by (Cundal & strack, 1979) enables the study of the mechanical behavior of particulate systems based on an explicit integration of Newton's second law of motion. The medium is modeled as a collection of interacting particles subjected to forces defined through specific force displacement laws to produce representative emergent macroscopic behaviors at the scale of the assembly. These laws can be adapted depending on the material to model by combining elasticity, plasticity, or viscosity components. For instance, cohesive frictional materials such as rocks can be modelled through elastic-cohesive-frictional force-displacement laws as defined in the bonded particle model (BPM) proposed by (Scholtès and Donzé, 2013). Thanks to their capability, DEM models can also be used to model fractured rocks as illustrated by the model proposed by (Scholtès et al., 2011) for coal which enables to incorporate discontinuity surfaces within the particulate system (Figure 28).

As mentioned in section 2.5.2.2, the DEM has been extended to describe HM coupling in both saturated and partially saturated media by coupling it to the PFV method. The DEM-PFV approach has been since successfully applied to describe HM couplings in rock subjected to hydraulic fracturing processes (Papachristos et al., 2017), as well as thermo-hydro-mechanical processes (Caulk et al., 2020).

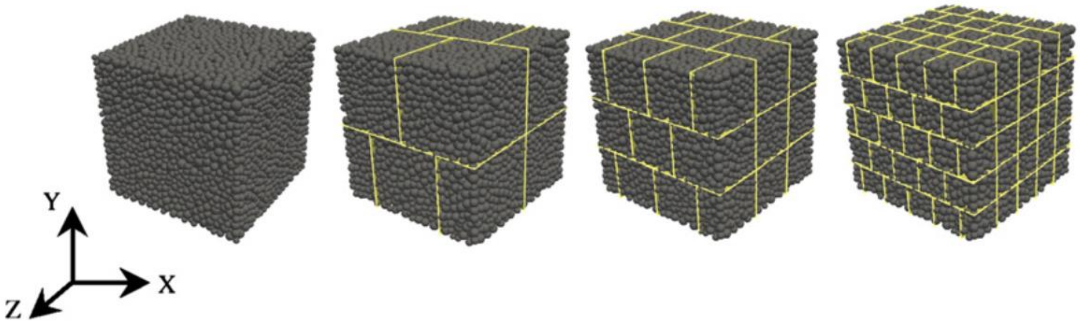

Figure 28 Four cubic samples of identical size (L=60 mm) and discretization (L/d=22) built up with an increasing fracture density (0, 1, 2 and 4 cleats per length) (Scholtès et al., 2011).

2.6.Recommendations

Recent experimental results, theoretical perspectives, and numerical models have greatly enhanced our understanding of coal behavior. However, despite these advances, several questions remain unanswered regarding coal's physical, chemical, and mechanical attributes, as well as its response to gas injection (such as carbon dioxide or methane). For instance:

- Comprehensive multi-scale hydro-mechanical models capable of concurrently addressing various gas diffusion mechanisms within the matrix, Darcy-type flow in the cleats, and the correlation between coal matrix swelling/shrinkage and permeability/porosity evolution are notably absent.
- Estimating the volume of gas that can be practically stored in a coal seam and determining its state at injection (gaseous, liquid, or supercritical) remains a challenge.
- While selecting suitable cap rocks for gas storage scenarios is conceivable, their reactivity to carbonic acid remains uncertain. Could a coal seam, with low permeability and propensity for swelling, serve as a cap rock rather than a reservoir?
- The role of minerals, particularly clays (as discussed by Busch et al., 2008), in acting as preferential adsorption sites or potential impediments to diffusion and gas storage due to their untimely occupation of porosity requires further exploration.

Coal, with its inherent complexity, remains a puzzling geological material, necessitating comprehensive research to match the understanding and predictability achieved with other porous rocks, such as sandstones and carbonates, which are frequently utilized for CO2 storage in aquifers. Of particular significance is addressing the first point: the need for the development of multiscale hydromechanically coupled models. Such models are scientifically crucial as they would consider the various transport mechanisms at work within coal. This approach is vital for achieving a profound understanding of CBM production and the intricacies associated with it. The following chapters present our contribution toward this objective and resume the work performed during the last 4 years.

Chapter 3

Pore-scale hydro-mechanical modeling of gas transport in coal matrix

Chapter 3 : Pore-scale hydro-mechanical modeling of gas transport in coal matrix

Ahmad Mostafa[1], Luc Scholtès[2], Fabrice Golfier[1]

[1]Université de Lorraine, CNRS, Laboratoire GeoRessources, Nancy, France

[2]Université Clermont-Auvergne, CNRS, IRD, OPGC, Laboratoire Magmas et Volcans, Clermont-Ferrand, France

Corresponding author email: ahmad.mostafa@univ-lorraine.fr

3.1.Introduction

Coal bed methane (CBM), also known as coal seam gas (CSG), has drawn much attention lately as an alternative energy resource. Production curves of CBM reservoirs are very different, however, from the ones of hydrocarbon conventional reservoirs (Liu et al., 2011). As emphasized by several studies (Li et al., 2017; Mostaghimi et al., 2017b, 2016; Privalov et al., 2020; Wang et al., 2018), transport and poromechanical properties of coal are strongly driven by topological and morphological features of its pore space.

Coal is fractured by nature; it is a dual porosity/permeability system made up of a porous matrix surrounded by fractures known as cleats (Figure 29, scale II). The orientation of this quasi-orthogonal cleat network including tensile fractures or face cleats, and compressive and strike-slip fractures or butt cleats, depends on the principal stress' directions (Laubach et al., 1998) and provides preferential pathways for fluid flow with fracture apertures up to 100 microns. In contrast, methane gas is stored within the low porosity coal matrix with pore sizes generally varying from a few to several dozens of nanometers (Li et al., 2017; Wang et al., 2018).

The cleat-matrix system compartmentalizes the transport and mechanical properties of coal. Knudsen and surface diffusions prevail in the nanometer-sized pores of the matrix, while molecular diffusion and two-phase Darcy flow occur mainly within the cleat network. All these transport mechanisms induce mechanical couplings related to both (i) the pore pressure changes which may alter the effective stress and consequently impact the bulk volume of the coal and, (ii) the sorption processes which contribute to swell or shrink the coal matrix (Pini et al., 2009; Wang et al., 2011). Indeed, coal can sorb various gases including CO_2, CH_4 and N_2, and the adsorption of these gases induces swelling strains (Ceglarska-Stefańska and Czapliński, 1993; Ceglarska-Stefańska and Zarębska, 2002; Pan and Connell, 2007). The magnitude of adsorption-induced deformation depends on the pores structure as well as on the nature of the gas adsorbed. It is well known for instance that the swelling is much higher with CO_2 than with CH_4 (Brochard et al., 2012), hence advocating the development of enhanced coal bed methane (ECBM) technology combining CBM recovery and CO2 sequestration.

If many experimental studies have attempted to accurately determine this volumetric deformation rate (Majewska et al., 2010) and have given precious insights into the changes in pore size distribution during adsorption/desorption processes, they did not completely succeed to capture the dynamics of mass transfer within the cleat-matrix system since measurements are generally carried out at equilibrium (Wang et al., 2018). Also, coal measurements are strongly affected by sample preparation, material composition, environment, and methodology (Mostaghimi et al., 2017b).

The inherent couplings between the physical processes at stake and the multiscale features of coal need to be explored further to better assess the macroscopic response of the coal matrix and the sorption induced volumetric deformation. If pioneering works (see for instance the review by (Liu et al., 2011)) have focused on permeability models using continuum (Connell, 2016; Guo et al., 2016) or dual-porosity approaches (Bertrand et al., 2017; Ma et al., 2017; Perrier et al., 2018; Wu et al., 2010), much attention has been paid in the last years to study the hydro-mechanical (HM) behavior of coal matrix at the pore-scale. For instance, Liu et al. (Liu and Mostaghimi, 2017) have derived a model based on the lattice Boltzmann method taking into account fluid-rock interactions with permeability and porosity variations to investigate the reactive transport of CO_2-saturated brine in coal fractures. Youjun and Vafai, (Youjun and Vafai, 2017) have simulated fluid flow in pores using a digital SEM image of a coal rock sample. More recently, Sampath et al. (Sampath et al., 2020) have developed a HM model taking into account CO_2 diffusion and adsorption-induced mechanical deformation in coal matrix. To the best of our knowledge, however, a coupled HM model that incorporates the different transport mechanisms combining the diversity of nanoscale processes with the complexity of pore network topology has never been derived for coal matrix.

In this work, we propose a 3D pore-scale model for coal matrix based on a pore network model (PNM) describing gas transport coupled to a discrete element model (DEM) describing the mechanical behavior. The model is based on the framework of the pore scale finite volume (PFV) scheme implemented in the open-source platform YADE DEM (Šmilauer et al., 2015). The DEM-PFV coupled approach was initially designed for upscaling fluid flow in granular materials (Chareyre et al., 2012) and has been afterward used to describe hydro-mechanical processes in both soils (Catalano et al., 2014; Scholtès et al., 2015) and rocks (Papachristos et al., 2017). Lately, Caulk et al. (Caulk et al., 2020) extended its capability by incorporating heat transfer to the scheme and the associated possibility to describe thermo-hydro-mechanical processes. Here, we go further by introducing mass transport and sorption induced deformation processes to its formulation.

In summary, the equations governing the transport and HM schemes are first presented and derived accordingly to the geometric and numerical characteristics of the proposed model. Then, a validation exercise is provided where each component of the transport model is challenged against analytical solutions of Fick's law considering either pore-pore, pore-particle or particle-particle diffusion mechanisms. Finally, the coupled HM model is used to simulate an experiment from the literature where a coal sample experience swelling due to gas adsorption.

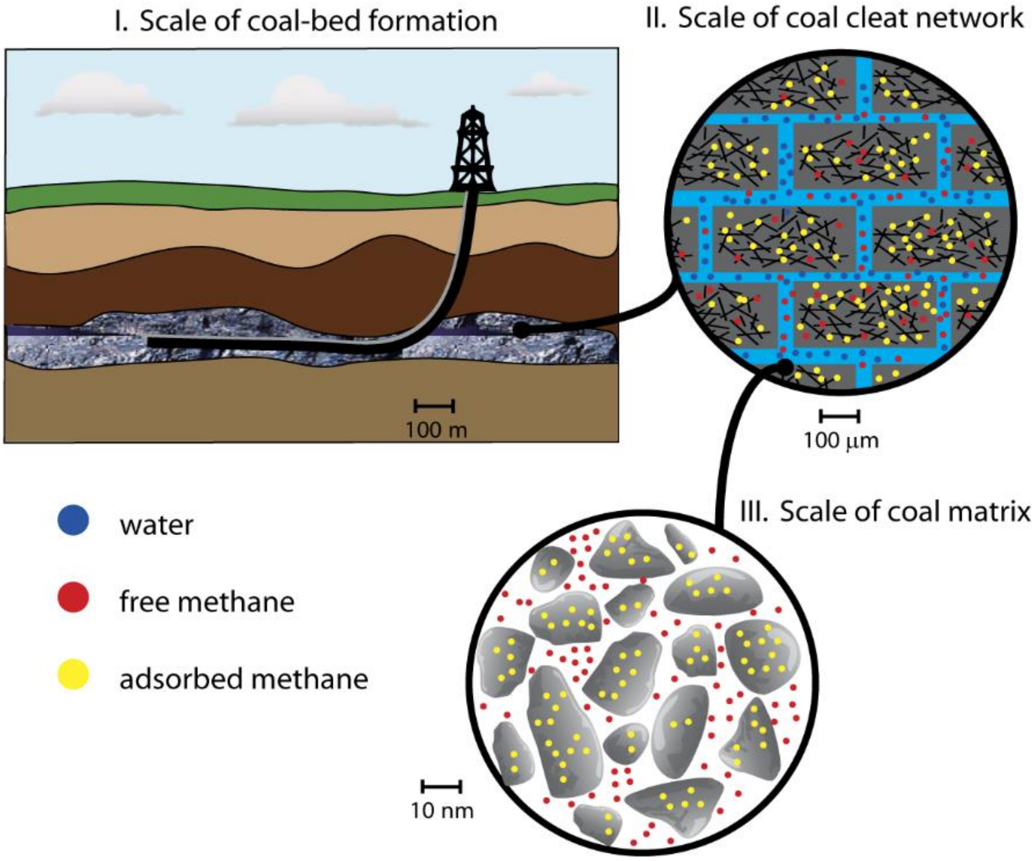

Figure 29 Different scales of a coalbed reservoir.

3.2.Methodology

The porous coal matrix is modeled based on the assumption that the solid phase is made up of densely packed spherical particles bonded one with another, and the pore space idealized as a network of interconnected pores. The following sections detail the mechanical and transport models, the assumptions made and their respective implementation in YADE DEM.

3.2.1. Mechanical scheme

The discrete element method (DEM) represents the mechanical behavior of a particulate system as a collection of interacting objects, where interactions follow predefined constitutive laws. Similar to the original DEM scheme (Cundall and Strack, 1979), the iterative scheme implemented in the Yade open DEM software integrates particle positions through time according to Newton's second law of motion, which can be written for the whole system as:

$$\mathrm{M}\ddot{\mathrm{x}} = \mathrm{f} \tag{3.1}$$

with $\ddot{\mathrm{x}}$ the vector containing each particle acceleration, M the diagonal matrix of particle masses, and f the vector containing the total forces applied on the particles. The explicit time stepping scheme integrates the particle acceleration from the current step to update the particle position at the next step through a finite difference scheme (see (Smilauer V. et al., 2015) for details of the implementation). The inter-particle forces result from the contribution of two force components, defined respectively in the normal and in the tangential (shear) directions of the contact. The normal force between two interacting particles *a* and *b* is evaluated according to:

$$\mathrm{F^n} = \mathrm{k^n}\, \Delta\mathrm{D} \tag{3.2}$$

$$k_n = E_{eq} \frac{R_a R_b}{R_a + R_b} \tag{3.3}$$

where k^n is the normal stiffness, E_{eq} an equivalent elastic modulus, R_a and R_b the radii of *a* and *b* respectively, and $\Delta D = D - D^{eq}$ is the displacement between *a* and *b* computed from the equilibrium distance D_{eq} and the current distance D. In compression, F_n can increase indefinitely. In tension, a maximum acceptable force is defined as a function of the interparticle tensile strength t such as $F_{n,max} = t\, A_{int}$, with $A_{int} = \pi[min(R_a, R_b)]^2$. If $F_n \geq F_{n,max}$, tensile rupture occurs.

The shear force is computed incrementally such as:

$$F_s = \{F_s\}_{updated} + k_s \Delta u_s \tag{3.4}$$

with k_s the shear stiffness defined as $k_s = P k_n$ with $0 < P < 1$, and Δu_s the relative incremental tangential displacement. F_s can increase up to a threshold value defined by a Mohr-Coulomb type criterion such as $F_{s,max} = c + F_n \tan(\varphi)$, with *c* the interparticle cohesion, and φ the interparticle friction angle. If $F_s \geq F_{s,max}$, shear rupture occurs.

In addition, the integration of the equations of motion being done through an explicit scheme, a local non viscous damping is used to dissipate kinetic energy and to ease the convergence of the simulated system toward quasi-static equilibrium (see (Duriez et al., 2016) for details). Basically, the resultant force $\vec{F} = \overrightarrow{F_n} + \overrightarrow{F_s}$ considered in Newton's second law of motion is damped by a force $\overrightarrow{F^d}$ defined as:

$$\overrightarrow{F^d} = -\alpha\; sign\left(\sum \vec{F} \,.\left(\vec{v} + \frac{\Delta t^m}{2} \vec{a}\right)\right) \sum \vec{F} \tag{3.5}$$

with α a damping coefficient ($0 < \alpha < 1$), $\vec{v}$ and $\vec{a}$ the velocity and acceleration of the particle respectively, and Δt^m the mechanical time step.

3.2.2.Mass transport model

The diffusion of gas molecules within coal is rather complex due to the multi-scale architecture of the material, with pore sizes varying over several orders of magnitude (Jing et al., 2017b). Theory of gas transport in porous media has a long history from the simple Fick's law for binary systems, to the Stefan-Maxwell equations for multicomponent mixtures and ultimately, the Dusty-Gas Model, based on the Chapman-Enskog kinetic theory and including the couplings between the various mechanisms (Reinecke and Sleep, 2002; Thorstenson and Pollock, 1989). Indeed, different transport modes manifest and drive gas migration in nanoporous media, depending on the pore size and on the flow regime (Do, 1998):

(i) Viscous flow in which displacement of molecules is induced by the mean velocity and governed by the total pressure gradient which acts as driving force.

(ii) Molecular or continuum diffusion where molecular-molecular collision prevails. In the gas mixture, each species moves relative to each other, and the driving force is the molar fraction gradient for an isothermal system.

(iii) Knudsen diffusion in which molecule-wall collisions dominate compared to collisions between molecules. Contrarily to molecular diffusion, each species moves independently from each other. The driving force here is the partial pressure gradient, which reduces to the total pressure gradient for a single species gas flow.

(iv) Surface diffusion in which adsorbed molecules moves along solid surface (pore walls) from one adsorption site to another (Choi et al., 2001).

These different transport mechanisms may compete and combine in a complex way. The relative magnitude of collisions between molecules relative to collisions between molecules and walls (molecular vs Knudsen diffusion) is classically expressed through the dimensionless Knudsen number K_n, defined as the ratio between the molecular mean free path length ∩ which is a function of pore pressure, and the mean pore diameter d. For nanoporous material such as coal, and at low pore pressures, $K_n \gg 1$ typically, meaning that Knudsen diffusion generally prevails.

In the present study, we assume that water was previously expelled from coal matrix (residual water is expected to be trapped in the smallest pores that do not participate to flow) so that single-phase gas flow occurs within the pore network. The gaseous mixture is only composed of methane (an ideal gas assumption is employed) and a part of gas is sorbed on the coal solid phase. Due to the very low permeability of the matrix and considering single-species gas phase, only Knudsen and surface diffusions are thus considered (Figure 30a).

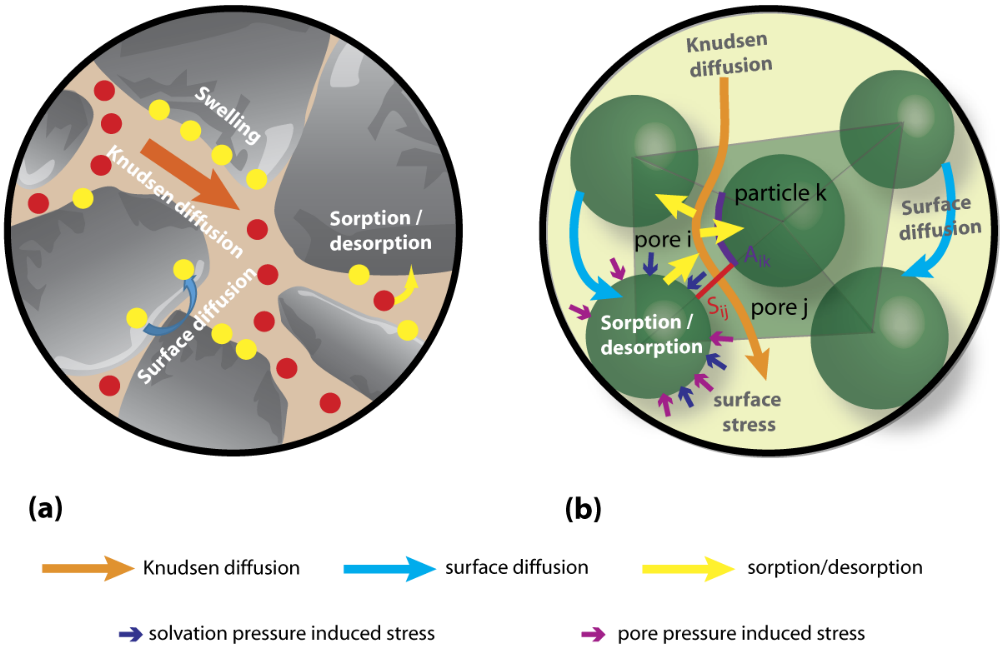

Figure 30 Mass transport and associated diffusion mechanisms in a) coal matrix, b) DEM-PFV model.

The DEM-PFV approach discretizes the pore space of the particle assembly into tetrahedra built from a weighted Delaunay triangulation of the particles' centers (Figure 30b). Each tetrahedron contains both a solid fraction resulting from the intersection between the tetrahedron and the associated vertex spheres, and a fluid fraction (the pore) resulting from the remainder of the tetrahedron volume. Each pore is thus connected to 4 neighboring pores and is in contact with 4 particles through surface areas where mass transport occurs by diffusion.

3.2.2.1.Mass balance equation for pores

Gas molecules are transported from one pore to another and are adsorbed/desorbed from and to the solid particles.

Let V_f be the volume of a pore *i* saturated with fluid (gas). Integrating the continuity equation in pore *i* gives:

$$\int_{V_f} \frac{\partial c_i}{\partial \mathrm{t}} dV + \int_{V_f} \bar{\nabla}.\bar{\mathrm{J}}_{pore,i} dV \ = 0 \tag{3.6}$$

where c_i is the concentration of gas in pore i, and $\bar{J}_{pore,i}$ represents the gas fluxes coming in and out of pore i.

Applying the divergence theorem to Equation (3.6) gives:

$$\int_{V_f} \frac{\partial c_i}{\partial t}.dV + \int_{\partial V_f} \bar{J}_{pore,i}.\bar{n}dS \ = 0 \tag{3.7}$$

Since each pore *i* is connected to 4 neighboring pores and in contact with 4 particles, the contour surface of each pore can be calculated as:

$$\partial V_f = \sum_{j=1}^{4} \partial V_{pore,i-pore,j} + \sum_{k=1}^{4} \partial V_{pore,i-particle,k} = \sum_{j=1}^{4} S_{ij} + \sum_{k=1}^{4} A_{ik} \tag{3.8}$$

with S_{ij} and A_{ik} the intersection surface areas between pore *i* and pore *j*, and between pore *i* and particle *k* respectively.

In our modeling approach, Knudsen diffusion describes the pore-pore diffusion fluxes and adsorption/desorption describes the pore-particle diffusion fluxes (Figure 30). Equation (3.7) can then be written as follows:

$$\int_{Vf} \frac{\partial c_i}{\partial \mathrm{t}} dV = -\sum_{j=1}^{4} \int_{S_{ij}} \bar{J}_{ij}^{K}.\bar{n}dS - \sum_{k=1}^{4} \int_{A_{ik}} \bar{J}_{ik}^{ad}.\bar{n}dS \tag{3.9}$$

where $\bar{J}_{ij}^{K}$ is the Knudsen diffusion flux between pore i and pore j, and $\bar{J}_{ik}^{ad}$ is the adsorption/desorption flux between pore *i* and particle k.

3.2.2.1.1.Knudsen diffusion

For a single-species phase flow along a straight circular capillary tube, the Knudsen diffusion flux can be defined as (Do, 1998):

$$\bar{J}^{K} = -D^{K}\bar{\nabla}c \tag{3.10}$$

$$\bar{J}^{K} = -D^{K}\frac{1}{RT}\bar{\nabla}p$$

with $p = cRT$ the gas pressure, R the gas constant (j/mol/k) and T the absolute temperature (K). The Knudsen diffusion coefficient D^K (m^2/s) is given by:

$$D^{K} = \frac{2r}{3}\sqrt{\frac{8RT}{\pi M_g}} \tag{3.11}$$

with r the pore hydraulic radius, and M_g the molar mass (kg/m^3).

The Knudsen flux may thus be written in terms of concentration between pore i and pore j such as:

$$\overline{J_{ij}^{K}} = -\frac{2r}{3}\sqrt{\frac{8RT}{\pi M_g}}\;\bar{\nabla} c_{ij} \tag{3.12}$$

with r computed as proposed by (Chareyre et al., 2012) in the PFV scheme. Then the spatial integration of Equation (3.12) between pores i and j gives:

$$\int_{S_{ij}} \bar{J}_{ij}^{K}.\bar{n}dS = -\frac{S_{ij}}{L_{ij}}\frac{2r}{3}\sqrt{\frac{8RT}{\pi M_g}}\left(c_j^t - c_i^t\right) \tag{3.13}$$

where L_{ij} is the distance between the centers of pore i and pore j.

3.2.2.1.2.Sorption

Sorption generally refers to the transport and attachment of a solute to the surface of a solid phase. Sorption processes are usually investigated at equilibrium through isotherms that relate the amount of adsorbed solute to the bulk concentration at constant temperature. In our modeling approach, we define kinetics formulations balancing the relative rates of adsorption and desorption (Raoof et al., 2012).

➢ **Linear first order sorption**

Linear sorption is characterized by an infinite number of sites on the particles' surfaces. As a result, solid particles can adsorb an infinite number of gas molecules according to the following relation:

$$\frac{\partial s}{\partial t} = \left(K_{att}c - K_{det}s\right) \tag{3.14}$$

where s (mol/m^3) is the amount of solute adsorbed onto the solid phase surface, c (mol/m^3) is the concentration of solute in the mobile phase (gas), K_{att} and K_{det} are respectively the adsorption and desorption coefficients defining the rate of adsorption/desorption, and t is the time (s). At equilibrium we recover the linear relationship:

$$K_d = \frac{K_{att}}{K_{det}}. \tag{3.15}$$

$$\text{where } \frac{\partial s}{\partial t} = 0 \text{ then } s = \frac{K_{att}}{K_{det}}c = K_d.c \tag{3.16}$$

➢ **Langmuir sorption**

If adsorption is limited by the number of sites on the solid surface (Liu et al., 2019), the following nonlinear relation can be used:

$$\frac{\partial s}{\partial t} = \frac{s}{s_{max}}K_{det} - \left(1 - \frac{s}{s_{max}}\right)K_{att}c \tag{3.17}$$

where the sorption is proportional to the number of available sites $\left(1 - \frac{s}{s_{max}}\right)$, s_{max} being the maximum amount of sorbed concentration. At equilibrium, we recover:

$$\frac{\partial s}{\partial \mathrm{t}} = 0, \text{then } \frac{s}{s_{max}} = \frac{K_d . c}{1+K_d c} \tag{3.18}$$

In our model, the diffusion fluxes between pores and particles can thus be described either by the linear relation of Equation (3.16) or by the nonlinear relation (Langmuir isotherm) of Equation (3.18). For instance, the spatial integration of the pore-particle diffusion flux between pore *i* and particle *k* in the case where it is governed by the Langmuir isotherm is defined as:

$$\int_{A_{ik}} \bar{J}_{ik}^{ad} . \bar{n} dS = \frac{A_{ik}}{A_k} \left[K_{det} \frac{s_k^t}{s_{k,max}} - \left(1 - \frac{s_k^t}{s_{k,max}}\right) K_{att} c_i \right] \times V_p \tag{3.19}$$

where s_k $(\mathrm{mol/m^3})$ is the solute concentration adsorbed on the surface of particle k, A_k is the overall surface of particle k, and V_p is the volume of particle k.

Finally, considering both sorption Equation (3.13) and Knudsen diffusion Equation (3.19), the evolution of each pore concentration is obtained by an explicit integration over time such as:

$$c_i^{t+\Delta t} = \sum_{i=1}^{4} \frac{V_p A_{ik}}{V_f A_k} \left[\left(1 - \frac{s_k^t}{s_{k,max}}\right) K_{att} c_i^t - K_{det} \frac{s_k^t}{s_{k,max}} \right] \Delta t^{\frac{ad}{des}} + \sum_{i=1}^{4} \frac{S_{ij}}{V_f L_{ij}} \ \frac{2r}{3} \sqrt{\frac{8\mathrm{RT}}{\pi M_g}} (c_j^t - c_i^t) \Delta t^K + c_i^t \tag{3.20}$$

with $\Delta t^{\frac{ad}{des}}$ and Δt^K the associated time steps.

3.2.2.2.Mass balance equation for particles

The amount of gas molecules adsorbed on the solid particles results from the transport of gas molecules both from neighboring solid particles and from pores (Figure 30b). Particle-particle flux occurs by surface diffusion, while pore-particle flux results from adsorption/desorption process. Let V_p be the volume of a particle *k*. Integrating the mass balance equation on particle *k* gives:

$$\int_{V_p} \frac{\partial s_k}{\partial \mathrm{t}} dV + \int_{V_p} \bar{\nabla} . \bar{\mathrm{J}}_{particle,k} \, dV \ = 0 \tag{3.21}$$

where s_k is the adsorbed concentration on particle k, and $\bar{J}_{particle,k}$ represents the gas fluxes coming in and out of particle *k*.

Applying the divergence theorem to Equation (3.21) gives:

$$\int_{V_p} \frac{\partial s_k}{\partial \mathrm{t}} dV + \int_{\partial V_p} \bar{\mathrm{J}}_{particle,k} . \bar{n} dS \ = 0 \tag{3.22}$$

Since each particle is connected to *N* particles (*N* depends on the spatial arrangement of the particles within the medium), and to 4 pores, the contour surface of each particle can be calculated as:

$$\partial V_p = \sum_{l=1}^{N} \partial V_{particle,k-particle,l} + \sum_{i=1}^{4} \partial V_{particle,k-pore,i} = \sum_{l=1}^{N} S_{kl} + \sum_{i=1}^{4} A_{ik} \tag{3.23}$$

where S_{kl} is the intersection surface area between particle k and particle l, and A_{ki} is the intersection surface area between particle k and pore *i* (Figure 30b).

Equation (3.22) can then be written as follows:

$$\int_{V_p}\frac{\partial s_k}{\partial t}dV = -\sum_{l=1}^{N}\int_{S_{kl}}\bar{J}_{kl}^{S}.\bar{n}dS - \sum_{i=1}^{4}\int_{A_{ki}}\bar{J}_{ki}^{ad}\bar{n}.dS \tag{3.24}$$

where $\bar{J}_{kl}^{S}$ is the surface diffusion flux between particle k and particle l, and $\bar{J}_{ki}^{ad}$ is the adsorption/desorption flux between particle k and pore i.

3.2.2.2.1.Surface diffusion

Particle-particle flux is governed by surface diffusion in which gas molecules are transported from the surface of a grain to the surface of a neighboring grain. In essence, molecules jump from an adsorption site to another adsorption site. The diffusive flux is thus driven by the gradient of sorbed concentration between and within particles and the surface diffusion flux can be expressed as:

$$\bar{J}^{s} = -D^{S}\bar{\nabla}s \tag{3.25}$$

The surface diffusion coefficient D^{S} is known to be a function of temperature following the Arrhenius equation and strongly depends on the surface loading (Do, 1998). For sake of simplicity, however, it will be kept constant hereafter.

The spatial integration of the diffusive flux between particles *k* and *l* is defined as:

$$\int_{S_{kl}}\bar{J}_{kl}^{S}.\bar{n}dS = -\,\theta\frac{D^{S}\,S_{kl}}{L_{kl}}(s_k^t - s_l^t\,) \tag{3.26}$$

where S_{kl} is the intersection surface area between particle k and particle l computed here as $S_{kl} = 4r_l r_k$, L_{kl} is the distance between the centers of particle k and particle l, r_l and r_k are the radiuses of particle k and particle l , and θ is a scaling parameter enabling to constrain the transport properties of the simulated medium depending on the structural characteristics of the particle assembly (θ is related to the particle connectivity which is a function of the particle size distribution of the packing as well of its porosity).

3.2.2.2.2.Sorption

Particle-pore diffusion processes are governed by the same mechanisms than pore-particle diffusion processes (see Equation (3.19)).

Finally, combining both sorption Equation (3.19) and surface diffusion Equation (3.26), the evolution of each particle concentration is obtained by an explicit integration over time such as:

$$s_k^{t+\Delta t} = \sum_{i=1}^{4}\frac{A_{ik}}{A_k}\left[\left(1-\frac{s_k^t}{s_{k,max}}\right)K_{att}c_i^t - K_{det}\frac{s_k^t}{s_{k,max}}\right]\Delta t^{\frac{ad}{des}} + \sum_{l=1}^{m}\theta\frac{D^{S}\,S_{kl}}{V_p\,L_{kl}}(s_k^t - s_l^t\,)\Delta t^{sd} + s_k^t \tag{3.27}$$

with $\Delta t^{\frac{ad}{des}}$ and Δt^{sd} the associated time steps.

3.2.3.Hydro-mechanical coupling

The hydraulic forces acting on a solid particle immersed in a fluid result from both the pressure and viscous stress acting on its surface (Chareyre et al., 2012). In coal matrix with nanometer pores, pore velocities are very low (they are actually neglected in the mass transport model) and hence are the viscous stress forces. We thus only consider the contribution of the normal pressure forces which result from pressure losses within the pore space as follows:

$$\overrightarrow{F_{ij}^{k}} = A_{ij}^{k}(p_i - p_j)\overrightarrow{n_{ij}} \tag{3.28}$$

where $p_i - p_j$ represents the pressure difference between pore i and pore j, A_{ij}^{k} is the intersection surface area between particle k and the pore throat between pore i and pore j, $\overrightarrow{n_{ij}}$ is the unit vector pointing from pore i to pore j. As shown in (Catalano et al., 2014) and in (Scholtès et al., 2015), the HM coupling resulting from Equation (3.28) enables the DEM-PFV model to simulate conventional poromechanical behaviors as described by Biot's theory (Biot, 1941).

The classical Biot's theory states that the mechanical behavior of a porous medium depends on the bulk fluid pressure only (p_f) without considering its detailed composition. This means that two pore fluids with different compositions having the same bulk pressure should produce the same volumetric deformation. This is not verified for swelling materials like coal which shows different deformation amplitudes depending on the nature of the pore fluid (Ottiger et al., 2008). It is now well known that the deformation of coal is not solely governed by the pore bulk pressure: as for all swelling materials, sorption processes induce additional deformation related to the nature of the sorbed molecules (Brochard et al., 2012). Gas molecules get adsorbed at the surface of the pores and induces a surface excess free energy. An additional interfacial force is thus exerted and resulting stress develops within the porous medium. Different approaches were proposed to introduce these nanoscale features into an extended poromechanical equation to explain the sorption-induced deformations from a continuum description. First works have introduced the so-called solvation pressure to describe swelling since in confined pores(Gor and Neimark, 2010; Kowalczyk et al., 2008; Ustinov and Do, 2006; Yang et al., 2010). A second class of models, based on an energy balance approach, relates the changes in surface potential energy due to gas adsorption to the elastic energy (Dolino et al., 1996; Grosman and Ortega, 2008; Pan and Connell, 2007). Other researchers also have reformulated the poroelastic constitutive equations by introducing an apparent porosity and an interaction free energy that are both related to the Gibbs adsorption isotherm (Mushrif and Rey, 2009; Perrier et al., 2018; Pijaudier-Cabot et al., 2011; Sampath et al., 2020; Vermorel and Pijaudier-Cabot, 2014). In contrast, (Brochard et al., 2012; Espinoza et al., 2014, 2013; Nikoosokhan et al., 2014; Vandamme et al., 2010) have made use of the bulk pressure and of the swelling strain to express the sorbed amount or the adsorption-induced pressure.

In the present work, the sorption-induced deformations are interpreted in terms of the solvation pressure or adsorption pressure p_s, that is related to the amount of gas molecules attached to the solid skeleton. Specifically, the total pore pressure in each pore i is equal to the sum of the bulk fluid pressure p_f and of the solvation pressure p_s such as:

$$p_i = p_{i,f} + p_{i,s} \tag{3.29}$$

with $p_{i,f}$ and $p_{i,s}$ defined as follows:

$$p_{i,s} = \sum_{k=1}^{4} \frac{A_{i,k} \times p_s^k}{A_{i,k}} \tag{3.30}$$

$$p_{i,f} = c_i RT \tag{3.31}$$

where the solvation pressure related to the amount of gas molecules attached to the particle k is denoted p_s^k and computed as

$$p_s^k = \alpha s_k RT \tag{3.32}$$

A_{ik} is the intersection surface area between particle k and pore i, and α is a coupling coefficient. Hereafter, α is fixed constant but it is not necessarily the case (Brochard et al., 2012).

Although the solvation pressure is dependent of the adsorbed amount on a grain and hence should be specific to a given particle, it is also a pressure which is summed up with the bulk pressure specific to a pore. To further explain how this additional pressure term is calculated within the pore space, we illustrate in Figure 31 the different situations that can be encountered:

- Case 1: for connected pores (belonging to the connected porosity which will be further discussed in Section 3.3), we compute a contact surface weighted average solvation pressure for each particle in contact with pore i, and the fluid pressure value depends on the gas pressure gradient within the percolating pore space.
- Case 2: for isolated pores (belonging to the unconnected porosity), the fluid pressure and the solvation pressure are fixed to zero resulting in a zero-total pore pressure. These pores also have no contribution on the fluxes related to the surrounding pores and particles.

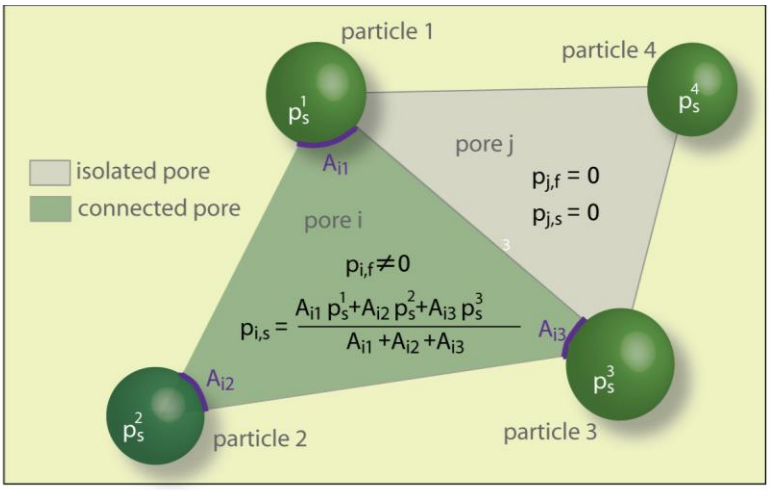

Figure 31 2D representation of pore pressure distribution within the pores of the DEM-PFV model: distinction between activated vs inactivated pores

3.3.Model implementation

3.3.1.Scaling strategy

If the interparticle properties presented in Section 3.2.1 can be calibrated so that the emergent mechanical properties of the DEM model match those of the material to model (see (Scholtès and Donzé, 2013) for details of the procedure), the diffusion mechanisms at stake require some adjustments of the transport model. For instance, coal matrix has a porosity that is significantly smaller than the porosity of an assembly of spherical particles. Basically, the pore space of the model is scaled so that the effective volume of fluid $V_{f,eff}$ is equal to:

$$V_{f,eff} = V_f \frac{n_m}{n_a} \tag{3.33}$$

with n_a the porosity of the spherical particle assembly, and n_m the porosity of the actual material.

Scaling the diffusive fluxes is actually sufficient to match the required porosity without changing the volume of both the pore space and the solid phase in the discretized equations, resulting in a total mass balance that accurately represents the material to model as follows:

For particles:
$$\bar{J}_{eff} = \bar{J}\frac{1-n_a}{1-n_m} \tag{3.34}$$

For cells:
$$\bar{J}_{eff} = \bar{J}\frac{n_a}{n_m} \tag{3.35}$$

with $\bar{J}$ the non-scaled flux calculated according to the previous sections and $\bar{J}_{eff}$ the effective ("scaled") diffusive flux.

In addition, we also introduced a procedure to adjust the poromechanical response of our DEM-PFV model since the Biot coefficient of a DEM assembly is intrinsically equal to 1 given the rigid particle assumption of the DEM formulation. As a matter of fact, according to the poroelasticity theory (Detournay and Cheng, 1993), the contribution of the pore pressure *p* to the overall deformation of porous media is defined through the effective stress such as

$$\sigma' = \sigma - bp \tag{3.36}$$

where σ' is the effective stress, σ is the total stress, and *b* is the Biot coefficient equal to $1 - \frac{K}{K_s}$ with K the bulk modulus of the medium, and K_s the bulk modulus of the solid phase. This effective stress produces volumetric strain ε_v which, for a swelling material, presents an additional term of adsorption induced strain ε_s as follows:

$$\varepsilon_v = -\frac{1}{K}\left(\sigma - bp_f\right) + \varepsilon_s \tag{3.37}$$

where $\sigma = \frac{\sigma_{kk}}{3}$ is the mean stress and ε_s is defined such as:

$$\varepsilon_s = b\frac{p_s}{K} \tag{3.38}$$

Instead of applying a global scaling factor to Equation (3.29), we introduced the possibility to neutralize a certain amount of pores within the pore network so that the connected porosity of the particle assembly $n_{a,c}$ is equal to:

$$n_{a,c} = bn_a \tag{3.39}$$

with *b* directly equal to the Biot coefficient of the material. The neutralized pores (unconnected porosity) correspond to tetrahedra randomly chosen within the triangulated mesh where gas transport calculations are simply not performed. These isolated pores thus participate to the overall deformability of the particle assembly due to their compliance without contributing to its poromechanical response as

illustrated in Figure 32.

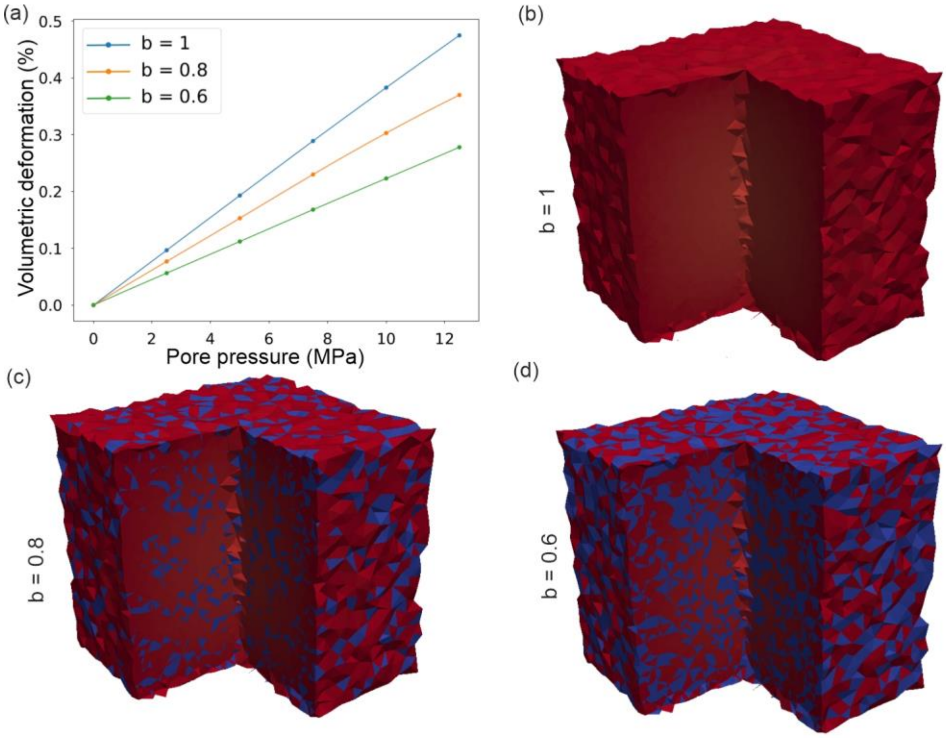

Figure 32 Illustration of the connected porosity $n_{a,c}$ and of its effect on the Biot coefficient, Equation (3.39): a) Volumetric deformation as a function of pore pressure increase and b,c,d) pressure distribution at equilibrium (p_{CO2}=12.5 MPa) in numerical samples with different pre-defined Biot coefficients (the connected pores are in red and the isolated pores in blue).

3.3.2.Time scaling

Time scaling is a critical aspect in gas injection experiments conducted on coal samples, often requiring a minimum duration of 10 days. However, aligning the real-time duration with the duration of numerical simulations poses a challenge. To address this, a strategic approach is adopted, wherein time is scaled to optimize the computational time.

The time step in our HM simulations depends on the mechanical properties and the diffusion coefficients. Employing the FTCS method, we select the minimum time step based on these parameters and proceed with the simulation. Typically, simulation time steps range from 10^{-5} to 10^{-7} s to ensure numerical stability when aligning with experimental data. This implies that completing 5,000 iterations leads to 0.0005 s in real-time which translates to around 5 to 6 h of simulation duration on a workstation for numerical samples with thousands of particles as presented in the present work. This is problematic with regards to the duration of a Ph.D. thesis.

To mitigate this, time scaling between numerical simulations and experimental setups becomes imperative. Considering that the mechanical time step is not a limitation thanks to the use of density scaling (the mechanical time step is a function of the mass which can be increased without any consequences if gravity does not apply in the simulations), and given that fluxes are functions of both time step (Δt) and diffusion coefficients, adjusting the time step by a certain factor necessitates a reciprocal adjustment in the diffusion coefficients (i.e., increasing the time step by a factor X and adjusting the diffusion coefficients par a factor 1/X provides the same result). This ensures the synchronization of numerical time steps with experimental conditions, optimizing the efficiency of the simulation process.

3.3.3.Numerical stability

Numerical stability needs to be considered in every explicit numerical scheme as any effect can only move by a maximum of one spatial grid block in one time step. For instance, in the general case of a 2D diffusion problem, the explicit discretization reads:

$$\frac{u_i^{t+\Delta t}-u_i^t}{\Delta t} = D\,\frac{u_{i+1}^t-2u_i^t+u_{i-1}^t}{\Delta x^2} \tag{3.40}$$

where D is the diffusion coefficient. Solving Equation (3.40) for $u_i^{t+\Delta t}$ leads to:

$$u_i^{t+\Delta t} = ru_{i+1}^t + (1-2r)u_i^t + ru_{i-1}^t \tag{3.41}$$

with $r = D\frac{\Delta t}{\Delta x^2}$ the Fourier Number. Applying the Von Neumann stability analysis, the FTCS (Forward Time Centered Space) method is satisfied only if the following condition is fulfilled:

$$r \leq \frac{1}{2} \text{ then } \Delta t \ \leq \frac{\Delta x^2}{2D} \tag{3.42}$$

In our model, in addition to the mechanical time step that governs the solid particles motion, three-time steps exist due to the three different types of transport mechanisms occurring respectively between pore-pore, pore-particle and particle-particle. The diffusion coefficient D in Equation 3.42 is therefore respectively equal to the surface and Knudsen diffusion coefficients $D = (D^s, D^K)$. Then, to ensure the stability of the numerical scheme, the simulation time step Δt is set up equal to a fraction of the minimum time step $\Delta t_{min} = \min\left(\Delta t^m, \Delta t^K, \Delta t^{\frac{ad}{des}}, \Delta t^s\right)$ required to ensure the stability of the numerical scheme (in all our simulations, the time step was defined equal to 0.8 Δt_{min}).

3.4.Verification of the transport models

To verify the correct implementation of the transport equations in our DEM-PFV model, we compared its predictions to analytical solutions of Fick's law considering different 1D problems. For that purpose, we built up a pseudo 1D numerical assembly with dimensions equal to L_0 x 0.2L_0 x 0.2L_0 m, made up of 1,000 particles with radii varying between 7.1 and 13 mm, and 5,500 cells. In all the verification examples presented below, HM couplings were not considered, and the simulated medium was non deformable (the mechanical scheme was turned off and the particles fixed in space and time). In the present section and for the sake of comparison, all results and variables will be presented dimensionless. The *x*-coordinate, the Knudsen diffusion coefficient D^K, and the concentration *c* are normalized respectively by the sample length L_0, the gas diffusion coefficient D_0, and the inlet concentration c_0. The dimensionless time is defined as $t = Dt_0/L^2$ where t_0 is the physical time. Similar normalization holds for the sorbed concentration *s* and the surface diffusion coefficient D^s. The different test cases are gathered in Table 3. together with the parameter values used in the simulations and the corresponding analytical solutions.

Table 3.

Numerical parameters of the different verification test cases.

Parameter	Test case 1	Test case 2	Test case 3
n	0.45	0.47	0.45
Dimensionless time step Δt	9e-7	9e-6	9e-7
D^K / D_0	1	-	1
D^S / D_0	-	1	-
θ	-	1.12	-
$K_d = k_{att}/k_{det}$	-	-	2
k_{att}	-	-	0.116
k_{det}	-	-	0.058

3.4.1.Test case 1: Knudsen diffusion

First, we consider diffusion of non-sorbing species within a nanoporous material. As a consequence, only Knudsen diffusion occurs, and both sorption and surface diffusion may be neglected. The boundary value problem is thus defined by the following initial and boundary conditions:

$$\frac{\partial c}{\partial t} = D^K \frac{\delta^2 c}{\partial x^2}, \quad \forall x \in [0, L_0] \tag{3.43}$$

$$c(x, 0) = c_0, \quad \forall x \in [0, L_0]$$
$$c(0, t) = c(L_0, t) = 0$$

Using Fourier series, the unsteady solution of this 1D diffusion problem can be written as follows:

$$c(x, t) = \sum_{m=1}^{\infty} \frac{2}{\pi} \left(\frac{1 - cos(m\pi)}{m}\right) sin\left(m\pi \frac{x}{L_0}\right) e^{-\frac{D^K}{n_a L_0^2}(m\pi)^2 t_0} \tag{3.44}$$

The numerical assembly, illustrated in Figure 33a, was subjected to the initial and boundary conditions defined in Equation (3.43), and the simulation was run with the parameters presented in Table 3.

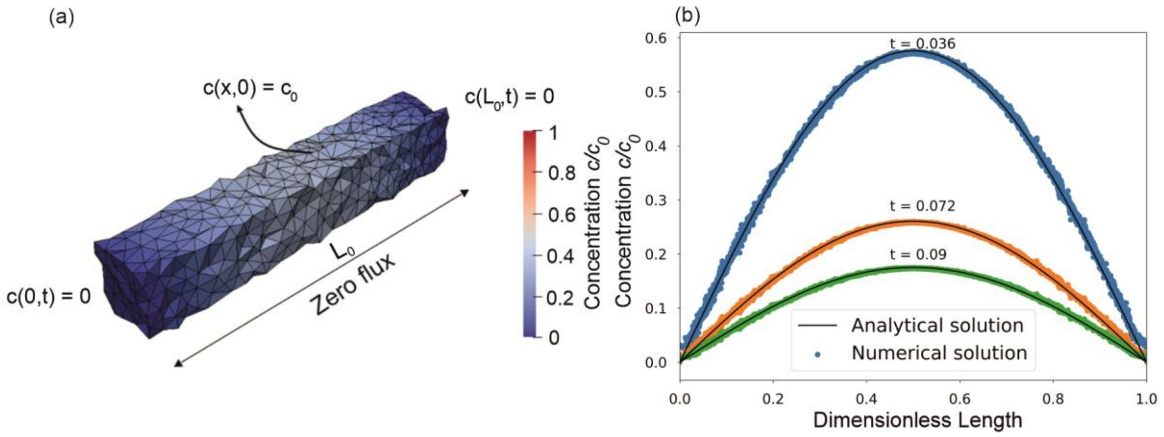

Figure 33 a) Concentration distribution in pores at t=0.04. b) Numerical and analytical concentration profiles in pores at different times.

As shown in Figure 33b, the concentration distribution in the numerical model matches perfectly the analytical solution in space and time, confirming the accuracy of the numerical scheme for simulating Knudsen diffusion.

3.4.2.Test case 2: surface diffusion

The second test case assumes that the gas molecules are irreversibly adsorbed and may only diffuse through the solid grains. Surface diffusion is thus considered as the only effective transport mechanism and the problem is defined by the following initial and boundary conditions:

$$\begin{gathered}\frac{\partial s}{\partial t} = D^S \frac{\delta^2 s}{\partial x^2}, \quad \forall x \in [0, L_0] \\ s(x,0) = s_0, \quad \forall x \in [0, L_0] \\ s(0,t) = s(L_0,t) = 0\end{gathered} \tag{3.45}$$

This 1D diffusion problem is very similar to the first one and the analytical solution in terms of Fourier series can be written as follows:

$$s(x,t) = \sum_{m=1}^{\infty} \frac{2}{\pi}\left(\frac{1-cos(m\pi)}{m}\right) sin\left(m\pi \frac{x}{L_0}\right) e^{-\left(\frac{D^S}{(1-n_a)L_0^2}\right)(m\pi)^2 t_0} \tag{3.46}$$

The numerical values used in the simulation are presented in Table 3. The parameter θ was initially calibrated since the number of contacts between particles depends on the packing characteristics (samples are generated using a random packing procedure, considering a pre-defined size distribution). Figure 34a displays an example of the concentration field in the solid grains at a given time of the simulation, while a comparison of the numerical solutions with averaged concentration profiles at different times is provided in Figure 34b. As for test case 1, the concentration distribution in the numerical model matches perfectly the analytical solution in space and time, showing the correctness and reliability of our surface diffusion model and of its implementation.

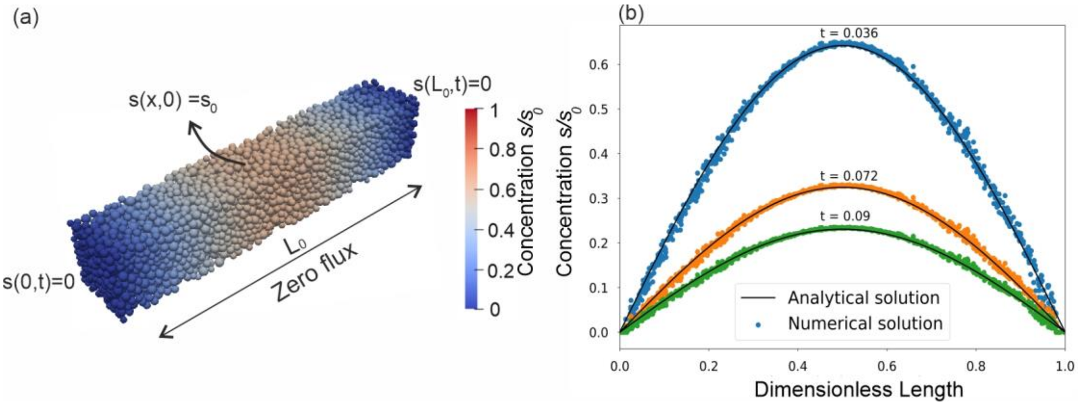

Figure 34 Concentration distribution in particles at t = 0.04. b) Comparison of numerical and analytical concentration profiles in particles at different times.

3.4.3.Test case 3: Knudsen diffusion with adsorption/desorption

For this test case, we consider diffusion of a sorbing species within a non-swelling porous material. Here, we used a linear isotherm to describe the solute adsorption onto the solid grains (see Section 3.2.2.1.2) and surface diffusion is neglected (no transport within the solid phase). The system is initially at thermodynamic equilibrium so that partitioning between gas and solid phases is respected. The adsorption and desorption kinetics coefficients K_{att} and K_{det} are chosen high enough so that the equilibrium state is verified at each time step. Based on these assumptions, the 1D boundary value problem is defined as follows:

$$\begin{gathered}\frac{\partial c}{\partial t} = D^K \frac{\delta^2 c}{\partial x^2}, \quad \forall x \in [0, L_0] \\ s(x,t) = K_d\, c(x,t), \quad \forall x \in [0, L_0] \\ c(x,0) = c_0\, ; s(x,0) = K_d c_0, \quad \forall x \in [0, L_0] \\ c(0,t) = c(L_0,t) = \ 0\end{gathered} \tag{3.47}$$

and the transient analytical solution is given by:

$$c(x,t) = \sum_{m=1}^{\infty} \frac{2}{\pi} \left(\frac{1-cos(m\pi)}{m}\right) sin\left(m\pi \frac{x}{L}\right) e^{-\left(\frac{D^K}{n_a(1+K_d)L_0^2}\right)(m\pi)^2 t_0} \tag{3.48}$$

The numerical parameters used for this test case are presented in Table 3. Figure 35a displays an example of the concentration fields in both pores and grains obtained at a given time while a comparison of the numerical solutions with averaged concentration profiles at different times is provided in Figure 35b. Here again, a very good agreement between the numerical and analytical solutions is obtained. We may also observe that our kinetics formulation converges well to the equilibrium since the partitioning between gas and solid grains, driven by $K_d = 2$, is always respected. This comparison validates the coupling method between diffusion and sorption processes.

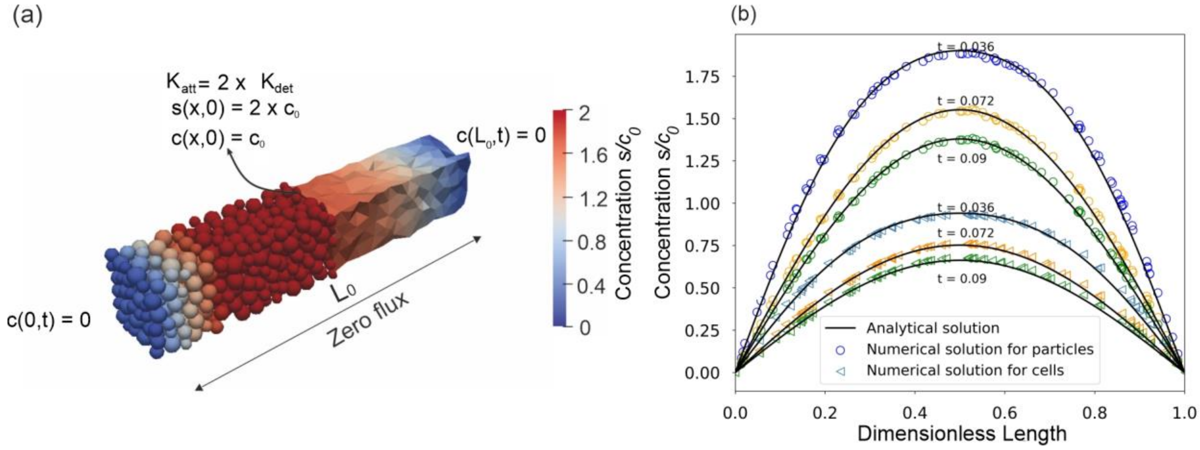

Figure 35. a) Concentration distribution in particles and pores simulated numerically at *t* = 0.04. b) Comparison of numerical and analytical concentration profiles in pores and particles at different times.

3.5.Hydro-mechanical behavior: comparison with a swelling experiment

To verify the implementation and validity of our HM scheme (Section 3.2.3), we compared the predictions of our model to the experimental results of Day et al. (Day et al., 2008a) who performed a swelling experiment on a 30 x 10 x 10 mm block of coal under confined conditions. The CO_2-induced coal swelling was measured for different values of CO_2 pressure by optical method. The experiment performed at 55°C on the Australian bituminous coal from the Bowen Basin (referred to as sample 3 in Day et al. (Day et al., 2008a) and as Qld8 in Day et al. (Day et al., 2008b)) was used as reference. Note that the same data set (but at 40°C) was also used by (Sampath et al., 2020) for model validation purpose but some discrepancies exist between our two investigations. Indeed, due to the lack of experimental data available, a part of their numerical properties were obtained from another coal experiment and they discarded the highest pressures of swelling experiment (higher than 12MPa) for comparison. In the present analysis, we did our best to carry out a fair comparison by using the full range of experimental data available and a complete set of consistent physical properties for this coal. All the parameter values are gathered in Table 4. Because the elastic properties and Biot coefficient were not provided either in (Day et al., 2008b, 2008a), we set the value of *b* based on the value used by Sampath et al. (Sampath et al., 2020). The Young modulus E and the Poisson ratio υ were chosen in order to reproduce the behavior observed by Day et al. (Day et al., 2008a) with a non-sorbing gas (a volumetric contraction of 0.06% was reached at 15MPa of helium pressure). The s_{max} value was inferred from the maximum sorption capacity of the coal W_0 in the isotherm model calculated by Day et al. (Day et al., 2008b) (68.4 kg of CO_2 per ton of rock for the sample Qld 8). Finally, values of D^K and D^S were taken from the literature (Dong et al., 2017) whereas K_{att} , K_{det} were fixed arbitrarily. D^S is fixed constant but D^K varies as a function of the pore radius, as expressed in Equation (3.12), around an average value found in the literature (see Table 4). Note that the values chosen for these transport and kinetic parameters do not affect the steady-state behavior and hence, the comparison we made which is based on equilibrium states.

3.5.1.Sample preparation

A 10 x 10 x 10 mm particle assembly made up of 10,000 particles was generated and the interparticle properties calibrated following the approach proposed by (Scholtès and Donzé, 2013). The coal sample is considered isotropic although, even for the matrix, this assumption may be questioned (Day et al., 2008a). The calibration was done by performing uniaxial compression tests on the numerical sample following a trial and errors approach to determine the adequate interparticle properties to match both Young modulus and Poisson ratio of the coal. In addition, both the porosity and Biot coefficient of the numerical sample were defined to match those of the tested coal by following the procedures presented in Section 3.3.1.

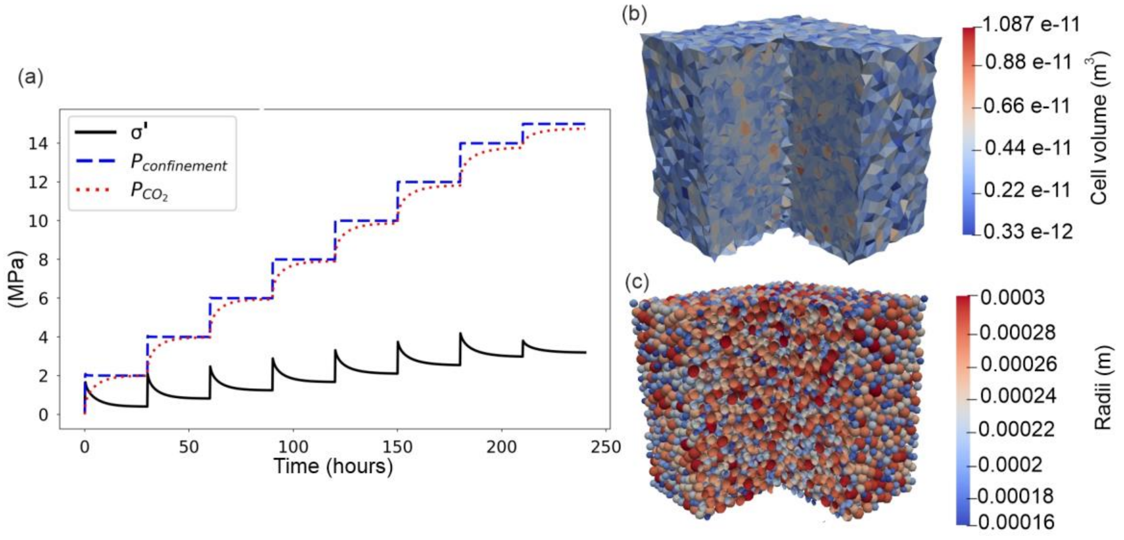

Figure 36 Numerical set up for simulating the swelling experiment of Day et al. (2008): a) boundary pressures and resulting mean effective stress, b) pore size distribution, c) particles size distribution.

Table 4

Numerical parameters used to simulate the coal matrix experiment by Day et al. [57]. The star symbol denotes the calibration parameters.

Parameters	DEM-PFV model	Sources
Young modulus E (GPa) *	4.550	*computed from Day et al., 2008* (Day et al., 2008a) *(sample 3)*
Poisson ratio υ (-)*	0.225	*computed from Day et al., 2008* (Day et al., 2008a) *(sample 3)*
Temperature T (K)	328	*Day et al., 2008* (Day et al., 2008a) *(sample 3)*
Gas constant R ($J.mol^{-1}.K^{-1}$)	8.314	*N/A*
Molar mass M_g ($g.mol^{-1}$)	44.01	*N/A*
Skeletal density ($kg.m^{-3}$)	1303	*Day et al., 2008* (Day et al., 2008b) *(sample Qld 8, Table 3)*

s_{max} (mol.m^{-3})	2025	*Day et al., 2008* (Day et al., 2008b) *(sample Qld 8, Table 2)*
K_d (mol.m^{-3}) *	0.0017	-
K_{att} (s^{-1})	17e-11	-
K_{det} (mol.m^{-3}. s^{-1})	1e-7	-
D^K(×10^{-12} m^2.s^{-1})	3	*Dong et al., 2017* (Dong et al., 2017) *(Table 4)*
D^s(×10^{-12} m^2.s^{-1})	30	*Dong et al., 2017* (Dong et al., 2017) *(Table 4)*
Biot coefficient *b* (-)	0.8	*Sampath et al., 2020* (Sampath et al., 2020) *(Table 2)*
Coupling coefficient α (-) *	20.2	-
Porosity of assembly n_a (%)	32	*N/A*
Porosity of coal sample n_m (%)	7.1	*Day et al., 2008* (Day et al., 2008b) *(sample Qld 8, Table 3)*

3.5.2.Experimental procedure

Day et al. (Day et al., 2008a) measured the dimensional changes of a sample contained within a pressure cell where CO_2 pressure was increased up to 15 MPa. In our experiment, the numerical sample is confined in between 6 frictionless boundary walls to control the confining pressure $p_{confinement}$. To reproduce the swelling experiment of Day et al. (Day et al., 2008a), we imposed CO_2 pressure both as boundary stress ($p_{confinement}$) and as boundary pressure (p_{CO2}) on all the sample boundaries. $p_{confinement}$ is adjusted by displacing the boundary walls. During the simulation, p_{CO2} and $p_{confinement}$ were increased stepwise from equilibrium states and the volumetric deformation ε_v, solvation pressure (p_s), adsorbed amount of gas (s), and fluid pressure (p_f) were recorded at each step (Figure 36a).

Since the Biot coefficient is lower than one, the effective stress varies at each CO_2 injection pressure step. Day et al. (Day et al., 2008a) however suggest that the mechanical compression caused by the pore pressure increase can be neglected (0.06% of contraction for non-sorbing gas against 2% of swelling deformation with CO_2 at 15Mpa). In other words, Day et al. investigated throughout this experiment the influence of sorption-induced swelling on the poromechanical behavior of the material without taking into consideration the effect of the fluid bulk pressure.

3.5.3.Parametric study

Before directly comparing the model results with the experimental observations, a parametric study is presented to highlight the influence of the model parameters on the emergent behavior. The results are summarized in Figure 37 and the parameters roles assessed as follows:

- The coupling term α controls the intensity of the solvation pressure p_s (Equation (3.32)), Figure 37b), hence the amplitude of the associated deformation (Equation (3.37)), Figure 37c). Thus, α needs to be adjusted as a function of the swelling potential of the material with respect to the nature of the adsorbed fluid as, for example, CO2 induces larger swelling than CH_4 in coal (Durucan et al., 2009). p_s is directly proportional to α (Figure 37b), giving the opportunity to set its value so as to match experimental evidence of swelling for each combination of material and adsorbed fluid. One has to note that α does not influence the amount of molecules that can be adsorbed on the solid phase (Figure 37a).

- According to Equations (3.17) and (3.18), s_{max} determines the maximum amount of gas molecules that can be adsorbed on the surfaces of the solid phase. Depending on the nature of the fluid-solid interaction at play, s_{max} must be adjusted because it also affects the solvation pressure and thus the volumetric deformation (Figure 37d-e-f). In contrast, K_d controls the adsorption/desorption kinetics (Figure 37g-h-i) without influencing the maximum amount of adsorbed gas molecules, hence leading to the same plateau value for the adsorbed amount of gas molecules, solvation pressure and volumetric deformation.
- Finally, the Biot coefficient b does not influence neither the amount of adsorbed gas molecules nor the solvation pressure (Figure 37j-k) while it directly influences the volumetric deformation (Figure 37l), as described by the poromechanical equation (Equation (3.37)).

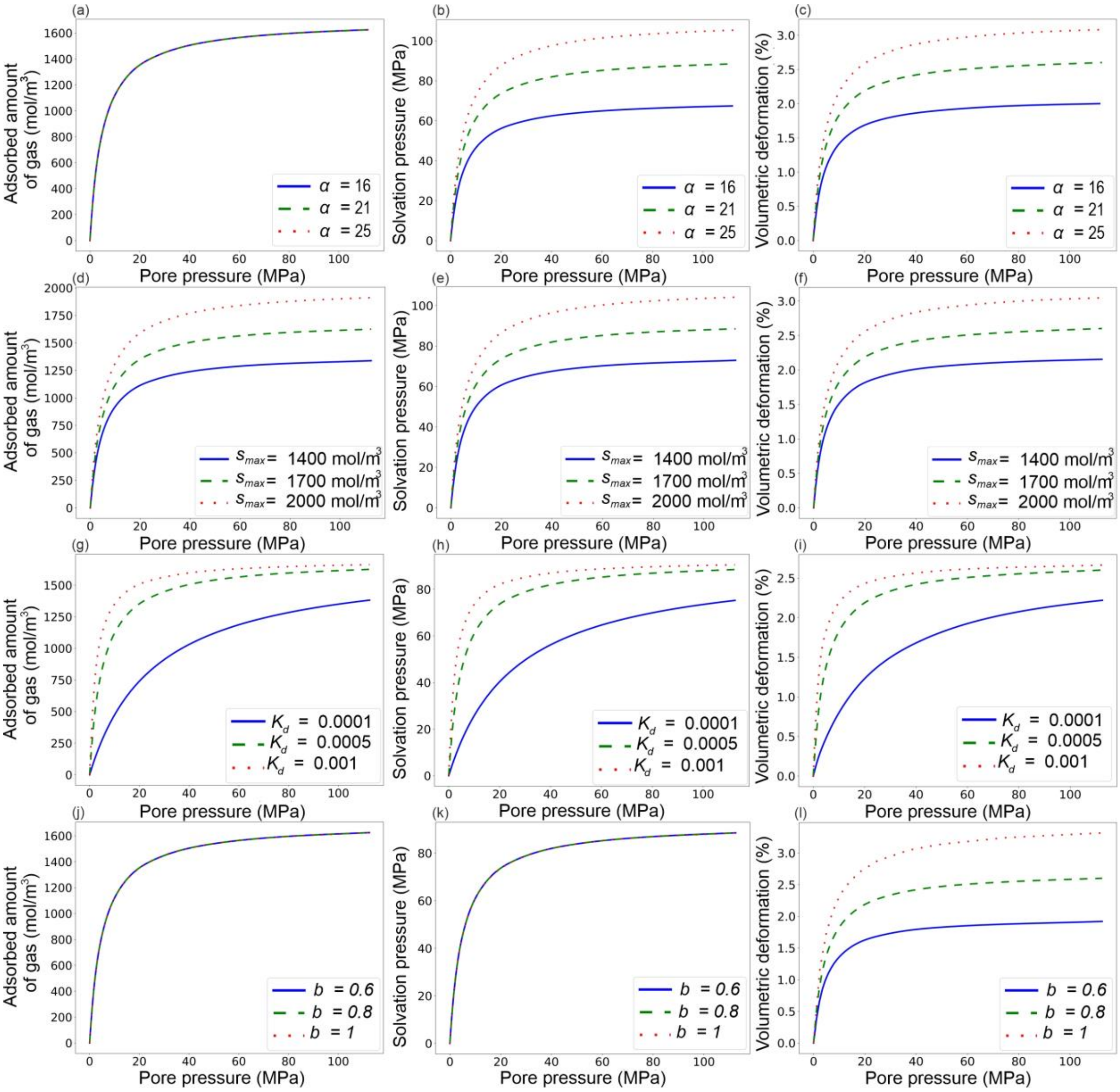

Figure 37 Evolution of adsorbed amount of gas s (left), solvation pressure p_s (middle) and volumetric deformation ε_v (right) versus pore pressure p_f for: (a,b,c) different α values and fixed parameters (s_{max}=1700, K_d=0.0005, b=0.8), (d,e,f) different s_{max} values and fixed parameters (α =21, K_d=0.0005, b=0.8), (g,h,i) different K_d values and fixed parameters (α =21, s_{max}=1700, b=0.8), (j.k,l) different b values and fixed parameters (α =21, K_d=0.0005, s_{max}=1700).

3.5.4. Calibration procedure and comparison to the experiment of Day et al.

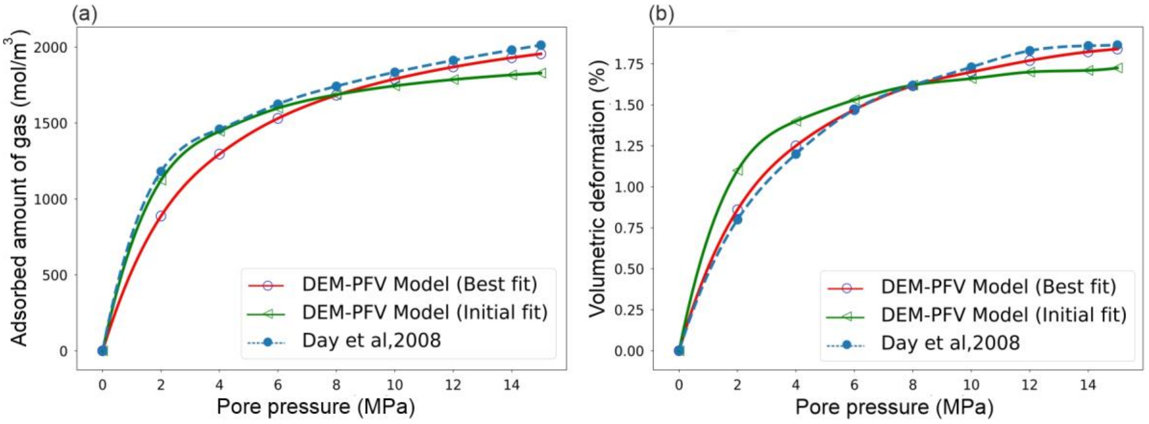

Figure 38 Swelling experiment: comparison of the DEM-PFV model predictions to the experiment of Day et al. (Day et al., 2008a): evolutions of a) adsorbed amount of gas and, b) volumetric deformation as functions of the pore pressure.

The calibration of the model was done through the following procedure:

1. Determine the interparticle elastic properties (E_{eq} and P) through uniaxial or triaxial compression testing (trial and error adjustments) to match both Young modulus E and Poisson ratio υ of the material.
2. Set b equal to the measured value and scale the numerical sample connected porosity $n_{a,c}$.
3. Determine the experimental solvation pressure p_S by using the extended poromechanical equations, (Equations (3.37) and (3.38)) such that

$$p_S = \frac{K\,\varepsilon_v + (\sigma - b p_f)}{b} \tag{3.49}$$

   where $K = \frac{E}{3(1-2\vartheta)}$ is the bulk modulus and $\sigma = \frac{\sigma_{kk}}{3}$ is the mean stress and, from the value of s_{max}, estimate α using the plateau value of p_S.

4. Finally, calibrate K_d (trial and error adjustments) so that the numerical results fit with the experiments in terms of solvation pressure or swelling deformation.

The numerical results presented in Figure 38 (referred to as the initial fit) match the experimental observations for the following set of parameters: $\alpha = 20.02$, $K_d = 0.0017$ mol.m^{-3} with the s_{max} value inferred from the experiment ($s_{max} = 2025$ mol.m^{-3}). The fit to experimental data point is not ideal yet. In their study, Day et al. (Day et al., 2008b) have explored a pore filling isotherm model (Dubinin–Radushkevich model) which has been found to provide a better fit to experimental adsorption data than the classical Langmuir model, especially at high pressures, above 6 MPa. A comparison between this isotherm model and ours is shown in Figure 38a and confirms this observation. This discrepancy, inherent to the use of Langmuir isotherm, is also observed when comparing volumetric deformations in Figure 38b (an average error of 19% is found). Note that a better fit can be achieved when fitting also the s_{max} value. A second simulation, referred to as the best fit, where $s_{max} = 2400$ mol.m^{-3}, $K_d = 0.0008$ mol.m^{-3} and $\alpha = 20.02$ is shown in Figure 38a and Figure 38b. The error is thus reduced to 2% for volumetric deformation.

Additional insights can be gained from numerical simulations into the dynamics of mass transfer processes within the coal material. Figure 39 shows the changes in averaged gas and sorbed concentrations with time in the porous sample between two successive constant pressure steps. The corresponding porosity variation is also exhibited. As an illustrative example, we focused on the transient behavior corresponding to an increase from 0 to 15 MPa of CO_2 pressure. Results indicate that the gas diffuses first through the solid phase. As expected from diffusion values of Table 4 and accordingly to the literature (Dong et al., 2017; Mathias et al., 2020), surface diffusion is the predominant transport mechanism within coal matrix. This increase in sorbed concentration within the coal sample results in swelling and hence, volumetric strain and porosity increase. Owing to the values used for K_{att} and K_{det}, the desorption rate is not large enough and equilibrium is reached faster in the solid phase than in the gas phase (Figure 39). As a consequence, swelling occurs before the pore pressure reaches its equilibrium state in agreement with Sampath et al. results (Sampath et al., 2020).

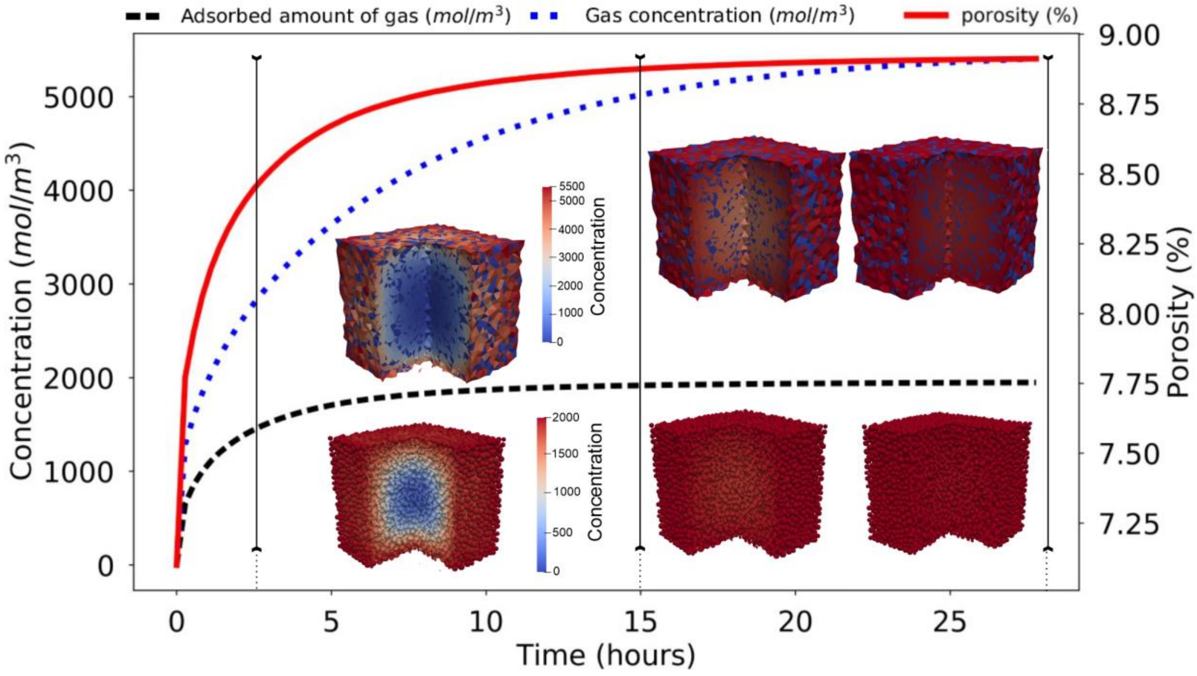

Figure 39. Evolution of porosity, fluid concentration and adsorbed amount of gas with time.

3.6.Conclusion

A new 3D pore-scale model for porous swelling materials is proposed to the hydromechanical behavior of coal subjected to gas transport. In our model, a DEM model where the material is represented as an assembly of particles interacting one with another according to predefined contact laws is coupled to a PNM approach for describing transport mechanisms between and within pores and solid grains. The material is assumed to be saturated with gas and various mechanisms for gas transport across the coal matrix have been considered including Knudsen diffusion, surface diffusion and sorption. Mechanical couplings inherent to such swelling materials are also taken into account. The model simulates both (i) the interplay between pore pressure and external stress with variations in the effective stress which may impact the mechanical behavior of the medium and (ii) the sorption processes which contribute to swell or shrink the material. This latter mechanism is considered through the addition of an additional pressure term, classically called the solvation pressure, related to the sorbed concentration.

The implementation of the model was tested against analytical solutions and compared to a swelling experiment. The model was found to be robust and a suitable tool for describing adsorption induced deformation. This comprehensive investigation reveals the complex physics at stake during methane adsorption and the numerical results give precious insights onto the internal dynamics of gas within the coal matrix. In particular, simulations reveal that coal matrix swelling occurs before the pore pressure reaches its equilibrium state since surface diffusion prevails. The present model is thus capable to describe the strong coupling between transport, chemical (sorption) and mechanical processes and can be used to predict methane recovery. Future work will focus on introducing cleat network to assess the effect of cleat intensity and facilitate more comprehensive analysis on the permeability changes at the coal rock mass scale.

3.7.Supplementary material: Mass balance validation

Validation of a model is a crucial step in ensuring its accuracy and reliability. In the case of gas molecule transport, one important factor to consider is the conservation of mass. To achieve this, we simulate a closed system that is not initially at equilibrium with the parameters presented in Table 5.

Table 5

numerical parameters of the DEM-PFV model used for mass balance validation

Parameter	Test case 1
time step Δt	1e-6
D^K	1e-1
D^{sd}	1e-5
$\propto$	0 to 140
$K_d = k_{att}/k_{det}$	1e-1
k_{att}	25e-2
k_{det}	25-1
Temperature T (K)	328
Gas constant R (J.mol^{-1}.K^{-1})	8.314
Molar mass M_g (g.mol^{-1})	44.01
s_{max} (mol.m^{-3})	1000
Young modulus E (GPa) *	4.550
Poisson ratio υ (-)*	0.225
Bulk density (kg.m^{-3})	1220

Skeletal density (kg.m^{-3})	1303
Biot coefficient *b* (-)	1

The boundary value problem is defined by the initial and boundary conditions presented in Figure 40.

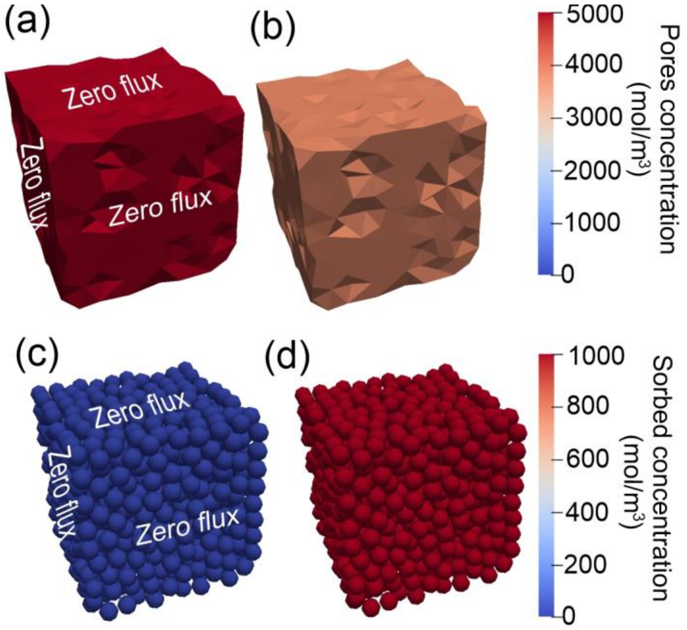

Figure 40. Mass balance verification test case: a) pore concentration at t = 0 b) pore concentration at t=inf c) particle concentration at t = 0 d) particle concentration at t = inf.

The goal here is to monitor the behavior of the system over time and to assess the conservation of mass during gas transport and associated HM response. This information is critical for ensuring that our model accurately represents real-world systems and can be relied upon for further analysis and prediction.

The simulation starts from a non-equilibrium state (Figure 40) where only free gas is present (gas is not adsorbed initially). Due to gas adsorption, swelling occurs up to the equilibrium state and gas diffuses through the medium (both in the pores and in the particles). We perform different simulations by varying the value of the coupling coefficient α which linearly relates the solvation pressure to the amount of gas molecules in our closed system and plotted the final state condition in Figure 41. The relative error ($\frac{mass_t - mass_{t0}}{mass_{t0}}$) of the overall mass balance should be equal to zero as no mass is entering/existing the system. Unfortunately, due to the volumetric deformation (swelling), the relative error increases linearly as a function of the volumetric deformation (Figure 41 – dotted curve).

If the volumetric deformation remains below 3% (expected for typical coal matrix), the relative error for mass balance does not exceed 2% which can be considered acceptable. However, the induced volumetric deformation might be larger than 3% in some cases (e.g., when cleats are present in the simulated system), hence the relative mass balance error might become problematic. For that reason, we included a correction to the numerical scheme to resolve this problem by adding a source term to the mass balance equation for pores (see Chapter 4 for details). This additional source term takes into consideration the volumetric deformation of the pores over time such as:

$$\emptyset_{correction} = \frac{\Delta V_f \times \Delta t \times c^{t+\Delta t}}{V^{t+\Delta t}} \tag{3.50}$$

where $\Delta V_f = V_f^t - V_f^{t+\Delta t}$, with V^t the volume of the pore at t, and $V_f^{t+\Delta t}$ the volume of the pore at $t + \Delta t$, and $c^{t+\Delta t}$ is the concentration of pore.

Introducing this additional source term into equation (3.20) gives the following evolution of the concentration in each pore *i* over time:

$$c_i^{t+\Delta t} = \sum_{i=1}^{4} \frac{V_p\, A_{ik}}{V_f\, A_k} \left[\left(1 - \frac{s_k^t}{s_{k,max}}\right) K_{att} c_i^t - K_{det} \frac{s_k^t}{s_{k,max}} \right] \Delta t^{\frac{ad}{des}} + \sum_{i=1}^{4} \frac{S_{ij}}{V_f L_{ij}} \ \frac{2r}{3} \sqrt{\frac{8\mathrm{RT}}{\pi M_g}} (c_j^t - c_i^t) \Delta t^K + \emptyset_{correction} + c_i^t \tag{3.51}$$

We performed a second time the swelling experiments presented in Figure 41 with this correction applied to the numerical scheme. As shown in the figure, the relative error of the mass balance is equal to zero whatever is the amplitude of the volumetric deformation (related to the swelling coefficient here).

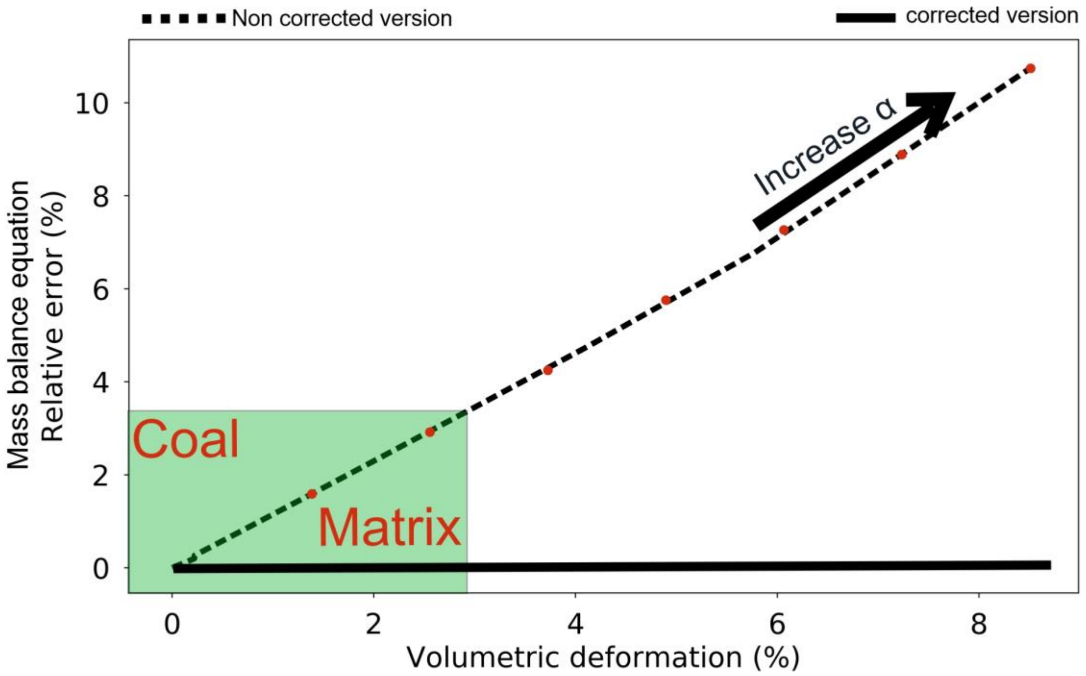

Figure 41. Evolution of the mass balance relative error $\frac{mass_t - mass_{t=0}}{mass_{t=0}}$ as a function of the volumetric deformation in systems subjected to swelling. The curves represent the equilibrium states obtained for different values of the swelling coefficient α with and without the correction applied to the numerical scheme Equation (3.50).

Chapter 4

Multi-scale single phase hydromechanical model for fractured coal

Chapter 4 : Multi-scale single phase hydromechanical model for fractured coal

4.1.Introduction

The intricate interplay of storage and transport mechanisms taking place in coal beds makes predicting CBM reservoir behavior a challenging task due to their structural characteristics. Coal beds inherently exhibit two porosity scales: the primary porosity, consisting of the micro and macropores within the matrix, and the secondary porosity, formed by the cleat networks (Figure 42) (Laubach et al., 1998). The primary porosity system hosts the majority of the enclosed gas, adsorbed as a layer on the solid phase's surface. Conversely, the cleats act as the principal conduit for fluid flow to and from the wellbore (Laubach et al., 1998; Shi and Durucan, 2004). These cleats are classified as face and butt cleats depending on their arrangement and origin. Face cleats are well developed persistent fractures that run parallel to one another. Butt cleats are non persistent fractures perpendicular to face cleats that terminate at the intersection with face cleats. Indeed, coalbeds permeability is directly dependent on the topology of the cleat network.

Understanding the coupling of coal mechanical behavior with ground water and gas flow and transport processes is an essential problem for CBM exploitation. Additionally, the gas specific adsorption/desorption induced deformations of coal add up to the complexity of the problem. A lot of experimental work has been done to relate adsorbed gas quantity and deformation in coal (Chikatamarla et al., 2004, 2004; Day et al., 2008b, 2008a; Harpalani and Chen, 1995; Levine, 1996b; Eric P. Robertson and Christiansen, 2005). Other experimental works focused on the sorption induced deformation of coal according to the gas type and coal ranks (Ceglarska-Stefańska and Brzóska, 1998; Harpalani and Schraufnagel, 1990b, 1990a; Moffat and Weale, 1955; Reucroft and Patel, 1986; St. George and Barakat, 2001; Zutshi and Harpalani, 2004). Finally, a lot of researchers tried to understand how transport of gas through the cleat and matrix and the associated hydromechanical couplings affect the permeability of coal (Gray, 1987; Mavor and Gunter, 2006; Palmer and Mansoori, 1998; Pekot and Reeves, 2003; Puri and Seidle, 1992; Robertson and Christiansen, 2008; Sawyer et al., 1990).

However, the complexity of coal system renders difficult precise analyses of the multiple processes involved. For instance, even though of great interest, transport experiments and studies involving analyses based on X-ray tomography, SEM, TEM etc. are time consuming and expensive and are highly affected by sample preparation, material composition, environment and methodology. Hence numerical approaches are needed (Bertrand et al., 2017; Chen et al., 2019a; Masoudian et al., 2014; Pekot and Reeves, 2003; Raoof et al., 2012; Sampath et al., 2020).

Continuum approaches have been massively used to model the hydro-mechanical behavior of coal (Chen et al., 2022b, 2019b; Lanetc et al., 2023a). Nonetheless, even though of great interest for large scale applications, they are based on phenomenological behavior laws that often fail to reproduce accurately the complex physics involved in coal. On the contrary, pore scale approaches, due to the level of detail they can describe, can improve our understanding of large scale behaviors as they can take into consideration the variation of many (if not all) the local system’s parameters (pore space geometries, fluid properties, and boundary conditions) and their related global effects (Meakin and Tartakovsky, 2009). Additionally, macroscopic (or “effective”) transport properties can be estimated through pore scale analyses through upscaling techniques. Pore-scale modelling techniques are well developed nowadays and are mainly based on particle-based methods, which include the lattice Boltzmann method (LBM) (Li et al., 2023; Pan et al., 2004; Peng et al., 2018) and the smoothed particle hydrodynamics (SPH) method (Tartakovsky et al., 2007).

These particle based methods are however inefficient at the meso-scale as they cannot take into consideration too many interconnected pores due to their computational cost (Tartakovsky et al., 2007). An alternative to these pore-scale particle methods are the pore network models (PNM)which have been used for decades to model multi or single-phase flow in porous media (Blunt, 2001; Fatt, 1956; Joekar-Niasar and Hassanizadeh, 2012; Piri and Blunt, 2005; Sweijen et al., 2017) as well as adsorption phenomena (Kainourgiakis et al., 1998; Raoof et al., 2013, 2010; Xu and Prodanović, 2018). Among these pore-scale models, only a few are able to describe hydromechanical (HM) couplings.

Our objective here is to present a pore scale model capable of describing flow and transport taking place in coal as well as the associated HM processes. For that purpose, we built upon the DEM-PFV model presented in Chapter 3 to propose a 3D model capable of describing the HM behavior of fractured coal. A pivotal aspect of this model lies in its capability to establish a direct correlation between the swelling (or shrinkage) of the coal matrix and the resulting permeability alterations within the cleats.

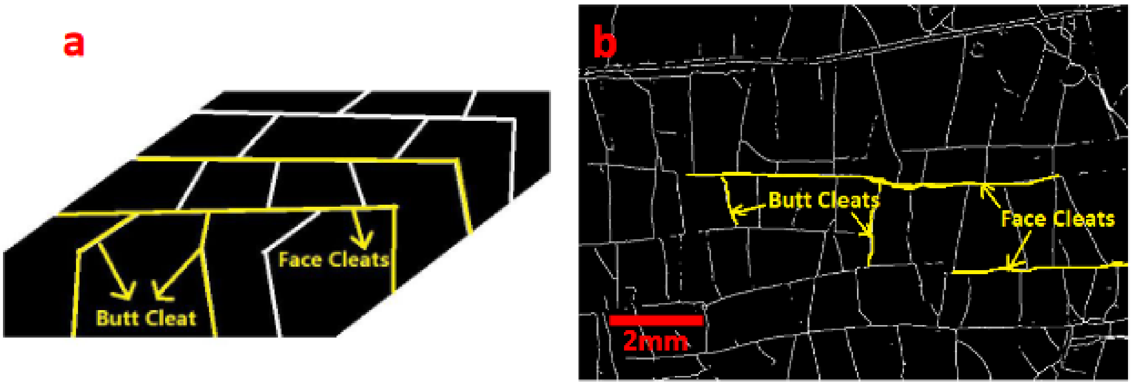

Figure 42 Illustration of face and butt cleats in a) a conceptual model, and b) reality (Jing, 2017).

4.2.Methodology

The modeling of the porous coal matrix is founded on the assumption that the solid phase consists of packed spherical particles bonded to one another, while the pore space is conceptualized as a network of interconnected pores (see Chapter 3 for details). In contrast, cleats are constructed as interconnected pores located in between coal matrix blocks. The following sections provide a comprehensive breakdown of the mechanical and transport models for the cleats, elucidate the underlying assumptions, and outline their respective implementation into the YADE Open DEM software.

4.2.1.Cleat representation

The DEM-PFV approach entails partitioning the voids within a particle assembly into tetrahedra through a weighted Delaunay triangulation of the particle centers, as depicted in Figure 43b. In the following, we will use the terms cleat-pore and matrix-pore to distinguish the fluid domain belonging respectively to the cleats and to the matrix. The cleat network is made up of interconnected cleat-pores, while the matrix porosity is made up of interconnected matrix-pores. Mass transport occurs within the cleats through advection between cleat-pores, and through a combination of Knudsen diffusion between cleat-pores and matrix-pores, and adsorption/desorption between cleat-pores and solid particles. Finally, the cleats can open and close mechanically through the contact network connecting its opposite walls.

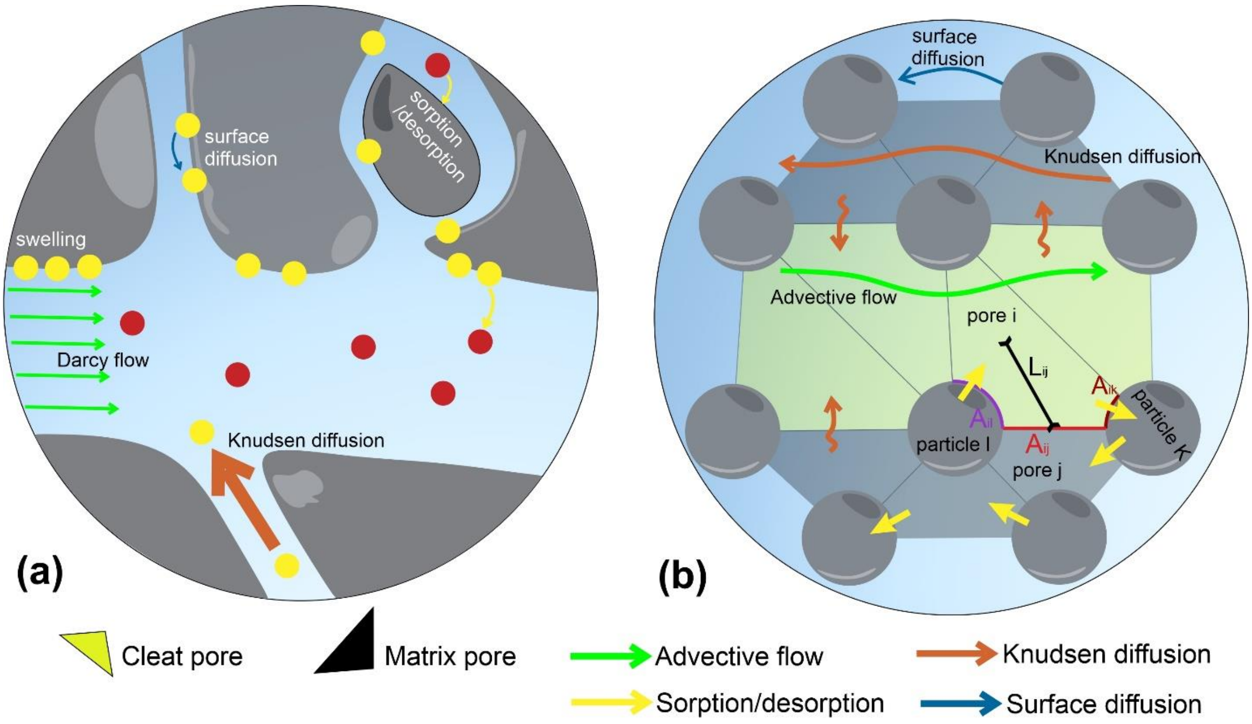

Figure 43 Mass transport and associated mechanisms in fractured coal: a) conceptual model, b) DEM-PFV model.

4.2.2.Mechanical scheme

The BPM enables to describe fractured rock by an explicit domain decomposition which consists in assigning dedicated behavior laws to the bonds/contacts making up the medium depending on their location “on” or “off” the fractures (Scholtès and Donzé, 2012). The only difficulty is to identify the bonds belonging to the cleat domain through their location in space with respect to the mean cleat plane. This can be done manually or automatically thanks to the use of a predefined discrete fracture network (DFN) meshed surface (see for instance the work by (Harthong et al., 2012; Scholtès et al., 2011)).

4.2.2.1.Coal matrix

The BPM depicting the coal matrix is presented in detail in Chapter 3 and we thus won’t repeat ourselves here since we use the exact same approach.

4.2.2.2.Cleats

The cleats' behavior is governed by the same elastic-cohesive-frictional laws used for the matrix (see Chapter 3). In the present work, we do not take advantage of the smooth contact logic proposed by (Scholtès and Donzé, 2012) to conform with the parallel plate model and simply assign specific properties to the bonds making up the cleats. This choice enables us to define the cleat transversal extension over several layers of particles instead of only two with the smooth contact logic. In such a case, the particles located within a cleat are simply considered as material points that do not participate to the mass transport scheme while ensuring the mechanical response of the cleat (Figure 44).

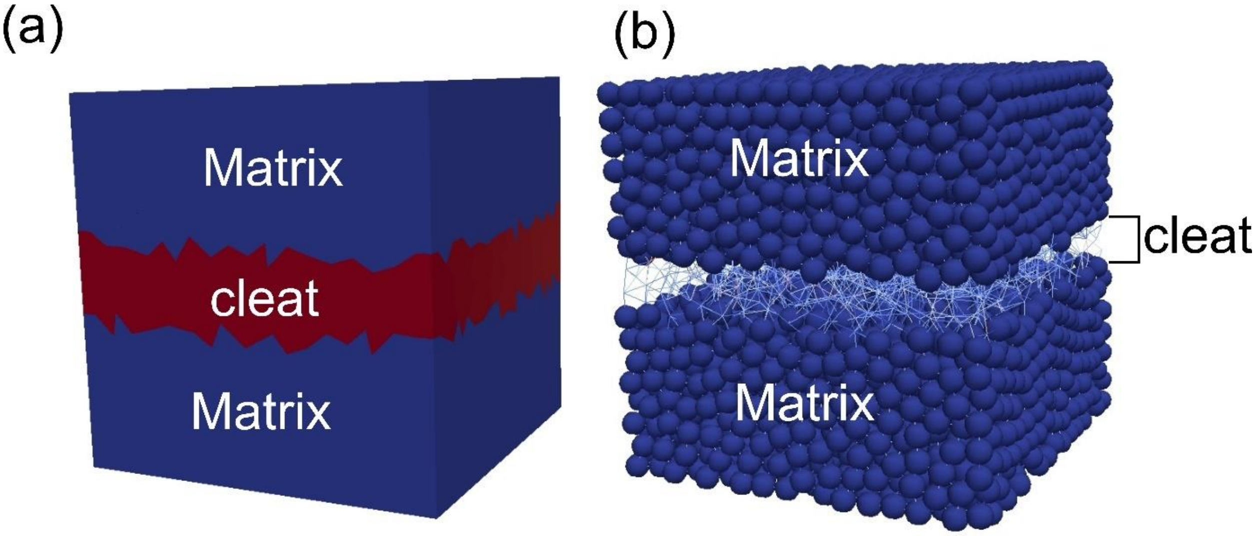

Figure 44 Illustration of a fractured coal system in YADE-DEM. a) pore finite volume domain. b) DEM domain.

4.2.3.Transport mechanisms

Broadly speaking, coal can be described as a dual porosity system with the cleats governing the overall coal permeability, and the matrix micropores housing diffusion processes such as Knudsen diffusion, adsorption/desorption, and surface diffusion, as illustrated in Figure 43. For instance, during an injection scenario, gas typically flows through the cleats, diffuses within the coal matrix, and then sorbs onto the solid phase, consequently leading to matrix swelling. As for the coal matrix, we assume in first approximation that water was first drained out of the domain through the largest cleats due to methane desorption and we also neglect the presence of residual water films (i.e., low capillary forces). We also assume that only a single component gas phase is present within our system (pure methane). In other words, we consider methane is present everywhere at the start of the simulation resulting in single-phase flow within the cleat system. This subsection will delve into a detailed examination of the transport mechanisms occurring within cleats and at their interface with the matrix (please refer to Chapter 3 for details about the transport mechanisms taking place in the matrix).

4.2.3.1.Mass transport at the matrix-cleat interfaces

4.2.3.1.1.Mass balance equation for boundary matrix-pores

As illustrated in Figure 45, some matrix-pores (*i* and *o*) are connected to cleat-pores (*p* and *j*) through one face of the tetrahedron they are built upon. Cleat-matrix exchanges are defined across this interface.

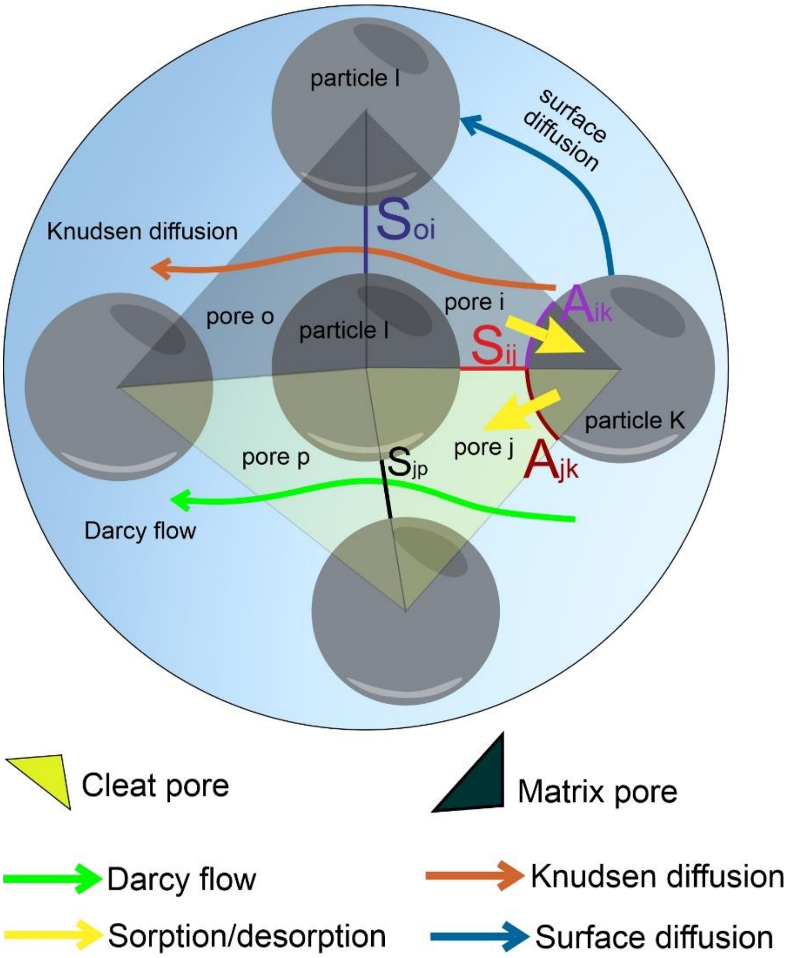

Figure 45 cleat-matrix interface representation in YADE-DEM and associated transport mechanisms.

Let V_f be the volume of boundary matrix-pore *i*. Integrating the continuity equation in pore *i* gives:

$$\int_{V_f}\frac{\partial c_i}{\partial t}dV + \int_{V_f}\vec{\nabla}\vec{J}_{pore_i}dV \ = 0 \tag{4.1}$$

where c_i is the concentration of gas in pore *i*, and $\vec{J}_{pore_i}$ represents the gas fluxes coming in and out of pore *i*.

Applying the divergence theorem to Equation (4.1)gives:

$$\int_{V_f}\frac{\partial c_i}{\partial t}.dV + \int_{\partial V_f}\vec{J}_{pore_i}.\vec{n}dS \ = 0 \tag{4.2}$$

In 3D, each interface-matrix-pore *i* is connected to 3 neighboring matrix-pores, *m* particles and 1 cleat-pore. The contour surface of pore *i* can thus be expressed as:

$$\partial V_f = \partial V_{pore_i,\ \mathrm{cleat}-pore_j} + \sum_{k=1}^{\mathrm{m}} \partial V_{pore_{\mathrm{i}},\ particle_k} + \sum_{o=1}^{3} \partial V_{pore_i,\ pore_o} \tag{4.3}$$

$$\partial V_f = S_{ij} + \sum_{k=1}^{\mathrm{m}} A_{ik} + \sum_{o=1}^{3} S_{io}$$

where S_{ij} represents the surface intersection between matrix-pore *i* and cleat-pore *j*, A_{ik} represents the surface intersection between particle *k* and pore *i*, and S_{io} represents the surface intersection between matrix-pore *i* and matrix-pore *o*.

Equation (4.2) can then be written as follows:

$$\int_{Vf} \frac{\partial \mathrm{c}_i}{\partial \mathrm{t}} dV = -\sum_{j=1}^{3} \int_{S_{io}} \vec{J}_{io}^{K}.\vec{n}dS - \sum_{k=1}^{m} \int_{A_{ik}} \vec{J}_{ik}^{ad}.\vec{n}dS - \int_{S_{ij}} \vec{J}_{ij}^{K}.\vec{n}dS \tag{4.4}$$

where $\vec{J}_{ij}^{K}$ is the Knudsen diffusion flux between matrix-pore i and cleat-pore j, $\vec{J}_{ik}^{ad}$ is the adsorption/desorption flux between pore *i* and particle k, and $\vec{J}_{io}^{K}$ is the Knudsen diffusion flux between matrix-pore i and matrix-pore *o*. In chapter 3, the equations governing diffusion through matrix pores and particles were presented. Here, we focus on the additional term describing diffusion between matrix-pores and cleat-pores defined as follows:

$$\emptyset_K = \int_{S_{ij}} \vec{J}_{ij}^{K}.\vec{n}dS \tag{4.5}$$

For a single-species phase flow along a straight circular capillary tube, the Knudsen diffusion flux can be defined as (Do, 1998):

$$\vec{J}^{K} = -D^{K} \frac{1}{RT} \vec{\nabla} p \tag{4.6}$$

with $p = cRT$ the gas pressure (Pa), R the gas constant (j/mol/k) and T the absolute temperature (K). The Knudsen diffusion coefficient D^K (m^2/s) is given by:

$$D^K = \frac{2r}{3} \sqrt{\frac{8RT}{\pi M_g}} \tag{4.7}$$

with r the pore hydraulic radius which represents the ratio between the throat's volume and solid-fluid interfaces area (Chareyre et al., 2012), and M_g the molar mass (kg/m^3).

Then equation (4.5) can be written as follows:

$$\emptyset_K = \frac{S_{ij}}{L_{ij}} \frac{2r}{3} \sqrt{\frac{8}{\pi RT M_g}} \left(p_j^t - p_i^t\right) = \frac{S_{ij}}{L_{ij}} \frac{2r}{3} \sqrt{\frac{8RT}{\pi M_g}} \left(c_j^t - c_i^t\right) \tag{4.8}$$

Here, we assume that the pressure drop prevails within the matrix, hence, we may consider that p_j is also the pressure at the interface between pores *i* and *j*. Then L_{ij} corresponds to the distance between the center of cell *i* and the interface between cell *i* and cell *j* as represented in Figure 43b.

Finally, considering both sorption Equation (3.13) and Knudsen diffusion Equation (3.19)), as well as the additional term $\emptyset_K$, then the evolution of each boundary matrix-pore *i* concentration can be obtained by an explicit integration over time such as:

$$c_i^{t+\Delta t} = \sum_{i=1}^{4} \frac{V_p\, A_{ik}}{V_f\, A_k} \left[\left(1 - \frac{s_k^t}{s_{k,max}}\right) K_{att} c_i^t - K_{det} \frac{s_k^t}{s_{k,max}} \right] \Delta t^{\frac{ad}{des}} + \sum_{i=1}^{3} \frac{S_{io}}{V_f L_{io}} \frac{2r}{3} \sqrt{\frac{8\mathrm{RT}}{\pi M_g}} (c_o^t - c_i^t) \Delta t^K + \frac{\emptyset_K \Delta t^K}{V_f} + c_i^t \tag{4.9}$$

with Δt_{des}^{ad} and Δt^{K} the associated time steps.

4.2.3.1.2.Mass balance equation for inter-boundary particles

As illustrated in Figure 43, at the cleat-matrix interface, boundary particles are connected to both matrix-pores and cleat-pores.

Let V_p be the volume of a particle k in contact with both a matrix-pore and a cleat-pore. Integrating the mass balance equation on particle k gives:

$$\int_{V_p} \frac{\partial s_k}{\partial \mathrm{t}} dV + \int_{V_p} \vec{\nabla}.\vec{J}_{particle_k}\, dV \;\; = 0 \qquad (4.10)$$

where s_k is the adsorbed concentration on particle k, and $\vec{J}_{particle_k}$ represents the gas fluxes coming in and out of particle k.

Applying the divergence theorem to Equation (4.10) gives:

$$\int_{V_p} \frac{\partial s_k}{\partial \mathrm{t}} dV + \int_{\partial V_p} \vec{J}_{particle_k}.\vec{n} dS \;\; = 0 \qquad (4.11)$$

Since each particle is connected to N particles, to M matrix-pores, and to L cleat-pores, then the contour surface of each particle can be expressed as:

$$\partial V_p = \sum_{l=1}^{N} \partial V_{particle\ k,particle\ l} + \sum_{i=1}^{M} \partial V_{particle\ k,pore\ i} + \sum_{j=1}^{L} \partial V_{particle\ k,cleat-pore\ j} \qquad (4.12)$$

$$\partial V_p = \sum_{l=1}^{N} S_{kl} + \sum_{i=1}^{M} A_{ki} + \sum_{j=1}^{L} A_{kj}$$

where S_{kl} is the intersection surface area between particle k and particle l, A_{ki} is the intersection surface area between particle k and matrix-pore i, and A_{kj} is the surface intersection area between particle k and cleat-pore j.

Equation (4.11) can then be written as follows:

$$\int_{V_p} \frac{\partial s_k}{\partial \mathrm{t}} dV = -\sum_{l=1}^{N} \int_{S_{kl}} \vec{J}_{kl}^{S}.\vec{n} dS - \sum_{i=1}^{M} \int_{A_{ki}} \vec{J}_{ki}^{ad} \vec{n}.dS - \sum_{j=1}^{L} \int_{A_{kj}} \vec{J}_{kj}^{ad} \vec{n}.dS \qquad (4.13)$$

where $\vec{J}_{kl}^{S}$ is the surface diffusion flux between particle k and particle l, $\vec{J}_{ki}^{ad}$ is the adsorption/desorption flux between particle k and matrix-pore i, and $\vec{J}_{kj}^{ad}$ is the adsorption/desorption flux between particle k and cleat-pore j.

In chapter 3, the equations governing surface diffusion between particles and sorption within the matrix were presented. Here, we focus on the additional term describing sorption within the cleats defined as follows:

$$\emptyset_s = \int_{A_{kj}} \vec{J}_{kj}^{ad} \vec{n}.dS \qquad (4.14)$$

According to chapter 3, Equation (3.19) becomes:

$$\int_{A_{kj}} \vec{J}_{kj}^{ad}.\vec{n} dS = \frac{A_{kj}}{A_k} \left[K_{det} \frac{s_k^t}{s_{k,max}} - \left(1 - \frac{s_k^t}{s_{k,max}}\right) K_{att} c_j \right] \times V_p \qquad (4.15)$$

where s_k (mol/m^3) is the solute concentration adsorbed on the surface of particle *k*, A_k is the overall surface of particle *k*, and V_p is the volume of particle *k*.

Finally, considering both sorption and surface diffusion as defined within the matrix (Chapter 3, Equation (3.26) and Equation (3.19))as well as the additional term $\emptyset_s$, the evolution of each particle concentration can be obtained by an explicit integration over time such as:

$$s_k^{t+\Delta t} = \sum_{i=1}^{M} \frac{A_{ki}}{A_k}\left[\left(1-\frac{s_k^t}{s_{k,max}}\right)K_{att}c_i^t - K_{det}\frac{s_k^t}{s_{k,max}}\right]\Delta t^{\frac{ad}{des}} + \sum_{l=1}^{N} \theta \frac{D^S\, S_{kl}}{V_p\, L_{kl}}(s_k^t - s_l^t)\Delta t^{sd} + \sum_{j=1}^{L} \frac{\emptyset_s \Delta t^{\frac{ad}{des}}}{V_p} + s_k^t \tag{4.16}$$

with $\Delta t^{\frac{ad}{des}}$ and Δt^{sd} the associated time steps.

4.2.3.1.3.Mass transport within the cleats

Flow occurs through advection within the cleats. To describe such a flow within the cleat-pore network of the DEM-PFV scheme, a Stokes' type of flow is established, similarly to what has been initially proposed by (Papachristos et al., 2017) to describe compressible flow in fractured rocks.

Let V_c be the volume of a pore *j* saturated with fluid (gas). Integrating the continuity equation in pore *j* gives:

$$\int_{Vc} \frac{\partial \rho_f}{\partial t} dV = -\int_{Vc} \nabla.(\rho_f v) dV \tag{4.17}$$

where $\rho_f$the fluid density and *v* is the fluid velocity. Note that ρ_f is equal to the mass concentration of gas *c* due to the assumption of single-component gas phase.

Applying the divergence theorem to equation (4.17) gives:

$$\int_{Vc} \frac{\partial c}{\partial t} dV = -\int_{S_{jp}} (cv).\vec{n} dS - \int_{S_{ij}} (cv).\vec{n} dS - \int_{A_{jk}} (cv).\vec{n} dS \tag{4.18}$$

where S_{jp} is the surface intersection between cleat pore j and cleat pore p.

Here, we consider that p_j and p_i are equal to the pressure at the cleat-matrix interface. This leads to:

$$(cv).\vec{n} = -D_k \nabla c.\vec{n}, \text{ for pores} \tag{4.19}$$

and to

$$(cv).\vec{n} = \left[K_{det}\frac{s_k^t}{s_{k,max}} - \left(1-\frac{s_k^t}{s_{k,max}}\right)K_{att}c_j\right] \times V_p, \text{ for particles} \tag{4.20}$$

According to equations (4.19) and (4.20) and introducing *u* as the interface velocity of contour ∂V_c, then equation (4.18) becomes:

$$\int_{Vc} \frac{\partial c}{\partial t} dV = -\int_{S_{jp}} c(v-u).\vec{n} dS - \int_{S_{jp}} cu.\vec{n} dS - c\emptyset_s - c\emptyset_k \tag{4.21}$$

For compressible fluid, the bulk modulus K_f relates the time derivative of c and P_j :

$$K_f = c\frac{\partial Pj}{\partial c} \tag{4.22}$$

Then equation (4.21) becomes:

$$\int_{Vc}\frac{1}{K_f}\frac{\partial P_j}{\partial t}dV = -\sum_o^4 \int_{Sjp}(v-u).\vec{n}dS - \dot{V}_{c,j} - \frac{\emptyset_S}{K_f} - \frac{\emptyset_K}{K_f} \tag{4.23}$$

where $\dot{V}_{c,j}$ is the time derivative of the volume of the pore, S_{jp} is the surface intersection between cleat pores, and V_c is the volume of pore *j* (Figure 45).

We then link the pressure jump between two cleat-pores through the conductance of the interpore throat so that equation (4.23) becomes:

$$\dot{P_j} = -\frac{k_f}{V_{f,j}}\left[\dot{V}_{c,j} + \sum_o^4 k_{jp}(P_j - P_p) - \frac{\emptyset_K}{k_f} - \frac{\emptyset_S}{k_f}\right] \tag{4.24}$$

with k_{jp} the local conductance of the throat between pore *j* and pore *p*.

According to (Scholtès et al., 2015), the finite difference of equation (4.24) gives:

$$\sum_{p=0}^4 k_{jp}P_p^t - (\beth_i + \sum_{p=0}^4 k_{jp})P_j^t = \dot{V}_{c,j}^{t-1/2} - \beth_i P_j^{t-1} - \emptyset_K - \emptyset_s \tag{4.25}$$

$$\text{With } \beth_i = \frac{V_{f,j}}{k_f \Delta t}$$

where the time-centered evaluation of˙ $\dot{V}_{c,j}^{t-1/2}$ is obtained from mid-step velocities of the particles.

Here, intercleat-pores flow is governed by the parallel plate model (Zhang et al., 2007; Zimmerman and Bodvarsson, 1996). Thus, the local conductivity k_{jp} can be calculated as:

$$k_{jp} = -\frac{h_{jp}^3}{12\mu} \tag{4.26}$$

where μ is the dynamic viscosity of the fluid and $h_{jp}^{t+\Delta t} = h_{jp}^t + \Delta h_{jp}$ is the cleat hydraulic aperture updated each time step using the following harmonic average of the volumetric deformation of the interconnected cleat-pores:

$$\Delta h_{jp} = h_{jp}^t \frac{2}{\frac{1}{\frac{\Delta V_j}{V_j}} + \frac{1}{\frac{\Delta V_p}{V_p}}} \tag{4.27}$$

where ΔV_j and ΔV_p represent the volume difference between two consecutive time step of pores *j* and *p*.

4.3.Results

4.3.1.Mass balance validation

Our primary focus in this investigation centers on examining the coupling between cleat and matrix and assessing our model's ability to accurately retain mass conservation in the simulated medium.

For that purpose, we constructed a numerical assembly with dimensions of 10 mm x 10 mm x 10 mm, consisting of 5,000 particles. The sample contains a single persistent cleat positioned at the center of the sample and was subjected to different loading paths. For the four cases presented here, we assume a closed system with no fluxes possible on all sides of the sample.

In the first two cases, we examine the mass transfer between the matrix and cleat without adsorption/desorption of gas molecules, whereas in the latter two cases, we add adsorption/ desorption mechanisms of gas molecules. From an analytical standpoint, the total mass of gas molecules should remain constant within the system, and we should verify the following relation at every time of the simulation:

$$total\ mass = mass\ in\ cleats\ (mol) + mass\ in\ matrix\ (mol) \tag{4.28}$$

where

$$mass\ in\ cleats\ (mol) = free\ gas\ mass\ (mol) \tag{4.29}$$

and

$$mass\ in\ matrix = adsorbed\ gas\ mass\ (mol) + free\ gass\ mass\ (mol) \tag{4.30}$$

Table 6

Test cases and corresponding model parameters.

Parameter	Test case 1	Test case 2	Test case 3	Test case 3b	Test case 4	Test case 5
D^K	1e-8	1e-8	1e-8	1e-8	1e-8	1e-8
D^{sd}	1e-9	1e-9	1e-9	1e-9	1e-9	1e-9
$\propto$	-	-	-	0,10,20	-	0,10,20,30
$K_d = k_{att}/k_{det}$	-	-	8e-4	8e-4	8e-4	8e-4
k_{att}	-	-	24e-8	24e-8	24e-8	8e-8
k_{det}	-	-	3e-4	3e-4	3e-4	1e-4
Temperature T (K)	328	328	328	328	328	328
Gas constant R (J.mol^{-1}.K^{-1})	8.314	8.314	8.314	8.314	8.314	8.314
Molar mass M_g (g.mol^{-1})	44.01	44.01	44.01	44.01	44.01	44.01
s_{max} (mol.m^{-3})	2400	2400	2400	2400	2400	2400
Cleat thickness (mm)	0.002	0.002	0.002	0.002	0.002	0.002
Young modulus E (GPa) *	4.550	4.550	4.550	4.550	4.550	4.550
Poisson ratio υ (-)*	0.225	0.225	0.225	0.225	0.225	0.225
Skeletal density (kg.m^{-3})	1303	1303	1303	1303	1303	1303

Biot coefficient b (-)	1	1	1	1	1	1
Initial cleat aperture $h^{t=0}$(m)	0.002	0.002	0.002	0.002	0.002	0.002

4.3.1.1.Test case 1: matrix to cleat gas transfer.

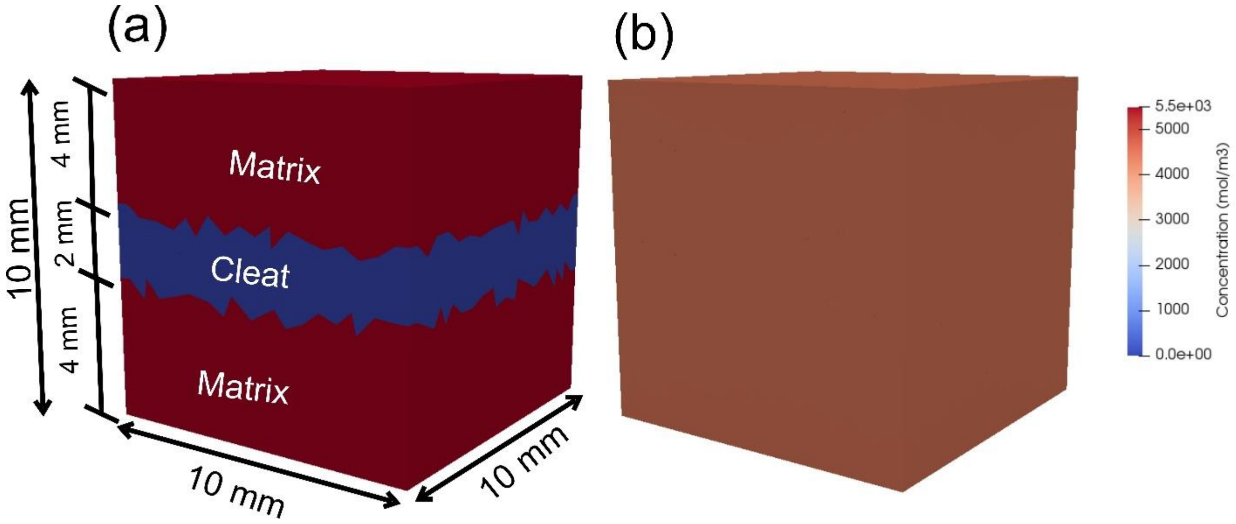

Figure 46 Test case 1: matrix to cleat gas transfer: a) fully gas saturated coal matrix and gas unsaturated cleat at t=0, b) gas concentration at t=inf.

In this first test case, we study the gas transfer from the coal matrix to a cleat without adsorption/desorption of gas molecules on the solid particles. At the initial state, the matrix is fully gas-saturated while the cleat does not contain any gas as illustrated in Figure 46a.

Figure 47a provides an illustration of the evolution over time of the mean average concentration within both the coal matrix and the cleat. As the time passes, the average concentration within the coal matrix decreases due to the diffusion of gas toward the cleat. Consequently, there is an observable increase in the mean average concentration within the cleat. At the end of the simulation, the system reaches equilibrium with a homogenized concentration in the entire system.

Figure 47b, presents the percentage of mass entering and leaving both the matrix and the cleat as well as the overall balance. Notably, we can observe that the total amount of gas mass entering the cleat corresponds to approximately 19% of the initial mass. This value is equivalent to the mass escaping from the coal matrix. As expected for a closed system, the total mass does not evolve over time, hence validating our numerical scheme for matrix to cleat gas transfer.

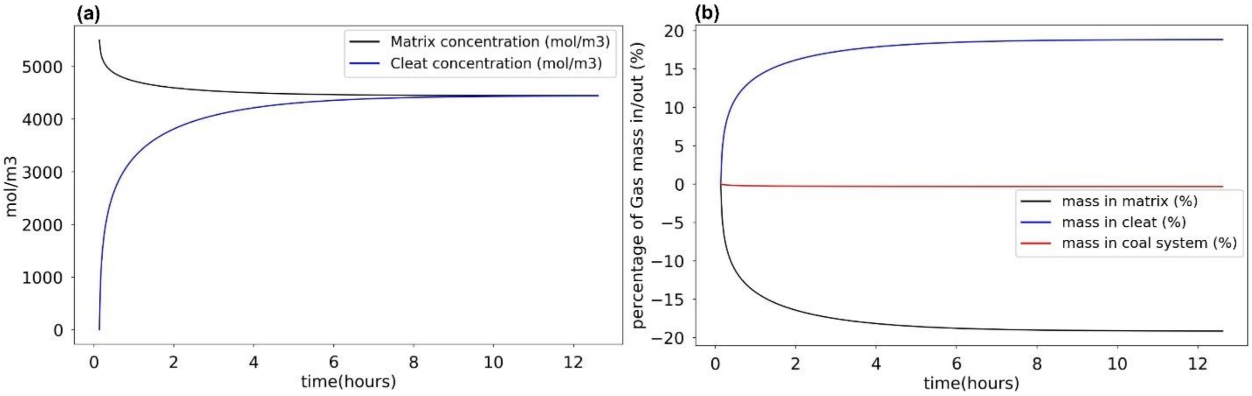

Figure 47 a) Evolution over time of the mean average concentrations in matrix and cleat. b) Variations of mass within the whole system.

4.3.1.2.Test case 2: cleat to matrix gas transfer

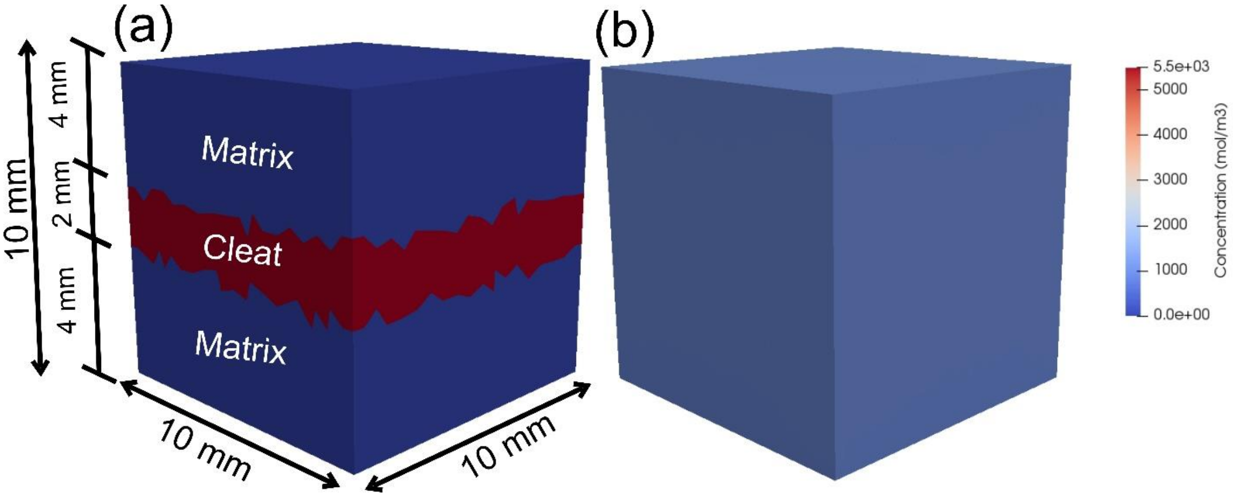

Figure 48 Test case 2: cleat to matrix gas transfer: a) fully gas saturated cleat and gas unsaturated coal matrix at t=0, b) gas concentration at t=inf

Unlike test case 1, the cleat is fully gas-saturated, and the matrix does not contain any gas Figure 48a).

Figure 49a provides an illustration of the evolution over time of the mean average concentration within both the coal matrix and the cleat. As time passes, the average concentration within the cleat decreases due to the diffusion of gas toward the matrix. At the end of the simulation, the system reaches equilibrium with a homogenized concentration in the entire system.

Figure 49b presents the percentage of mass entering and leaving both the matrix and the cleat as well as the overall balance. Notably, we can observe that the total amount of gas entering the matrix corresponds approximately to 80% of the initial mass. This value is equivalent to the mass escaping from the cleat. As expected for a closed system, the total mass does not evolve over time, hence validating our numerical scheme for cleat to matrix gas transfer.

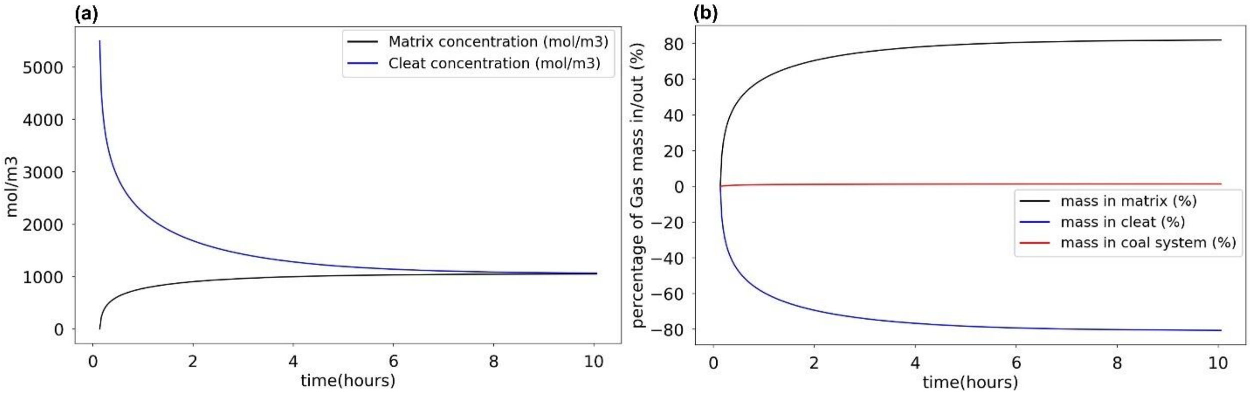

Figure 49 a) Evolution over time of the mean average concentration in matrix and cleat. b) Variations of mass within the matrix+cleat system.

4.3.1.3.Test case 3: matrix to cleat gas transfer with sorption

Examining cases involving sorption is essential to evaluate its impact on mass conservation within our system.

Our investigation starts with a scenario where the matrix, including pores and particles, is fully saturated with gas, while the concentration is null within the cleats, as illustrated in Figure 50a and c. It is important to emphasize that, here again, we consider a closed system, therefore implying zero fluxes on all sides of the sample. Moreover, sorption is governed by Langmuir isotherm (see Chapter 3 for details).

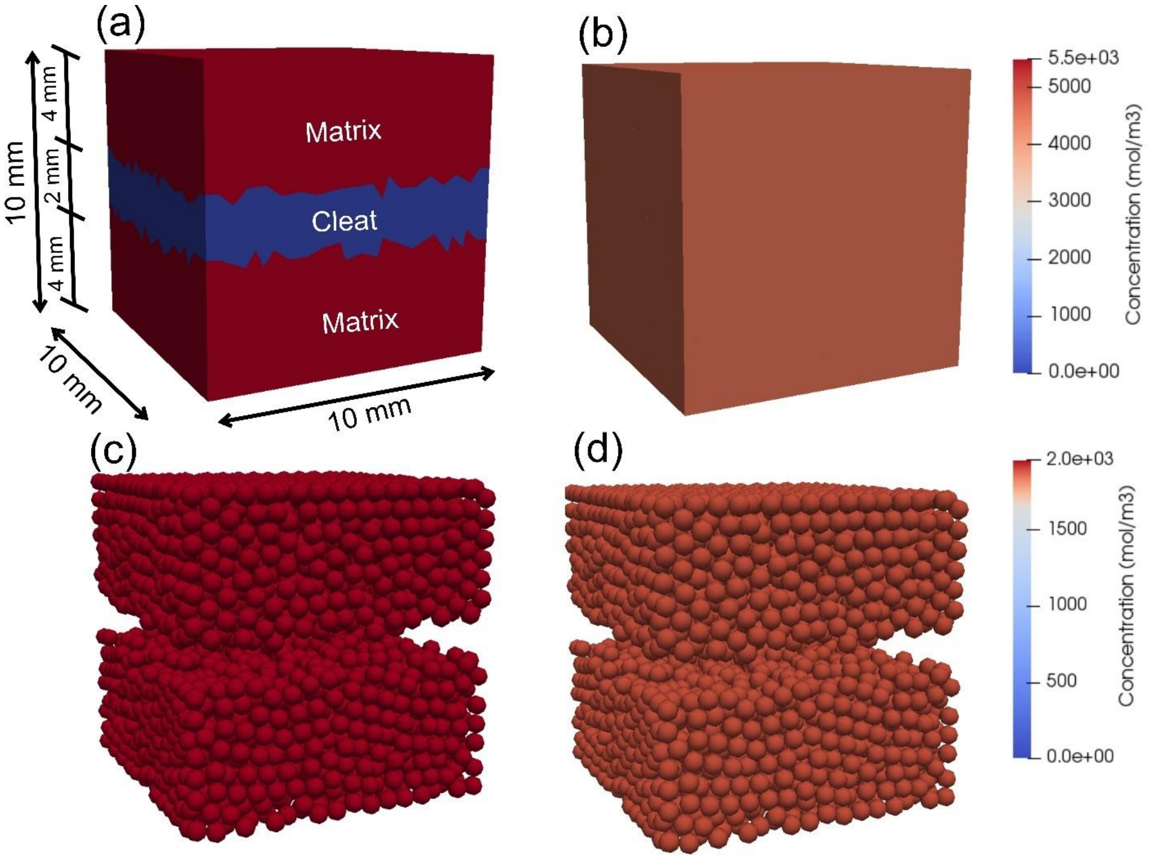

Figure 50 Test case 3: matrix to cleat mass transfer with sorption: a) fully gas-saturated matrix pores and gas unsaturated cleat at t=0, b) concentration of gas within the pores and cleat at t = inf c) fully saturated particles at t=0, d) particle’s gas concentration at t=inf.

As illustrated in Figure 51a, the mean average concentration within the matrix pores undergoes a progressive decrease due to the migration of gas molecules toward the cleat, coupled with a minor reduction in the amount of gas adsorbed on the solid particles in accordance with the Langmuir isotherm. Subsequently, an equilibrium state is achieved after 35 hours, at which point the concentration within the matrix pores matches the concentration within the cleat, as illustrated by the convergence of the black and blue curves in Figure 51a. Due to the difference between surface and Knudsen diffusion coefficient values, gas diffuses faster through the solid phase (particles) and reaches equilibrium sooner. Furthermore, it is noteworthy that the steady-state gas concentrations of the adsorbed gas on particles and of the free gas within the pores (both in matrix and cleats) are in equilibrium with respect to the Langmuir isotherm stated in equation (3.17) (chapter 3), as shown in Figure 51a.

Examining the mass balance, it appears that the amount of gas entering the cleat, approximately 13%, matches the percentage of gas exiting the matrix, with an overall balance equal to zero, thereby confirming the validity of our model (Figure 51b).

It's worth noting that in test case 3, the percentage of mass entering/exiting each domain is lower compared to test case 1. This discrepancy is attributed to the higher initial mass content within the matrix, primarily due to the presence of both adsorbed gas and free gas molecules.

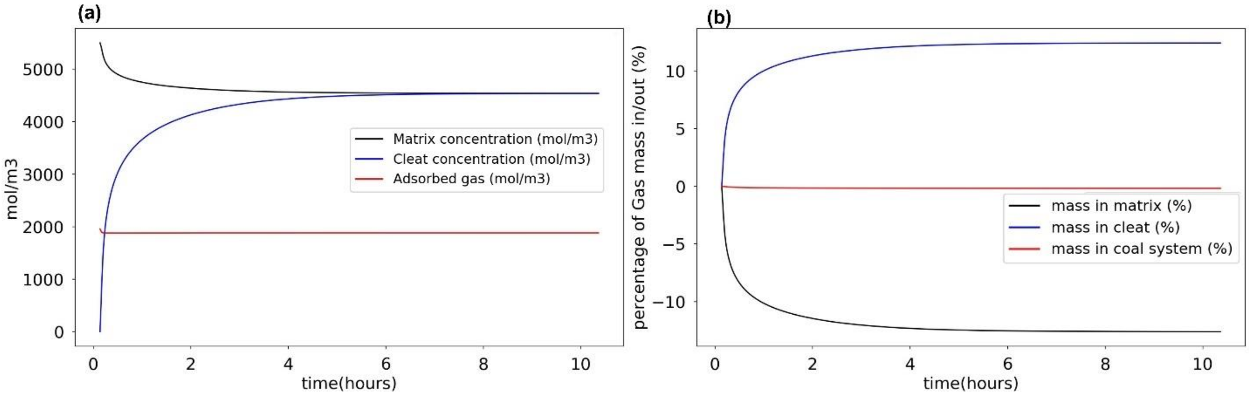

Figure 51 a) Evolution over time of the mean average concentration in matrix, cleat, and particles. b) Variations of mass within the whole system.

4.3.1.4. Test case 4: cleat to matrix gas transfer with sorption

In this test case we consider a fully saturated cleat with an unsaturated gas coal matrix (Figure 52). As for test case 3, sorption is governed by the Langmuir isotherm.

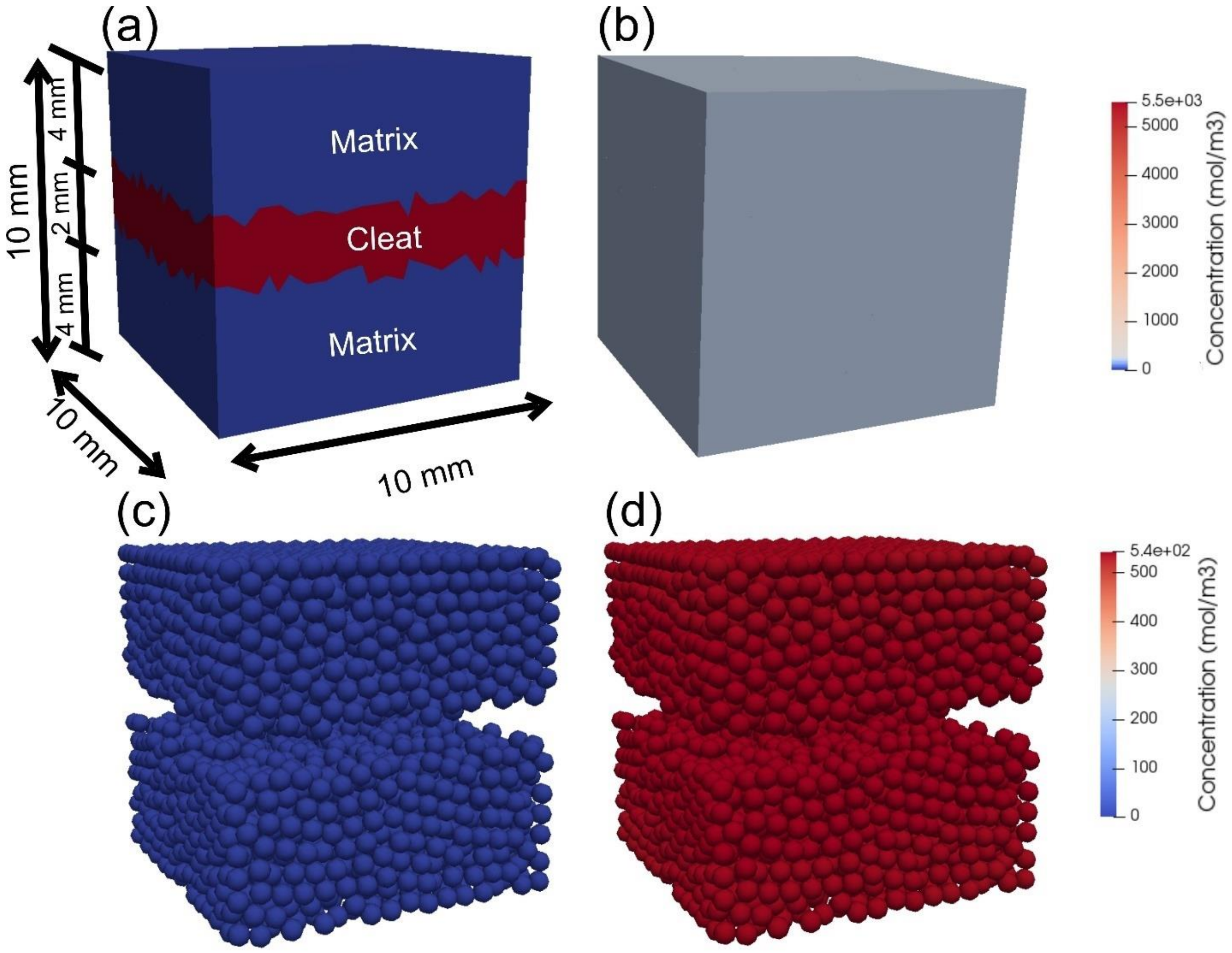

Figure 52 Test case 4: cleat to matrix mass transfer with sorption: a) fully gas saturated cleat and gas unsaturated coal matrix at t=0, b) concentration of gas within the pores and cleat at t=inf, c) gas unsaturated particles at t=0, d) particles' concentration at t=inf.

As illustrated in Figure 52a, the cleat concentration diminishes as gas migrates toward the matrix. It eventually stabilizes and balances with the concentration within the pores of the coal matrix, reaching 350 mol/m^3.

Here again, the mass balance is verified with 93% of mass entering the matrix and 93% escaping from the cleat (Figure 53b), the overall variation of mass remaining equal to 0% during the entire simulation.

It's worth highlighting that the percentage of mass entering and exiting each domain is higher compared to test case 2. This is due to the sorption effects present in test case 4, which produces a greater migration of gas molecules from the cleat toward the matrix.

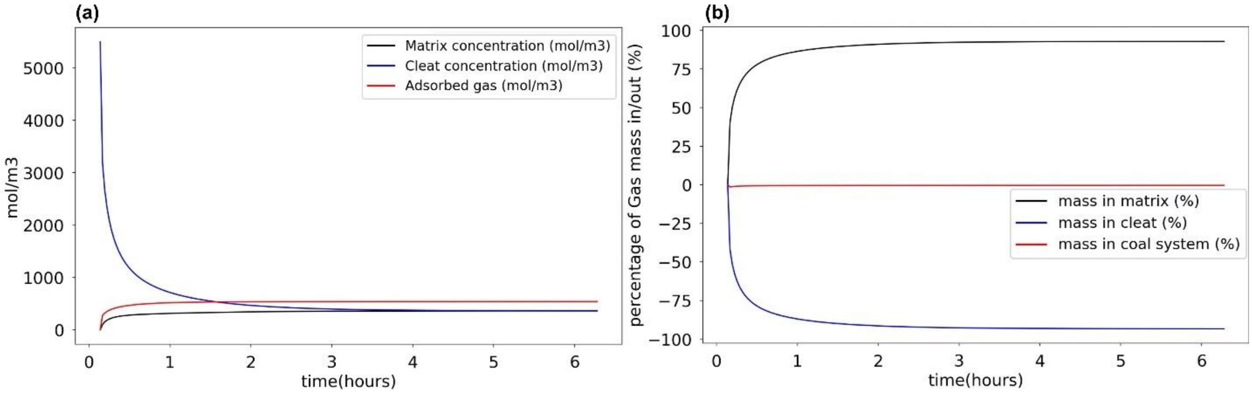

Figure 53 a) Evolution over time of the mean average concentration in the matrix, the cleat, and the particles. b) Variation of mass within the whole system

4.3.1.5.Influence of some numerical aspects

Since the transport calculations are made based on the disretization of the domain through a tetrahedral mesh, it is important to assess its influence on the model's predictions, especially when this mesh is updated to conform with the deformation of the medium.

In Figure 54a, we illustrate the relative error in the mass conservation induced by the frequency of the mesh update when running test case 4 (the PFV mesh needs to be updated when deformation occurs). It is shown that a smaller mesh update interval results in a larger relative error. This counterintuitive phenomenon occurs because the mesh updates tend to add or to exclude cells to the previous mesh based on the new position of the particles, which, in turn, affects the exchange surfaces and the cells' volumes, and thus the mass fluxes. Overall, one can note that the error induced by mesh update remains somewhat limited (<1%).

The use of random particles' packing can generate exceedingly small "flat" cells with volumes that are two orders of magnitude smaller than the average cell size. These flat cells pose a risk of inducing numerical instability as they require very small-time steps to be accommodated by the numerical scheme. To mitigate this issue, we introduced a shape-based criterion to disregard these cells and exclude them from the calculation. It is evident that, as shown in Figure 54b, these cells indeed are the source of a numerical error that tends to increase over time.

Finally, as illustrated in Figure 54c, the relative error in the mass balance is directly influenced by the chosen time step. As expected, when the time step increases, the relative error also increases. Hence, it is advisable to maintain a time step smaller than the critical one (see chapter 3 for maintaining stable simulation). Nevertheless, even with a critical time step, the relative error remains below 1%.

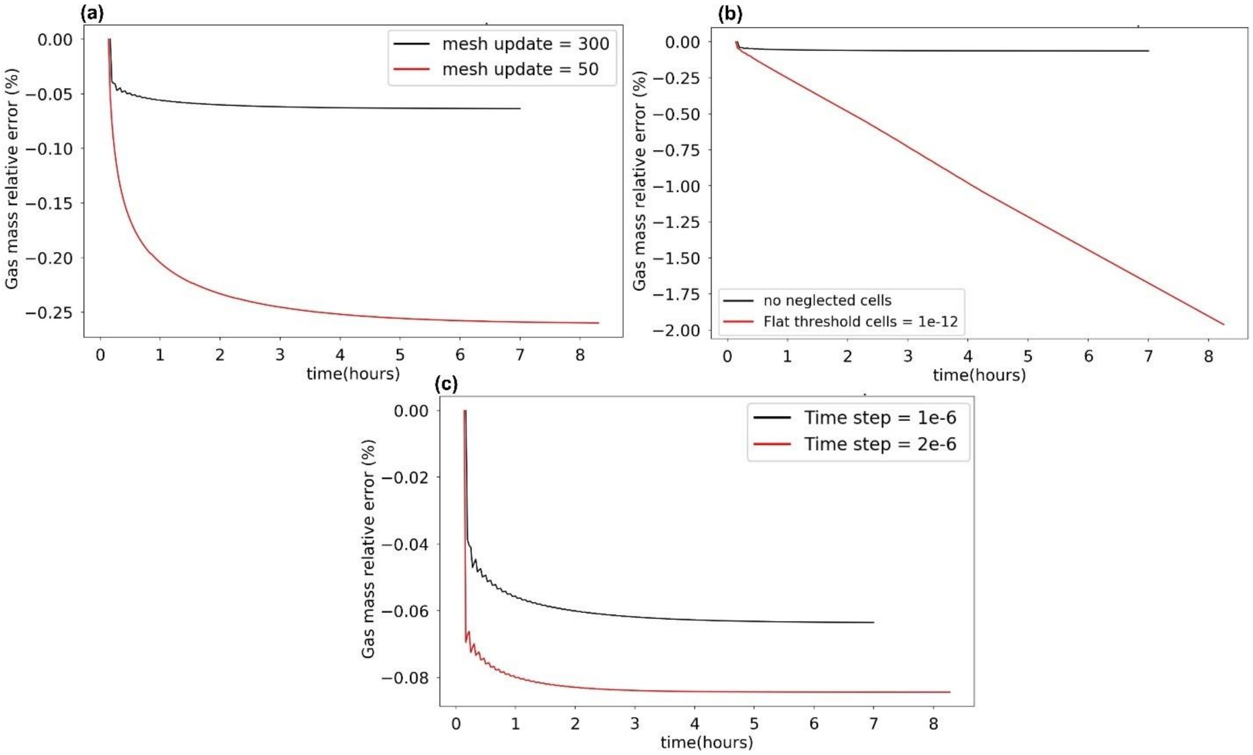

Figure 54 Changes in the relative error ($\frac{mass_t - mass_{t0}}{mass_{t0}}$) in mass balance over time as a function of: a) the mesh update interval, b) the flat cell threshold, c) the timestep.

4.3.2.Hydromechanical coupling.

In this section, we study how the stress components and volumes of both matrix and cleat evolve over time during test case 3 and test case 3b considering both non swelling and swelling scenarios.

4.3.2.1.Test case 3: non-swelling fractured sample

According to the poro-elasticity theory (Detournay and Cheng, 1993), the role of pore pressure (denoted as "p") in influencing the deformation of saturated porous media is defined in relation to the effective stress, expressed as follows:

$$\sigma' = \sigma - bp \tag{4.31}$$

where σ' is the effective stress, σ is the total stress, and b is the Biot coefficient equal to $1 - \frac{K}{K_s}$ with K the bulk modulus of the medium, and K_s the bulk modulus of the solid phase.

In our model, we can neglect swelling effects due to solvation pressure by simply defining the swelling coefficient α=0 (please refer to Chapter 3 for details). We thus use this case as a baseline condition for further observations. Furthermore, in this study, b=1 as the particles are assumed to be rigid (K_s=inf) and all the pores are connected (see Chapter 3 for explanations).

At t=0, the matrix is saturated with gas (methane) at a given pressure. Because the boundary walls are fixed, this instantaneous saturation results in a rapid increase of both the effective stress and the total stress, as seen in Figure 55a. This leads to a sudden volume increase of the matrix, accompanied with an equivalent reduction of the cleat volume (Figure 55b). However, as gas starts to percolate from the matrix toward the cleat, the matrix pore pressure decreases, accompanied with a reduction of its volume, while the cleat pore pressure begins to rise accompanied by an increase of its volume. After the initial perturbation, the total stress gradually decreases to reach a plateau at equilibrium. It is important to note that the effective stress equation (4.31) is verified at all time during the simulation, despite the dynamic response of the system at the beginning of the loading. The remaining volumetric deformations of both the matrix and cleat result from the change in pore pressure in the overall system (and associated effective stress change).

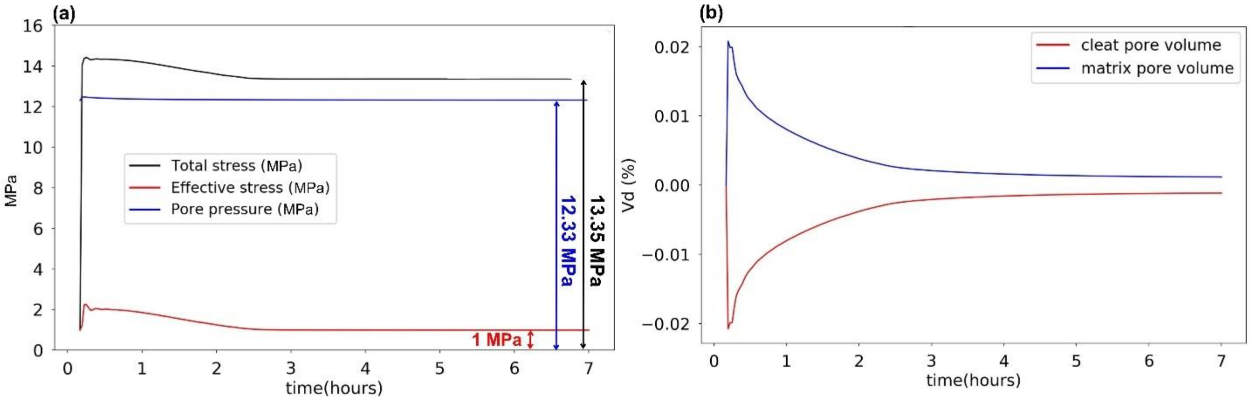

Figure 55 Test case 3 without swelling: evolution over time of a) the pore pressure, total stress, and effective stress, and b) the volumetric deformation of both cleat and matrix.

4.3.2.2.Test case 3b: swelling fractured sample

In this section, we explore the swelling behavior for various values of the swelling coefficient α. As previously discussed in Chapter 3, α plays a crucial role in regulating the solvation pressure, which, in turn, governs the induced swelling strain. To better assess its HM contribution, we make vary α from 0 to 20 during the simulation (Figure 56).

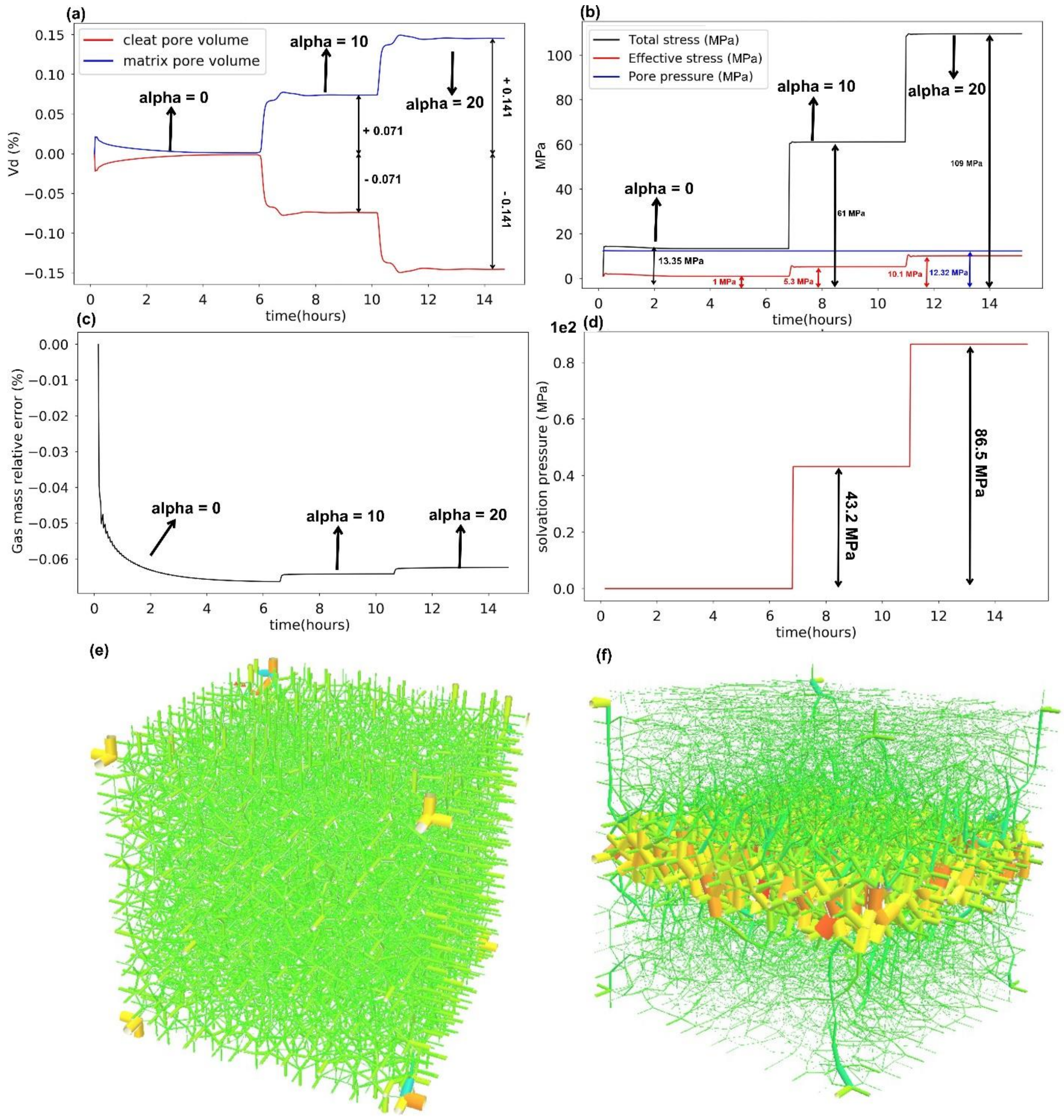

Figure 56 Test case 3 with swelling: evolution over time of: a) volumetric deformation, b) total stress, pore pressure and effective stress, c) changes in mass balance, and d) solvation pressure in a simulation where α is increased stepwise. e) contact stress (effective stress) between particles with alpha = 0. d) contact stress (effective) between particles with alpha = 20.

Increasing α during the simulation leads to higher solvation pressure in the matrix and thus results in a volume increase of the matrix accompanied with a decrease of the cleat volume. The solvation pressure induces additional stress on the sample walls (which positions are fixed in this case study), causing the total stress to increase proportionally to the sum of both the bulk pore pressure and the solvation pressure (the total pore pressure as defined in Chapter 3). Here again, the effective stress principle is verified at all time during the simulation. The effective stress within the cleat rises with increasing alpha values, as illustrated in Figure 56 e-f where the effective stress within the cleat is larger than the effective stress within the matrix when α>0 (the cylinders represent the interparticle forces: the bigger the cylinder diameter is, the higher the effective stress is). This increase in the effective stress within the cleat is primarily due to the stress transfer coming from the swelling of the matrix, which tends to close the cleat.

4.3.3.Permeability evolution

One has to note that we measure the effective permeability of our numerical samples based on Darcy's law by imposing a uniaxial flow with a pressure difference $\Delta p = p_{in} - p_{out}$ across its length:

$$K = -\frac{Q\mu L}{A\Delta p} \tag{4.32}$$

where Q is the volumetric flow rate at equilibrium, A is the cross- sectional area of the sample, and L is the length of the sample (Figure 57).

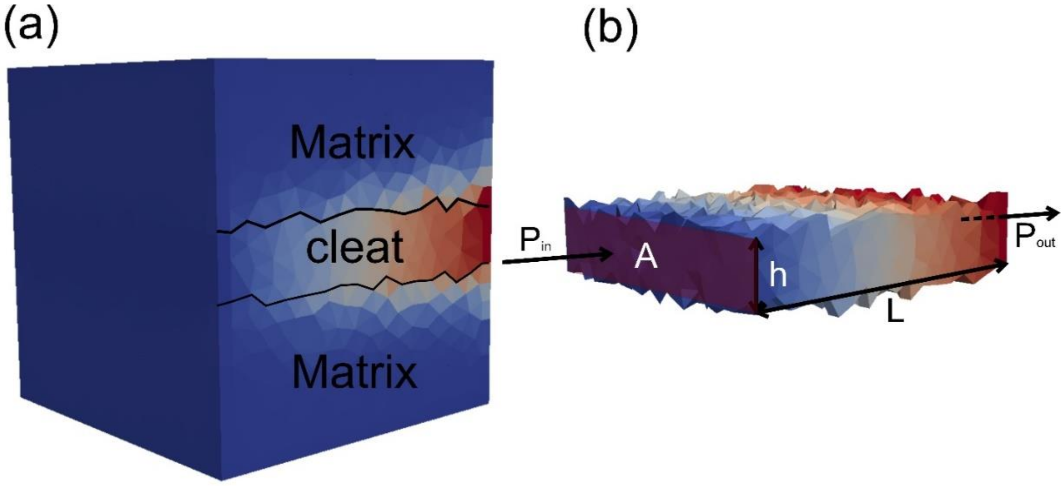

Figure 57 Permeability test simulation: a) coal system representation, b) cleat representation and boundary conditions.

We used the exact same assembly for this study than for the previous study (a 10 x 10 x 10 mm particle assembly made up of 5,000 particles), as well as the same parameters (Table 6, test case 5). As for the previous case studies, the sample boundaries are fixed.

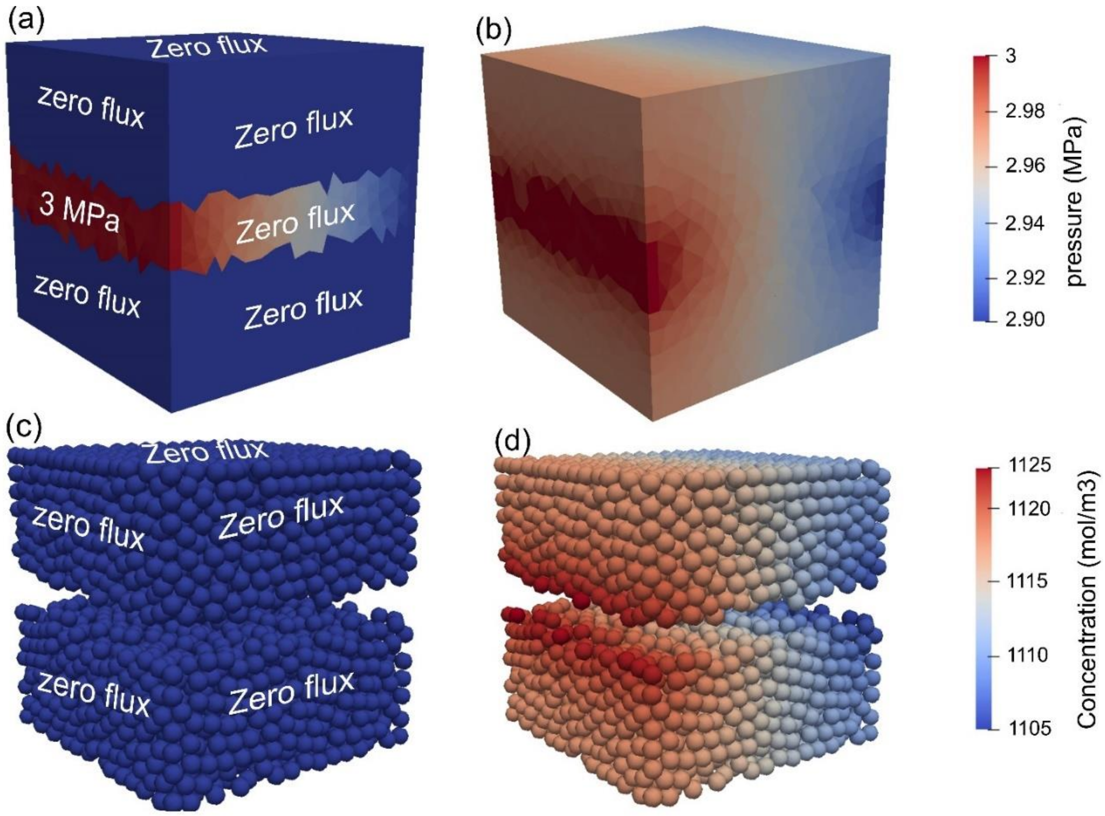

Figure 58 Permeability test simulation for a non-swelling medium: a) initial and boundary conditions for pores (the pressure gradient imposed at t=0 is 0.1 MPa), b) pressure field in pores at t=inf, c) Initial and boundary conditions for particles, d) concentration field for pores at t=inf.

4.3.3.1.Permeability evolution for a non-swelling medium

At first, we present the sample response when swelling does not take place to serve as a reference case.

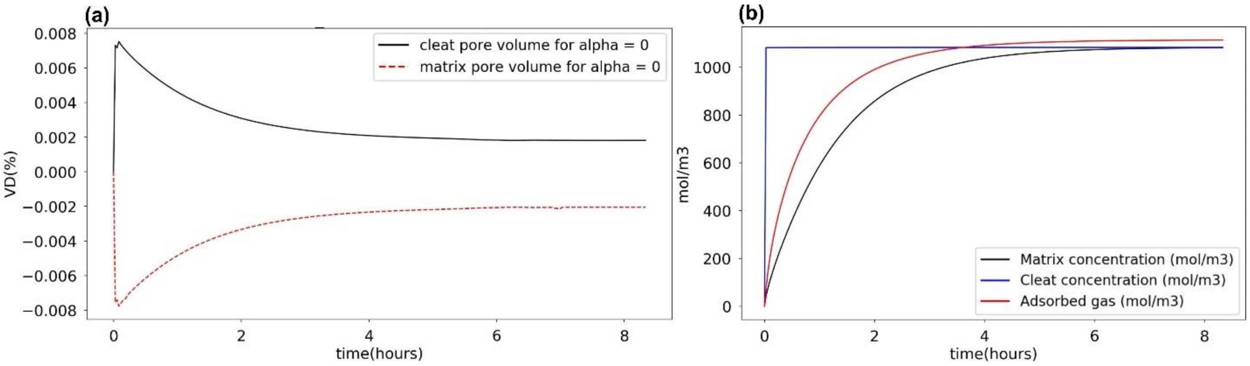

Figure 59 Evolution over time of: a) volumetric deformation of cleat and matrix, b) averaged concentration per region.

As shown in Figure 59a, the cleat instantaneously opens as a result of the imposed pressure jump and, consequently, the matrix compresses. The cleat concentration is instantaneously equilibrated and remains constant due to the imposed advective flow (blue curve in Figure 59b). As gas begins to diffuse into the coal matrix (black curve in Figure 59b), the matrix starts to swell, resulting in a closure of the cleat (Figure 59a). Then, the system reaches equilibrium with gas diffusing everywhere in the system (cleat, pores and particles). At the end of the simulation, gas concentration is homogeneously distributed and both cleat and matrix present an equivalent residual deformation (the cleat has opened while the matrix has shrunk compared to the initial state).

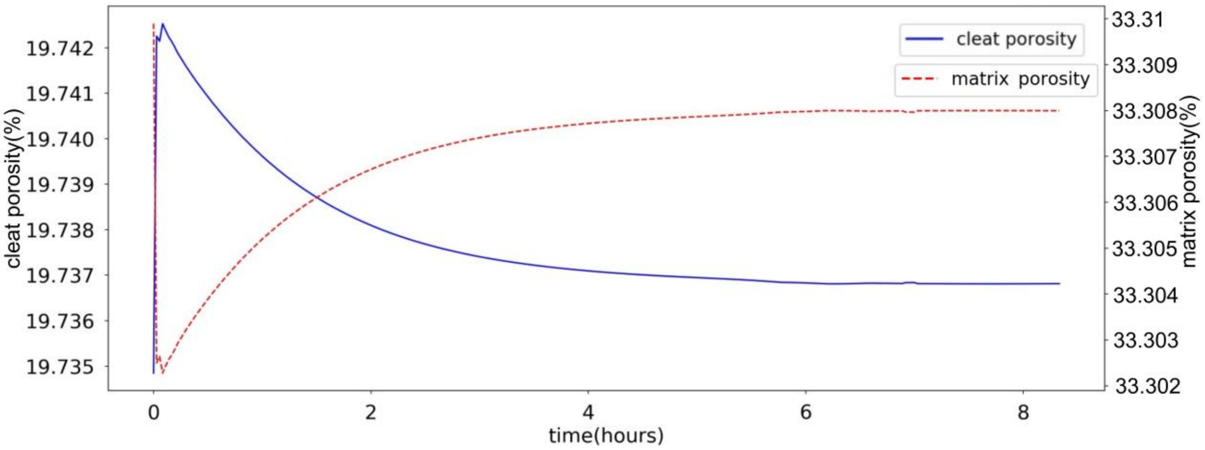

Figure 60 evolution of both cleat and matrix porosities in a non-swelling material.

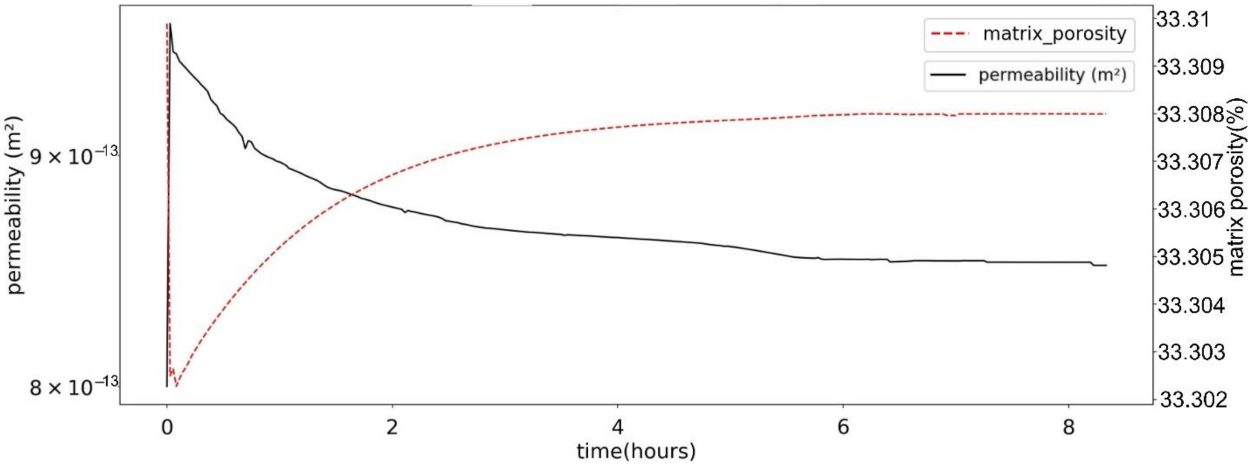

Figure 61 Evolution of permeability and porosity over time for a non-swelling material.

Figure 61 illustrates the dynamic changes of porosity within the matrix and permeability within the cleat. Initially, there is a sharp decline of porosity, followed by a gradual increase, driven by the diffusion of gas throughout the matrix. In parallel, the cleat permeability increases abruptly at the beginning of the simulation (application of the pressure jump) and then closes progressively when the system reaches equilibrium toward the initial value. It is obvious that the permeability changes in Figure 60 follows the cleat porosity evolution.

4.3.3.2.Permeability evolution for a swelling medium

To explore the effect of swelling on permeability changes, we establish two cases with identical initial and boundary conditions, as well as consistent elastic parameters for the non-swelling scenario. The key difference lies in their swelling potential defined by the α value, which we defined equal to 10 and 30 respectively (0 for the non swelling scenario).

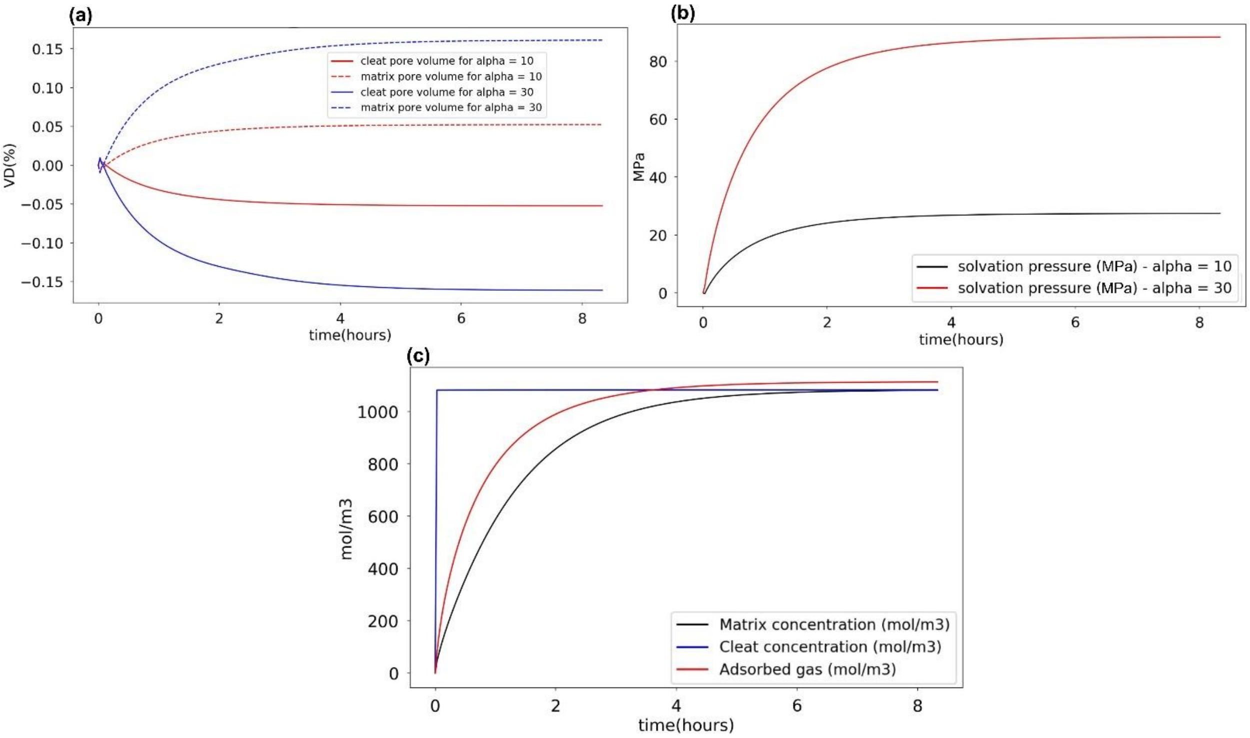

Figure 62 Evolution over time of a) volumetric deformation, b) solvation pressure, c) concentrations within the coal system.

As illustrated in Figure 62a, the application of the pressure gradient across the cleat leads to an instantaneous opening of the cleat accompanied with a matrix shrinkage. However, contrary to the non-swelling case, this trend changes soon after the injection, as a result of the swelling induced by gas diffusion within the matrix. Indeed, the cleat tends to close while the matrix tends to swell as a result of the solvation pressure built up within the matrix (Figure 62b). This sorption induced behavior is proportional to the swelling potential of the material as shown by the larger deformations obtained for the sample with the highest α value. Notably, we observe a more pronounced closure of the cleat and a greater dilatancy of the matrix for α=30 than for α=10.

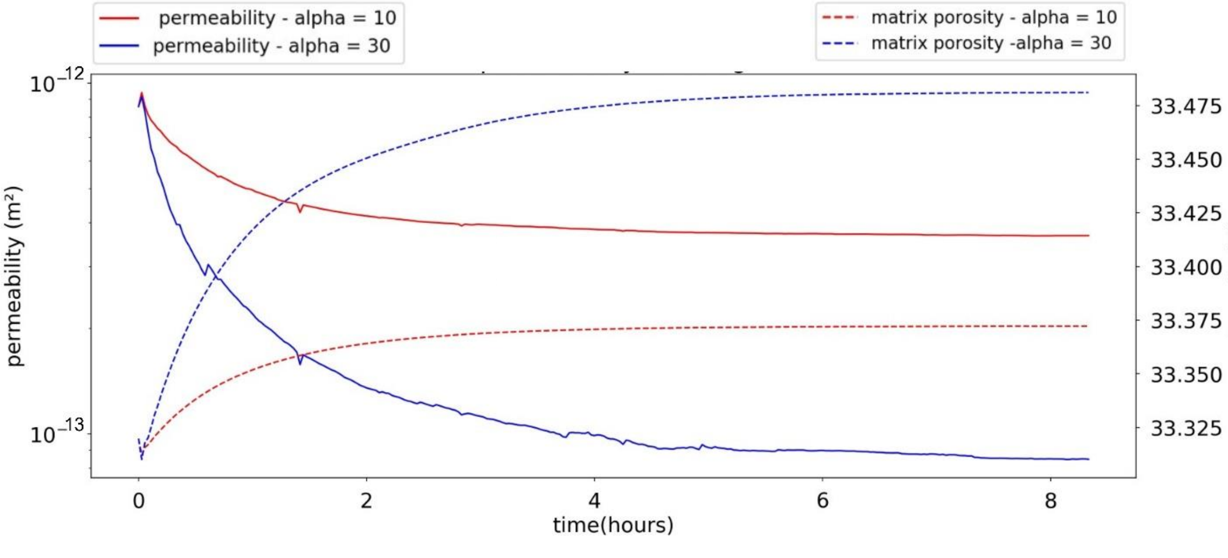

Figure 63 Evolution of permeability and porosity over time for two samples with different swelling potential (α)

Compared to the non-swelling material, sorption induced swelling produces larger changes in terms of permeability and porosity (compare Figure 61 to Figure 63). Actually, the permeability decreases up to one order of magnitude for the material with the highest swelling potential (α=30).

4.3.3.3.Permeability evolution for a swelling medium with a less stiff cleat

In what follows, we study the effect of the cleat stiffness on the permeability evolution by comparing the responses of two samples with identical properties except for the cleat stiffness. In one case, the cleat stiffness is equal to the matrix stiffness while in the other case, the cleat stiffness is ten times smaller than the matrix stiffness.

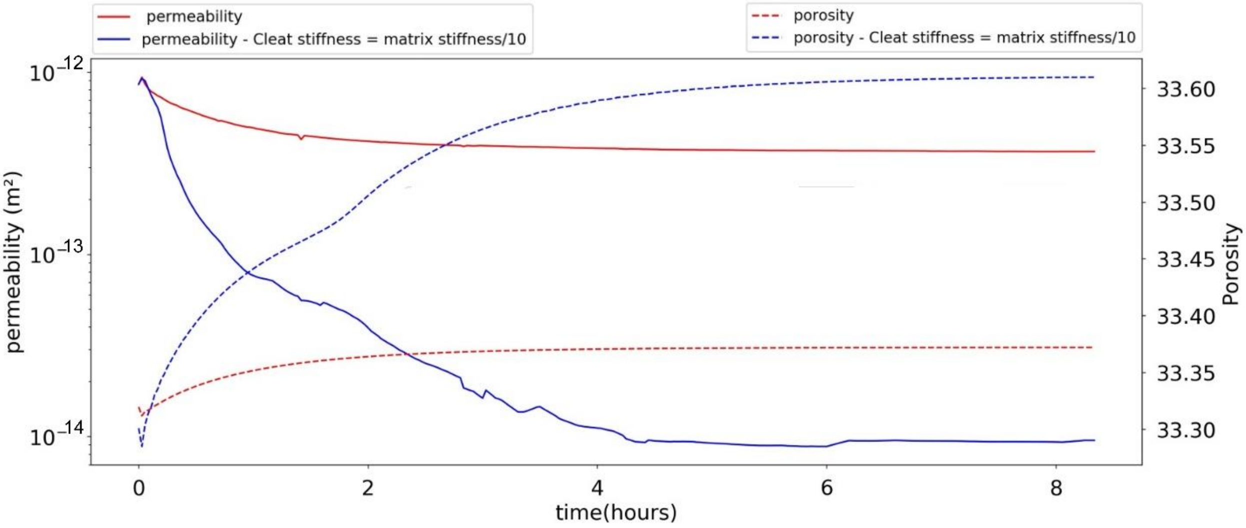

Figure 64 Evolution over time of porosity and permeability for tow samples with different cleat stiffnesses.

As shown in Figure 64, the sample with the less stiff cleat suffers a more pronounced deformation: the cleat closes with more amplitude and, as a result, the matrix porosity expands also more. In the case of the less stiff cleat, porosity increases by 0.3%, while in the sample with the same stiffness for both components, porosity increases by 0.05%. In terms of permeability evolution, the less stiff cleat sample experiences a more substantial decrease compared to the sample with the same cleat stiffness (ca. two orders of magnitude vs. one order of magnitude).

4.4.Conclusion

A 3D single phase pore-scale model for fractured porous swelling materials is proposed to investigate the behavior of coal bed. Specifically, a bonded particle model (BPM) is coupled to the pore scale finite volume scheme (PFV) for describing the transport mechanisms and associated hydromechanical responses within fractured coal. The model is an offspring of our matrix model (Chapter 3) that incorporates cleats in its formulation. The model takes into consideration the various transport mechanisms occurring within the matrix (Knudsen diffusion, surface diffusion and adsorption/desorption), within the cleat (single phase Darcy flow), and between the matrix and the cleat. Its implementation into the YADE DEM platform has been verified by assessing its capability to ensure mass conservation over time in closed systems considering different scenarios (drainage or imbibition), as well as swelling effects.

Finally, the model has been used to evaluate the role of sorption induced swelling on permeability changes for a sample containing a single cleat.

The model was found to be robust and a suitable tool for describing adsorption induced deformation in a fractured sample. This comprehensive investigation reveals the complex physics at stake during methane adsorption and the numerical results give precious insights into the internal dynamics of gas within a coal sample containing a cleat, as well as into the stress and permeability changes induced by sorption processes. Ongoing works aim at considering the presence of several cleats within the system to eventually resemble the topology of cleat networks in coal and extend our analysis. Future works should consider multi-phase flow as well as multi-species gases to better represent the transport processes taking place in coal and the associated hydromechanical responses.

Chapter 5

Conclusion and future work

Chapter 5 : Conclusion and future work

5.1.Conclusion

Coalbeds are highly intricate porous formations, characterized by their heterogeneity, dual porosity, and sensitivity to stress. Understanding the processes involved in coalbed methane (CBM) recovery, carbon dioxide (CO_2) sequestration in coal seams, and enhanced coalbed methane (ECBM) recovery is pivotal for the future both economically and environmentally, and constitutes a complex task that requires the use of adequate numerical models capable of dealing with multiple physics and multiple scales. Hydrogen underground storage in coal seam formations is also a promising option in a full-scale hydrogen economy perspective which will require similar numerical achievements (Keshavarz et al., 2022). While significant progress has been made in developing multi-physics and multi-scale numerical models over the past decades, there is still much room for improvement. Many essential mechanisms remain inadequately accounted for in simulations. One paramount factor among these is the influence of hydromechanical (HM) couplings, as they significantly affect coalbeds permeability and are thus critical for the success of the aforementioned industrial applications. Notably, the permeability of coalbeds is not constant and can undergo drastic changes due to alterations of in-situ conditions, related to stresses and pore pressure variations, as well as to sorption induced swelling/shrinkage associated to fluid flow and transport throughout the medium.

The work presented in this thesis aimed to provide an improved understanding of the coal mechanical response related to gas transport from a pore-scale perspective. For this purpose, we derived a 3D numerical model coupling a discrete element model (DEM) and a pore network model (PNM) specifically developed to describe the different diffusion mechanisms at stake in both coal matrix and cleats, as well as the associated sorption induced deformations. The model is based on the framework of the pore scale finite volume (PFV) scheme implemented in the open-source platform YADE Open DEM. The model is hydromechanically coupled in the sense that changes in pore pressure produce hydrostatic forces that deform the solid skeleton, while deformation of the pore space induces pore pressure changes that promote interpore flow and cleat matrix mass exchange. Sorption induced deformations are taken into account by considering an additional pressure term related to the concentration of gas within the matrix (the so-called solvation pressure). For the sake of simplicity, we have assumed that the cleat network/coal matrix system is initially fully saturated with gas and that the gaseous mixture is only composed of a single specie, considering an ideal gas assumption and the fact that a part of it can be sorbed onto the solid phase. In addition, coal matrix permeability is neglected, and advection only occurs within the cleats. Specifically, the following objectives have been achieved:

- Matrix
    - We developed a hydromechanically coupled numerical model that obeys the poromechanics of swelling materials (elastically at least!).
    - We implemented and validated the various transport mechanisms that take place within the coal matrix at the scale we are dealing with such as Knudsen diffusion, surface diffusion, and adsorption/desorption mechanisms.

  - Our numerical model reproduces the evolution of porosity, volumetric deformation, solvation pressure, concentration field, pore pressure in the coal matrix due to injection/dejection of gas in the coal matrix.
  - We successfully compared our model's predictions to experimental results from the literature.

- Cleats
  - We developed and implemented the mechanical and hydraulic couplings taking place between cleats and coal matrix in our numerical model.
  - We validated the implementation of the transport processes by verifying mass conservation in a closed system subjected to different loading paths. These transport processes include advection within the cleats, Knudsen diffusion and adsorption/desorption between the cleats and the matrix, as well as Knudsen diffusion, surface diffusion and adsorption/desorption within the matrix.
  - We studied the evolution of stresses related to sorption induced deformation and pore pressure variation within a fractured sample.
  - Our numerical model, even though limited to a sample containing a single cleat, reproduces the changes of permeability and porosity that takes place in coaldbeds when sorption induced deformations occur within the coal matrix.

Our work constitutes a first step toward a comprehensive understanding of the extremely complex processes that take place within a fractured coal system. Our model is capable to describe the strong coupling between transport, chemical (sorption) and mechanical processes that take place in coalbeds and could eventually be extended to predict CBM recovery in fractured coalbeds and assess the associated permeability changes at the reservoir scale.

5.2.Recommendations for future works

While acknowledging the time limitations, it is important to recognize that there is room for enhancing our numerical model. We aimed to capture the most crucial phenomena with its current status but, obviously, many elements could be added to improve its relevance and capability. Here, I want to share my suggestions on what should/could be integrated into the model:

- **Coal matrix shrinkage/swelling and gas desorption/adsorption in the presence of multi-component gaseous phase**.

How multiple gaseous species (CH_4, CO_2, H_2…) compete for adsorption on coal matrix (especially when adsorption sites are limited) and how gas components influence the deformation are not fully understood, especially under in situ stress conditions. However, from a numerical point of view, the model is already developed for single species which may ease the additions of multiple species by doing a parallel work to the model. Moreover, an experimental work run in parallel by my colleague (with Regalor team) which will help us to more validate our numerical result related to multispecies and its hydro-mechanical response (Amoih et al., 2022).

- **Multiphase flow through the cleat system**

Relative permeability curves play a vital role in simulating both Coalbed Methane (CBM) and Enhanced Coalbed Methane (ECBM) processes. In many coalbeds, the cleats at larger scales are initially filled with water (brine), giving rise to multiphase flow conditions. In addition, moisture remains in coal matrix and may thus influence both gas diffusion and sorption capacity (Harpalani and Zhao, 1989; Pan et al., 2010). Moreover, the effective stress within multiphase flow conditions is still not fully understood. It is usual to assume the concept of equivalent pressure (Coussy, 2004) but the appropriate form of the effective stress equation for a multiphase system is still an active domain of research (Gray and Schrefler, 2001).

A master's student, Gouy Augustin, has dedicated six months of its Master thesis to develop a PNM model for simulating multiphase flow through coal cleat networks (Figure 65). Moreover, the YADE DEM platform already incorporates an engine tailored for simulating multiphase flow within porous media (Sweijen et al., 2017; Yuan and Chareyre, 2017). Given these existing resources and developments, the creation of a numerical model for simulating multiphase flow within the cleat system should be a manageable task.

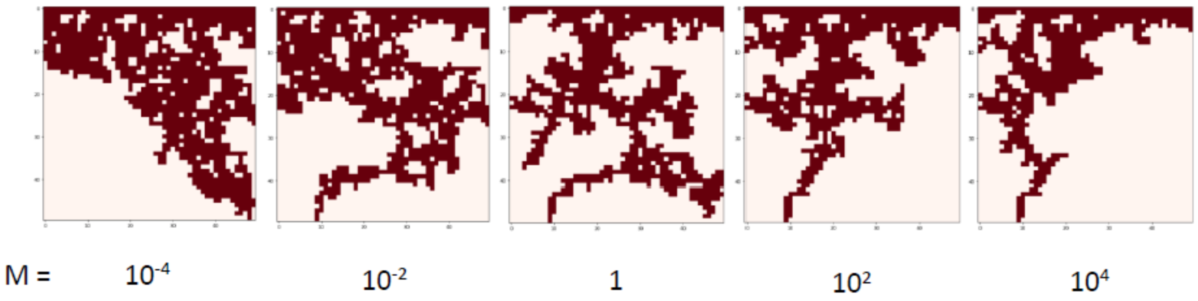

Figure 65. Gas invasion patterns within a porous medium after breakthrough simulated using a PNM model for different mobility ratios (Gouy et al., 2021)

- **Dual permeability system**

For some types of coal, the assumption of negligible coal matrix permeability can be somewhat irrelevant. It could be of interest to consider permeability in the coal matrix to have more accurate results about competition between transport mechanisms which may affect in return the evolution history of mechanical parameters such as the averaged permeability, porosity, stresses, etc.

- **Discrete fracture network**

Coal is a dual porosity system that consist of a coal matrix surrounded by a network of cleats which makes the structure of coalbeds very complex. Digital images of fractured coal samples obtained by X-ray tomography (see an example in Figure 66), or at the lower scale by FIB-SEM (Focused Ion Beam Scanning Electron Microscope) or Transmission Electron Microscopy (TEM) (Mostaghimi et al., 2016), provide the opportunity to construct relevant coal structures through 3D digitalized representations (Figure 66). A DEM-PFV coupled to a fracture network model such as the DEM-DFN model proposed by (Scholtès et al., 2011) (Figure 28) would render possible to simulate the HM behavior of such structures.

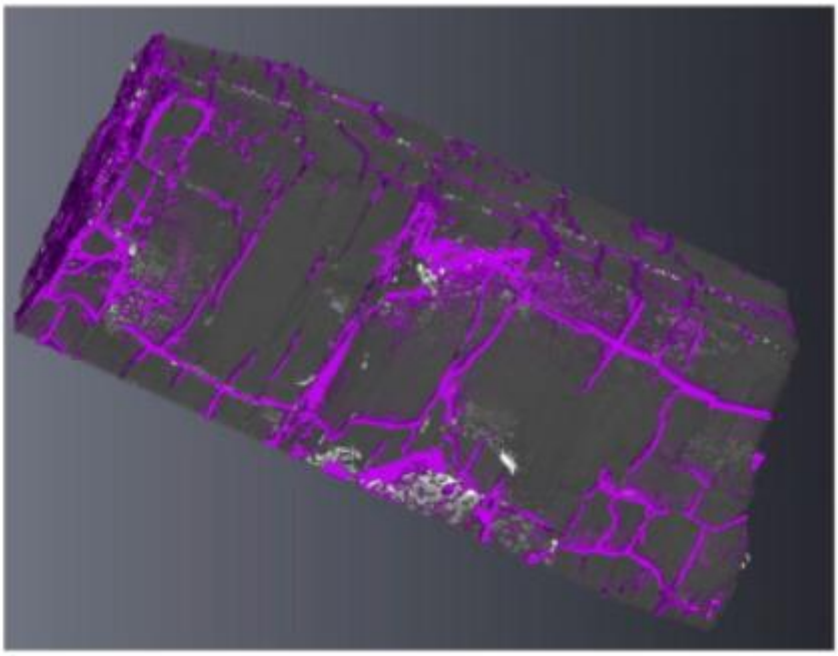

Figure 66 X-ray computed tomography reconstruction of a subbituminous coal lump (left hand side) showing the existing cleat network (Mathews et al., 2011)

- **taking into account plasticity/damage/fracturing**:

All our simulations were run in the elastic regime. However, DEM models such as the BPM used in this study have the capability to explicitly deal with the nucleation, propagation and coalescence of cracks/fractures within rock like materials (Scholtès and Donzé, 2012). Extending our model so that the PFV scheme would enable the simulation of progressive fracturing similarly to the DEM-PFV model proposed by (Figure 67, (Papachristos, 2017)) to study hydraulic fracturing process would then open up possibilities to deal with damage and rupture processes that take place in coalbeds.

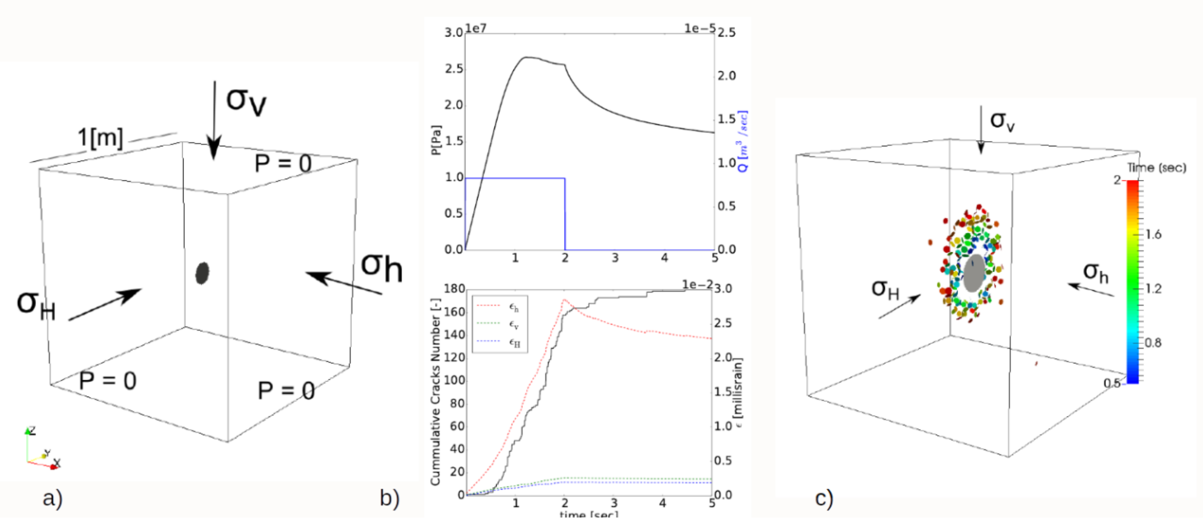

Figure 67 Simulation of an hydraulic fracturing test in an intact DEM-PFV model by (Papachristos, 2017): a) initial and boundary conditions, b) evolution over time of imposed and measured parameters, c) representation of the fracturing pattern at t=2.5 s.

- **Upscaling properties at the core or the field scale**

Part of the difficulty when using continuum models is to evaluate the effective properties (e.g., apparent adsorption rate, Biot coefficient, permeability) and determine their evolution. Indeed, these properties may evolve in a complex way due to their dependency to pore-scale properties and change of pore space architecture with time. An alternative of using heuristic formulations (e.g., Kozeny-Carman law) relies upon pore-scale simulations. This is the aim of the so-called Digital Rock Physics (DRP) approach based on the use of high resolution digital images of rocks so that the material properties are evaluated numerically at the pore scale (Tinet et al., 2020). As a consequence, the ultimate objective of this work is to explore the capability of the DEM-PFV approach to predict the macroscopic transport properties of coal and confront them to experimental data or in situ measurement. A first attempt have been achieved in **Chapter 4** to predict for instance the evolution of coal permeability but it should be extended to more complex and realistic geometries and for any effective property.

In combination with the investigation for defining the organization of structural blocks in the coalfield and for understanding the fracturing process (PhD thesis of Regalor Project; (Allouti et al., 2023), such result could be used in 3D geomechanical simulations for better risk assessment analysis of induced seismicity during CBM exploitation for instance (postdoctoral work funded by Regalor project; Modeste et al., 2022).

Chapter 6

References

Chapter 6 : References

Al-Jubori, A., Johnston, S., Boyer, C., Lambert, S.W., Bustos, O.A., Pashin, J.C., Wray, A., 2009. Coalbed Methane: Clean Energy for the World. Oilfield Rev.

Allouti, S., Michels, R., Malartre, F., Mouketo, M.M., Geraud, Y., Nassif, F., Pironon, J., Donato, P.D., 2023. The Lorraine Carboniferous Basin (France) as a New Target of Regional Gas Resource for the Energy Transition Strategy? Presented at the IMOG 2023, European Association of Geoscientists & Engineers, pp. 1–2. https://doi.org/10.3997/2214-4609.202333136

Amoih, F.A.K., Finqueneisel, G., Zimny, T., Bourrelly, S., Grgic, D., 2022. Characterization of Different Coal Seams for Co2-Ecbm by Comparison of Data from Sorption Isotherms, Breakthrough Curves and Thermogravimetric Analyzes. https://doi.org/10.2139/ssrn.4298724

Anggara, F., Sasaki, K., Rodrigues, S., Sugai, Y., 2014. The effect of megascopic texture on swelling of a low rank coal in supercritical carbon dioxide. Int. J. Coal Geol. 125, 45–56. https://doi.org/10.1016/j.coal.2014.02.004

Asnin, L.D., Fedorov, A.A., Chekryshkin, Yu.S., 2001. Thermodynamic parameters of adsorption described by the logarithmic Temkin isotherm. Russ. Chem. Bull. 50, 217–219. https://doi.org/10.1023/A:1009509813738

Australia, c\=AU\;o\=Australia G., 2014. Coalbed Methane [WWW Document]. URL https://www.ga.gov.au/data-pubs/data-and-publications-search/publications/oil-gas-resources-australia/2005/coalbed-methane (accessed 2.14.23).

Ayers, W.B., Jr., 2002. Coalbed Gas Systems, Resources, and Production and a Review of Contrasting Cases from the San Juan and Powder River Basins. AAPG Bull. 86, 1853–1890. https://doi.org/10.1306/61EEDDAA-173E-11D7-8645000102C1865D

Balucan, R.D., Turner, L.G., Steel, K.M., 2018. X-ray μCT investigations of the effects of cleat demineralization by HCl acidizing on coal permeability. J. Nat. Gas Sci. Eng. 55, 206–218. https://doi.org/10.1016/j.jngse.2018.05.007

Bertrand, F., Cerfontaine, B., Collin, F., 2017. A fully coupled hydro-mechanical model for the modeling of coalbed methane recovery. J. Nat. Gas Sci. Eng. 46, 307–325. https://doi.org/10.1016/j.jngse.2017.07.029

Biot, M.A., 1941. General Theory of Three-Dimensional Consolidation. J. Appl. Phys. 12, 155–164. https://doi.org/10.1063/1.1712886

Bird, R.B., Stewart, W.E., Lightfoot, E.N., 2002. Transport phenomena, 2nd, Wiley international ed ed. J. Wiley, New York.

Blunt, M.J., 2001. Flow in porous media — pore-network models and multiphase flow. Curr. Opin. Colloid Interface Sci. 6, 197–207. https://doi.org/10.1016/S1359-0294(01)00084-X

Brochard, L., FEN-CHONG, T., PELLENQ, R., 2011. Poromécanique et adsorption : Application au gonflement du charbon lors du stockage géologique du carbone.

Brochard, L., Vandamme, M., Pellenq, R.J.-M., 2012. Poromechanics of microporous media. J. Mech. Phys. Solids 60, 606–622. https://doi.org/10.1016/j.jmps.2012.01.001

Bustin, R.M., Clarkson, C.R., 1998. Geological controls on coalbed methane reservoir capacity and gas content. Int. J. Coal Geol. 38, 3–26. https://doi.org/10.1016/S0166-5162(98)00030-5

Catalano, E., Chareyre, B., Barthélémy, E., 2014. Pore-scale modeling of fluid-particles interaction and emerging poromechanical effects. Int. J. Numer. Anal. Methods Geomech. 38, 51–71. https://doi.org/10.1002/nag.2198

Caulk, R., Scholtès, L., Krzaczek, M., Chareyre, B., 2020. A pore-scale thermo–hydro-mechanical model for particulate systems. Comput. Methods Appl. Mech. Eng. 372, 113292. https://doi.org/10.1016/j.cma.2020.113292

Ceglarska-Stefańska, G., Brzóska, K., 1998. The effect of coal metamorphism on methane desorption. Fuel, Presented at the Third Symposium on Coal Structure, 1996 77, 645–648. https://doi.org/10.1016/S0016-2361(97)00177-4

Ceglarska-Stefańska, G., Czapliński, A., 1993. Correlation between sorption and dilatometric processes in hard coals. Fuel 72, 413–417. https://doi.org/10.1016/0016-2361(93)90064-9

Ceglarska-Stefańska, G., Zarębska, K., 2002. The competitive sorption of CO2 and CH4 with regard to the release of methane from coal. Fuel Process. Technol. 77–78, 423–429. https://doi.org/10.1016/S0378-3820(02)00093-0

Chareyre, B., Cortis, A., Catalano, E., Barthélemy, E., 2012. Pore-Scale Modeling of Viscous Flow and Induced Forces in Dense Sphere Packings. Transp. Porous Media 94, 595–615. https://doi.org/10.1007/s11242-012-0057-2

Chen, M., Hosking, L.J., Sandford, R.J., Thomas, H.R., 2019a. Dual porosity modelling of the coupled mechanical response of coal to gas flow and adsorption. Int. J. Coal Geol. 205, 115–125. https://doi.org/10.1016/j.coal.2019.01.009

Chen, M., Hosking, L.J., Sandford, R.J., Thomas, H.R., 2019b. Dual porosity modelling of the coupled mechanical response of coal to gas flow and adsorption. Int. J. Coal Geol. 205, 115–125. https://doi.org/10.1016/j.coal.2019.01.009

Chen, M., Masum, S.A., Thomas, H.R., 2022a. 3D hybrid coupled dual continuum and discrete fracture model for simulation of CO2 injection into stimulated coal reservoirs with parallel implementation. Int. J. Coal Geol. 262, 104103. https://doi.org/10.1016/j.coal.2022.104103

Chen, M., Masum, S.A., Thomas, H.R., 2022b. 3D hybrid coupled dual continuum and discrete fracture model for simulation of CO2 injection into stimulated coal reservoirs with parallel implementation. Int. J. Coal Geol. 262, 104103. https://doi.org/10.1016/j.coal.2022.104103

Chikatamarla, L., Cui, X., Bustin, R.M., 2004. IMPLICATIONS OF VOLUMETRIC SWELLING/SHRINKAGE OF COAL IN SEQUESTRATION OF ACID GASES.

Choi, J.-G., Do, D.D., Do, H.D., 2001. Surface Diffusion of Adsorbed Molecules in Porous Media: Monolayer, Multilayer, and Capillary Condensation Regimes. Ind. Eng. Chem. Res. 40, 4005–4031. https://doi.org/10.1021/ie010195z

Connell, L.D., 2016. A new interpretation of the response of coal permeability to changes in pore pressure, stress and matrix shrinkage. Int. J. Coal Geol. 162, 169–182. https://doi.org/10.1016/j.coal.2016.06.012

Coussy, O., 2004. Poromechanics. John Wiley & Sons.

Cundall, P.A., Strack, O.D.L., 1979. A discrete numerical model for granular assemblies. Géotechnique 29, 47–65. https://doi.org/10.1680/geot.1979.29.1.47

Dabbous, M.K., Reznik, A.A., Taber, J.J., Fulton, P.F., 1974. The Permeability of Coal to Gas and Water. Soc. Pet. Eng. J. 14, 563–572. https://doi.org/10.2118/4711-A

Dai, S., Ren, D., Chou, C.-L., Li, S., Jiang, Y., 2006. Mineralogy and geochemistry of the No. 6 Coal (Pennsylvanian) in the Junger Coalfield, Ordos Basin, China. Int. J. Coal Geol. 66, 253–270. https://doi.org/10.1016/j.coal.2005.08.003

Daniels, E.J., Marshak, S., Altaner, S.P., 1996. Use of clay-mineral alteration patterns to define syntectonic permeability of joints (cleat) in Pennsylvania anthracite coal. Tectonophysics 263, 123–136. https://doi.org/10.1016/S0040-1951(96)00019-4

Darcy, H., 1865. ptie. Recherches expérimentales sur l'écoulement de l'eau dans les canaux découverts. Imprimerie Nationale.

Dawson, G.K.W., Esterle, J.S., 2010. Controls on coal cleat spacing. Int. J. Coal Geol., Asia Pacific Coalbed Methane Symposium: Selected papers from the 2008 Brisbane symposium on coalbed methane and CO-enhanced coalbed methane 82, 213–218. https://doi.org/10.1016/j.coal.2009.10.004

Dawson, G.K.W., Golding, S.D., Esterle, J.S., Massarotto, P., 2012. Occurrence of minerals within fractures and matrix of selected Bowen and Ruhr Basin coals. Int. J. Coal Geol., Minerals and Trace Elements in Coal 94, 150–166. https://doi.org/10.1016/j.coal.2012.01.004

Day, S., Duffy, G., Sakurovs, R., Weir, S., 2008b. Effect of coal properties on CO2 sorption capacity under supercritical conditions. Int. J. Greenh. Gas Control, EGU General Assembly 2007: Advances in CO2 Storage in Geological Systems 2, 342–352. https://doi.org/10.1016/S1750-5836(07)00120-X

Day, S., Fry, R., Sakurovs, R., 2008a. Swelling of Australian coals in supercritical CO2. Int. J. Coal Geol. 74, 41–52. https://doi.org/10.1016/j.coal.2007.09.006

Deng, C., Tang, D., Liu, S., Xu, H., Tao, S., 2015. Characterization of mineral composition and its influence on microstructure and sorption capacity of coal. J. Nat. Gas Sci. Eng. 25, 46–57. https://doi.org/10.1016/j.jngse.2015.04.034

Detournay, E., Cheng, A.H.-D., 1993. 5 - Fundamentals of Poroelasticity, in: Fairhurst, C. (Ed.), Analysis and Design Methods. Pergamon, Oxford, pp. 113–171. https://doi.org/10.1016/B978-0-08-040615-2.50011-3

Diessel, C.F.K., 1992. Introduction, in: Diessel, C.F.K. (Ed.), Coal-Bearing Depositional Systems. Springer, Berlin, Heidelberg, pp. 1–4. https://doi.org/10.1007/978-3-642-75668-9_1

Dindarloo, S.R., Bagherieh, A., Hower, J.C., Calder, J.H., Wagner, N.J., 2015. Coal modeling using Markov Chain and Monte Carlo simulation: Analysis of microlithotype and lithotype succession. Sediment. Geol. 329, 1–11. https://doi.org/10.1016/j.sedgeo.2015.08.005

Do, D.D., 1998. Adsorption Analysis: Equilibria And Kinetics (With Cd Containing Computer Matlab Programs). World Scientific.

Dolino, G., Bellet, D., Faivre, C., 1996. Adsorption strains in porous silicon. Phys. Rev. B 54, 17919–17929. https://doi.org/10.1103/PhysRevB.54.17919

Dong, J., Cheng, Y., Liu, Q., Zhang, H., Zhang, K., Hu, B., 2017. Apparent and True Diffusion Coefficients of Methane in Coal and Their Relationships with Methane Desorption Capacity. Energy Fuels 31, 2643–2651. https://doi.org/10.1021/acs.energyfuels.6b03214

Duriez, J., Scholtès, L., Donzé, F.-V., 2016. Micromechanics of wing crack propagation for different flaw properties. Eng. Fract. Mech. 153, 378–398. https://doi.org/10.1016/j.engfracmech.2015.12.034

Durucan, S., Ahsanb, M., Shia, J.-Q., 2009. Matrix shrinkage and swelling characteristics of European coals. Energy Procedia, Greenhouse Gas Control Technologies 9 1, 3055–3062. https://doi.org/10.1016/j.egypro.2009.02.084

Dutcher, R., 1978. Field Description of Coal. ASTM International.

Eaton, T.T., 2013. Science-based decision-making on complex issues: Marcellus shale gas hydrofracking and New York City water supply. Sci. Total Environ. 461–462, 158–169. https://doi.org/10.1016/j.scitotenv.2013.04.093

Espinoza, D.N., Vandamme, M., Dangla, P., Pereira, J.-M., Vidal-Gilbert, S., 2013. A transverse isotropic model for microporous solids: Application to coal matrix adsorption and swelling. J. Geophys. Res. Solid Earth 118, 6113–6123. https://doi.org/10.1002/2013JB010337

Espinoza, D.N., Vandamme, M., Pereira, J.-M., Dangla, P., Vidal-Gilbert, S., 2014. Measurement and modeling of adsorptive–poromechanical properties of bituminous coal cores exposed to CO2: Adsorption, swelling strains, swelling stresses and impact on fracture permeability. Int. J. Coal Geol. 134–135, 80–95. https://doi.org/10.1016/j.coal.2014.09.010

Esterle, J.S., Kolatschek, Y., O'Brien, G., 2002. Relationship between in situ coal stratigraphy and particle size and composition after breakage in bituminous coals. Int. J. Coal Geol., John C. Ferm - Contributions to Coal Geology 49, 195–214. https://doi.org/10.1016/S0166-5162(01)00077-5

Esterle, J.S., O`Brien, G., Kojovic, T., 1994. Influence of coal texture and rank on breakage energy and resulting size distributions in Australian coals.

Ewen, C., Borchardt, D., Richter, S., Hammerbacher, R., 2012. Hydrofracking Risk Assessment: Study concerning the safety and environmental compatibility of hydrofracking for natural gas production from unconventional reservoirs.

Faiz, M., Hendry, P., 2006. Significance of microbial activity in Australian coal bed methane reservoirs — a review. Bull. Can. Pet. Geol. 54, 261–272. https://doi.org/10.2113/gscpgbull.54.3.261

Fatt, I., 1956. The Network Model of Porous Media. Trans. AIME 207, 144–181. https://doi.org/10.2118/574-G

Fick, A., 1855. Ueber Diffusion. Ann. Phys. 170, 59–86. https://doi.org/10.1002/andp.18551700105

Flores, R.M., 2013. Coal and Coalbed Gas: Fueling the Future. Newnes.

Freij-Ayoub, R., 2012. Opportunities and challenges to coal bed methane production in Australia. J. Pet. Sci. Eng., Unconventional hydrocarbons exploration and production Challenges 88–89, 1–4. https://doi.org/10.1016/j.petrol.2012.05.001

Furfari, S., 2017. The Myth of a Fossil Fuel Phase-Out | by Samuele Furfari [WWW Document]. Proj. Synd. URL https://www.project-syndicate.org/commentary/climate-change-fossil-fuels-continued-reliance-by-samuele-furfari-2017-12 (accessed 2.7.23).

Fuyuan Mu, Zhong Weizh, Zhao Xianliang, Che Changbo, Chen Yanpeng, Zhu Jie, Wang Bo, 2015. Strategies for the development of CBM gas industry in China | Elsevier Enhanced Reader. https://doi.org/10.1016/j.ngib.2015.09.013

Gamson, P.D., Beamish, B.B., 1992. Coal type, microstructure and gas flow behaviour of Bowen Basin coals, in: Symposium on Coalbed Methane Research and Development in Australia, Beamish, BB and Gamson, PD (Eds.), James Cook University of North Queensland. pp. 43–66.

Gamson, P.D., Beamish, B.B., Johnson, D.P., 1993. Coal microstructure and micropermeability and their effects on natural gas recovery. Fuel 72, 87–99. https://doi.org/10.1016/0016-2361(93)90381-B

Gan, H., Nandi, S.P., Walker, P.L., 1972. Nature of the porosity in American coals. Fuel 51, 272–277. https://doi.org/10.1016/0016-2361(72)90003-8

Gor, G.Yu., Neimark, A.V., 2010. Adsorption-Induced Deformation of Mesoporous Solids. Langmuir 26, 13021–13027. https://doi.org/10.1021/la1019247

Gray, I., 1987. Reservoir Engineering in Coal Seams: Part 1—The Physical Process of Gas Storage and Movement in Coal Seams. SPE Reserv. Eng. 2, 28–34. https://doi.org/10.2118/12514-PA

Gray, W.G., Schrefler, B.A., 2001. Thermodynamic approach to effective stress in partially saturated porous media. Eur. J. Mech. - ASolids 20, 521–538. https://doi.org/10.1016/S0997-7538(01)01158-5

Grosman, A., Ortega, C., 2008. Influence of elastic deformation of porous materials in adsorption-desorption process: A thermodynamic approach. Phys. Rev. B 78, 085433. https://doi.org/10.1103/PhysRevB.78.085433

Guo, X., Wang, Z., Zhao, Y., 2016. A comprehensive model for the prediction of coal swelling induced by methane and carbon dioxide adsorption. J. Nat. Gas Sci. Eng. 36, 563–572. https://doi.org/10.1016/j.jngse.2016.10.052

Hall, F.E., Zhou, C., Gasem, K. a. M., Robinson, R.L., Yee, D., 1994. Adsorption of Pure Methane, Nitrogen, and Carbon Dioxide and Their Binary Mixtures on Wet Fruitland Coal. Presented at the SPE Eastern Regional Meeting, OnePetro. https://doi.org/10.2118/29194-MS

Harpalani, Pariti, 1993. Study of coal sorption isotherms using a multicomponent gas mixture. In Proceedings of the International Coalbed Methane Symposium, Birmingham, Alabama, May 17–21.

Harpalani, S., Chen, G., 1997. Influence of gas production induced volumetric strain on permeability of coal. Geotech. Geol. Eng. 15, 303–325. https://doi.org/10.1007/BF00880711

Harpalani, S., Chen, G., 1995. Estimation of changes in fracture porosity of coal with gas emission. Fuel 74, 1491–1498. https://doi.org/10.1016/0016-2361(95)00106-F

Harpalani, S., Schraufnagel, A., 1990. Measurement of parameters impacting methane recovery from coal seams. Int. J. Min. Geol. Eng. 8, 369–384. https://doi.org/10.1007/BF00920648

Harpalani, S., Schraufnagel, R.A., 1990a. Shrinkage of coal matrix with release of gas and its impact on permeability of coal. Fuel 69, 551–556. https://doi.org/10.1016/0016-2361(90)90137-F

Harpalani, S., Schraufnagel, R.A., 1990b. Influence of Matrix Shrinkage and Compressibility on Gas Production From Coalbed Methane Reservoirs. Presented at the SPE Annual Technical Conference and Exhibition, OnePetro. https://doi.org/10.2118/20729-MS

Harpalani, S., Zhao, X., 1989. An investigation of the effect of gas desorption on coal permeability formation. Proc Coalbed Methane Symp Tuscaloosa Ala.

Harthong, B., Scholtès, L., Donzé, F.-V., 2012. Strength characterization of rock masses, using a coupled DEM–DFN model. Geophys. J. Int. 191, 467–480. https://doi.org/10.1111/j.1365-246X.2012.05642.x

Huddleston, Marshall, J.S., Pilcher, R.C., 1995. Analysis of Sorption and Thermodynamic Data and a Discussion of an Empirical Model for Sorbed Gases in Coal. (No. CONF-950572-). Alabama Univ., University, AL (United States); Gas Research Inst., Chicago, IL (United States); Environmental Protection Agency, Washington, DC (United States); Mine Safety and Health Administration, Arlington, VA (United States); Alabama Geological Survey, University, AL (United States); US Department of Energy (USDOE), Washington DC (United States).

Izart, A., Barbarand, J., Michels, R., Privalov, V.A., 2016. Modelling of the thermal history of the Carboniferous Lorraine Coal Basin: Consequences for coal bed methane. Int. J. Coal Geol. 168, 253–274. https://doi.org/10.1016/j.coal.2016.11.008

Jing, L., Ma, Y., Fang, Z., 2001. Modeling of fluid flow and solid deformation for fractured rocks with discontinuous deformation analysis (DDA) method. Int. J. Rock Mech. Min. Sci. 38, 343–355. https://doi.org/10.1016/S1365-1609(01)00005-3

Jing, Y., 2017. Pore-scale Characterisation of Fractured Coal (Thesis). UNSW Sydney. https://doi.org/10.26190/unsworks/20109

Jing, Y., Armstrong, R.T., Mostaghimi, P., 2017a. Digital coal: Generation of fractured cores with microscale features. Fuel 207, 93–101. https://doi.org/10.1016/j.fuel.2017.06.051

Jing, Y., Armstrong, R.T., Ramandi, H.L., Mostaghimi, P., 2017b. Topological Characterization of Fractured Coal. J. Geophys. Res. Solid Earth 122, 9849–9861. https://doi.org/10.1002/2017JB014667

Joekar-Niasar, V., Hassanizadeh, S.M., 2012. Analysis of Fundamentals of Two-Phase Flow in Porous Media Using Dynamic Pore-Network Models: A Review. Crit. Rev. Environ. Sci. Technol. 42, 1895–1976. https://doi.org/10.1080/10643389.2011.574101

Kainourgiakis, M.E., Kikkinides, E.S., Stubos, A.K., Kanellopoulos, N.K., 1998. Adsorption–desorption gas relative permeability through mesoporous media—network modelling and percolation theory. Chem. Eng. Sci. 53, 2353–2364. https://doi.org/10.1016/S0009-2509(98)00084-0

Kendall, P.F., Briggs, H., 1934. XIII.—The Formation of Rock Joints and the Cleat of Coal. Proc. R. Soc. Edinb. 53, 164–187. https://doi.org/10.1017/S037016460001556X

Keshavarz, A., Abid, H., Ali, M., Iglauer, S., 2022. Hydrogen diffusion in coal: Implications for hydrogen geo-storage. J. Colloid Interface Sci. 608, 1457–1462. https://doi.org/10.1016/j.jcis.2021.10.050

Kowalczyk, P., Ciach, A., Neimark, A.V., 2008. Adsorption-Induced Deformation of Microporous Carbons: Pore Size Distribution Effect. Langmuir 24, 6603–6608. https://doi.org/10.1021/la800406c

Lanetc, Z., Zhuravljov, A., Armstrong, R.T., Mostaghimi, P., 2023a. Hybrid numerical methods for modelling multi-physics mass transport in coal. Int. J. Heat Mass Transf. 214, 124386. https://doi.org/10.1016/j.ijheatmasstransfer.2023.124386

Lanetc, Z., Zhuravljov, A., Tang, K., Armstrong, R.T., Mostaghimi, P., 2023b. Multi-scale modelling of multi-physics flow in coal seams. Gas Sci. Eng. 118, 205081. https://doi.org/10.1016/j.jgsce.2023.205081

Laubach, S.E., Marrett, R.A., Olson, J.E., Scott, A.R., 1998. Characteristics and origins of coal cleat: A review. Int. J. Coal Geol. 35, 175–207. https://doi.org/10.1016/S0166-5162(97)00012-8

Levine, J.R., 1996a. Model study of the influence of matrix shrinkage on absolute permeability of coal bed reservoirs. Geol. Soc. Lond. Spec. Publ. 109, 197–212. https://doi.org/10.1144/GSL.SP.1996.109.01.14

Levine, J.R., 1996b. Model study of the influence of matrix shrinkage on absolute permeability of coal bed reservoirs. Geol. Soc. Lond. Spec. Publ. 109, 197–212. https://doi.org/10.1144/GSL.SP.1996.109.01.14

Li, W., Yang, K., Deng, D., Zhao, C., Yang, S., Cheng, Y., Lu, S., 2023. A lattice Boltzmann model for simulating gas transport in coal nanopores considering surface adsorption and diffusion effects. Fuel 340, 127507. https://doi.org/10.1016/j.fuel.2023.127507

Li, Z., Liu, D., Cai, Y., Ranjith, P.G., Yao, Y., 2017. Multi-scale quantitative characterization of 3-D pore-fracture networks in bituminous and anthracite coals using FIB-SEM tomography and X-ray μ-CT. Fuel 209, 43–53. https://doi.org/10.1016/j.fuel.2017.07.088

Lin, W., Tang, G.-Q., Kovscek, A.R., 2008. Sorption-Induced Permeability Change of Coal During Gas-Injection Processes. SPE Reserv. Eval. Eng. 11, 792–802. https://doi.org/10.2118/109855-PA

Liu, A., Liu, S., Hou, X., Liu, P., 2020. Transient gas diffusivity evaluation and modeling for methane and helium in coal. Int. J. Heat Mass Transf. 159, 120091. https://doi.org/10.1016/j.ijheatmasstransfer.2020.120091

Liu, J., Chen, Z., Elsworth, D., Qu, H., Chen, D., 2011. Interactions of multiple processes during CBM extraction: A critical review. Int. J. Coal Geol. 87, 175–189. https://doi.org/10.1016/j.coal.2011.06.004

Liu, L., Luo, X.-B., Ding, L., Luo, S.-L., 2019. 4 - Application of Nanotechnology in the Removal of Heavy Metal From Water, in: Luo, X., Deng, F. (Eds.), Nanomaterials for the Removal of Pollutants and Resource Reutilization, Micro and Nano Technologies. Elsevier, pp. 83–147. https://doi.org/10.1016/B978-0-12-814837-2.00004-4

Liu, M., Mostaghimi, P., 2017. Pore-scale modelling of CO2 storage in fractured coal. Int. J. Greenh. Gas Control 66, 246–253. https://doi.org/10.1016/j.ijggc.2017.09.007

Lu, M., Connell, L.D., 2007. A model for the flow of gas mixtures in adsorption dominated dual porosity reservoirs incorporating multi-component matrix diffusion: Part I. Theoretical development. J. Pet. Sci. Eng. 59, 17–26. https://doi.org/10.1016/j.petrol.2007.02.004

Ma, T., Rutqvist, J., Oldenburg, C.M., Liu, W., 2017. Coupled thermal–hydrological–mechanical modeling of CO2-enhanced coalbed methane recovery. Int. J. Coal Geol. 179, 81–91. https://doi.org/10.1016/j.coal.2017.05.013

Majewska, Z., Majewski, S., Ziętek, J., 2010. Swelling of coal induced by cyclic sorption/desorption of gas: Experimental observations indicating changes in coal structure due to sorption of CO2 and CH4. Int. J. Coal Geol. 83, 475–483. https://doi.org/10.1016/j.coal.2010.07.001

Maradin, D., 2021. ADVANTAGES AND DISADVANTAGES OF RENEWABLE ENERGY SOURCES UTILIZATION. Int. J. Energy Econ. Policy 11, 176–183. https://doi.org/10.32479/ijeep.11027

Masoudian, M., 2013. Chemo-hydro-mechanical aspects of CO2 sequestration in deep coal seams.

Masoudian, M.S., Airey, D.W., El-Zein, A., 2014. A chemo-poro-mechanical model for sequestration of carbon dioxide in coalbeds, in: Bio- and Chemo-Mechanical Processes in Geotechnical Engineering, Conference Proceedings. ICE Publishing, pp. 81–89. https://doi.org/10.1680/bcmpge.60531.007

Mathews, J.P., Pone, J.D.N., Mitchell, G.D., Halleck, P., 2011. High-resolution X-ray computed tomography observations of the thermal drying of lump-sized subbituminous coal. Fuel Process. Technol. 92, 58–64. https://doi.org/10.1016/j.fuproc.2010.08.020

Mathias, S.A., Dentz, M., Liu, Q., 2020. Gas Diffusion in Coal Powders is a Multi-rate Process. Transp. Porous Media 131, 1037–1051. https://doi.org/10.1007/s11242-019-01376-x

Mavor, M.J., Gunter, W.D., 2006. Secondary Porosity and Permeability of Coal vs. Gas Composition and Pressure. SPE Reserv. Eval. Eng. 9, 114–125. https://doi.org/10.2118/90255-PA

McKee, C.R., Bumb, A.C., Koenig, R.A., 1988. Stress-Dependent Permeability and Porosity of Coal and Other Geologic Formations. SPE Form. Eval. 3, 81–91. https://doi.org/10.2118/12858-PA

Meakin, P., Tartakovsky, A.M., 2009. Modeling and simulation of pore-scale multiphase fluid flow and reactive transport in fractured and porous media. Rev. Geophys. 47. https://doi.org/10.1029/2008RG000263

Misra, V.N., Reddy, P.S.R., 2004. Mineral Characterisation and Processing. Allied Publishers.

Modeste, G., Diallo, M., Conin, M., Gunzburger, Y., 2022. Déplacements de surface dans le bassin houiller lorrain : reflets des exploitations passées et actuelles, in: 11èmes Journées Nationales de Géotechnique et de Géologie de l'ingénieur. Institut National des Sciences Appliquées de Lyon [INSA Lyon], CFMS, CFMR, CFGI, Lyon, France.

Moffat, D.H., Weale, K.E., 1955. Sorption by coal of methane at high pressures. Fuel 34, 449–462.

Moore, T.A., 2012. Coalbed methane: A review. Int. J. Coal Geol. 101, 36–81. https://doi.org/10.1016/j.coal.2012.05.011

Mostaghimi, P., Armstrong, R.T., Gerami, A., Hu, Y., Jing, Y., Kamali, F., Liu, M., Liu, Z., Lu, X., Ramandi, H.L., Zamani, A., Zhang, Y., 2017a. Cleat-scale characterisation of coal: An overview. J. Nat. Gas Sci. Eng. 39, 143–160. https://doi.org/10.1016/j.jngse.2017.01.025

Mostaghimi, P., Armstrong, R.T., Gerami, A., Hu, Y., Jing, Y., Kamali, F., Liu, M., Liu, Z., Lu, X., Ramandi, H.L., Zamani, A., Zhang, Y., 2017b. Cleat-scale characterisation of coal: An overview. J. Nat. Gas Sci. Eng. 39, 143–160. https://doi.org/10.1016/j.jngse.2017.01.025

Mostaghimi, P., Armstrong, R.T., Gerami, A., Hu, Y., Jing, Y., Kamali, F., Liu, M., Liu, Z., Lu, X., Ramandi, H.L., Zamani, A., Zhang, Y., 2016. Pore Scale Characterisation of Coal: An Unconventional Challenge. Presented at the Abu Dhabi International Petroleum Exhibition & Conference, OnePetro. https://doi.org/10.2118/183411-MS

Mushrif, S.H., Rey, A.D., 2009. An integrated model for adsorption-induced strain in microporous solids. Chem. Eng. Sci., Morton Denn Festschrift 64, 4744–4753. https://doi.org/10.1016/j.ces.2009.04.014

Nakase, H., Takeda, T., Oda, M., 1999. A simulation study on liquefaction using DEM. Presented at the Earthquake geotechnical engineering, pp. 637–642.

Nikoosokhan, S., Vandamme, M., Dangla, P., 2014. A poromechanical model for coal seams saturated with binary mixtures of CH4 and CO2. J. Mech. Phys. Solids 71, 97–111. https://doi.org/10.1016/j.jmps.2014.07.002

Ottiger, S., Pini, R., Storti, G., Mazzotti, M., 2008. Competitive adsorption equilibria of CO2 and CH4 on a dry coal. Adsorption 14, 539–556. https://doi.org/10.1007/s10450-008-9114-0

Palmer, I., 2010. Coalbed methane completions: A world view. Int. J. Coal Geol., Asia Pacific Coalbed Methane Symposium: Selected papers from the 2008 Brisbane symposium on coalbed methane and CO-enhanced coalbed methane 82, 184–195. https://doi.org/10.1016/j.coal.2009.12.010

Palmer, I., Mansoori, J., 1998. How Permeability Depends on Stress and Pore Pressure in Coalbeds: A New Model. SPE Reserv. Eval. Eng. 1, 539–544. https://doi.org/10.2118/52607-PA

Pan, C., Hilpert, M., Miller, C., 2004. Lattice-Boltzmann simulation of two-phase flow in porous media -. Water Resour. Res. - Wiley Online Libr. 40(1).

Pan, Z., Connell, L.D., 2007. A theoretical model for gas adsorption-induced coal swelling. Int. J. Coal Geol. 69, 243–252. https://doi.org/10.1016/j.coal.2006.04.006

Pan, Z., Connell, L.D., Camilleri, M., Connelly, L., 2010. Effects of matrix moisture on gas diffusion and flow in coal. Fuel 89, 3207–3217. https://doi.org/10.1016/j.fuel.2010.05.038

Papachristos, E., 2017. A 3D hydro-mechanical discrete element model for hydraulic fracturing in naturally fractured rock (phdthesis). Université Grenoble Alpes.

Papachristos, E., Scholtès, L., Donzé, F.V., Chareyre, B., 2017. Intensity and volumetric characterizations of hydraulically driven fractures by hydro-mechanical simulations. Int. J. Rock Mech. Min. Sci. 93, 163–178. https://doi.org/10.1016/j.ijrmms.2017.01.011

Pashin, J.C., 2014. Geology of North American Coalbed Methane Reservoirs, in: Coal Bed Methane. Elsevier, pp. 31–61. https://doi.org/10.1016/B978-0-12-800880-5.00003-6

Pattison, C.I., Fielding, C.R., McWatters, R.H., Hamilton, L.H., 1996. Nature and origin of fractures in Permian coals from the Bowen Basin, Queensland, Australia. Geol. Soc. Lond. Spec. Publ. 109, 133–150. https://doi.org/10.1144/GSL.SP.1996.109.01.10

Pekot, L.J., Reeves, S.R., 2003. Modeling the effects of matrix shrinkage and differential swelling on coalbed methane recovery and carbon sequestration. Proc. Int. Coalbed Methane Symp. Univ. Ala. 328.

Peng, Z., Liu, S., Tang, S., Zhao, Y., Li, Y., 2018. Multicomponent Lattice Boltzmann Simulations of Gas Transport in a Coal Reservoir with Dynamic Adsorption. Geofluids 2018, e5169010. https://doi.org/10.1155/2018/5169010

Perrier, L., Pijaudier-Cabot, G., Grégoire, D., 2018. Extended poromechanics for adsorption-induced swelling prediction in double porosity media: Modeling and experimental validation on activated carbon. Int. J. Solids Struct. 146, 192–202. https://doi.org/10.1016/j.ijsolstr.2018.03.029

Pijaudier-Cabot, G., Vermorel, R., Miqueu, C., Mendiboure, B., 2011. Revisiting poromechanics in the context of microporous materials. Comptes Rendus Mécanique 339, 770–778. https://doi.org/10.1016/j.crme.2011.09.003

Pini, R., Ottiger, S., Burlini, L., Storti, G., Mazzotti, M., 2009. Role of adsorption and swelling on the dynamics of gas injection in coal. J. Geophys. Res. Solid Earth 114. https://doi.org/10.1029/2008JB005961

Piri, M., Blunt, M.J., 2005. Three-dimensional mixed-wet random pore-scale network modeling of two- and three-phase flow in porous media. I. Model description. Phys. Rev. E 71, 026301. https://doi.org/10.1103/PhysRevE.71.026301

Pomeroy, C.D., Robinson, D.J., 1967. The effect of applied stresses on the permeability of a middle rank coal to water. Int. J. Rock Mech. Min. Sci. Geomech. Abstr. 4, 329–343. https://doi.org/10.1016/0148-9062(67)90014-9

Privalov, V., Pironon, J., de Donato, P., Michels, R., Morlot, C., Izart, A., 2020. Natural Fracture Systems in CBM Reservoirs of the Lorraine–Saar Coal Basin from the Standpoint of X-ray Computer Tomography. Environ. Sci. Proc. 5, 12. https://doi.org/10.3390/IECG2020-08772

Puri, R., Seidle, J.P., 1992. Measurement of stress-dependent permeability in coal and its influence on coalbed methane production. Situ U. S. 16:3.

Qu, H., Liu, J., Chen, Z., Wang, J., Pan, Z., Connell, L., Elsworth, D., 2012. Complex evolution of coal permeability during CO2 injection under variable temperatures. Int. J. Greenh. Gas Control 9, 281–293. https://doi.org/10.1016/j.ijggc.2012.04.003

Qu, H., Liu, J., Pan, Z., Connell, L., 2014. Impact of matrix swelling area propagation on the evolution of coal permeability under coupled multiple processes. J. Nat. Gas Sci. Eng. 18, 451–466. https://doi.org/10.1016/j.jngse.2014.04.007

Raoof, A., Hassanizadeh, S.M., Leijnse, A., 2010. Upscaling Transport of Adsorbing Solutes in Porous Media: Pore-Network ModelingAll rights reserved. No part of this periodical may be reproduced or transmitted in any form or by any means, electronic or mechanical, including photocopying, recording, or any information storage and retrieval system, without permission in writing from the publisher. Vadose Zone J. 9, 624–636. https://doi.org/10.2136/vzj2010.0026

Raoof, A., Nick, H.M., Hassanizadeh, S.M., Spiers, C.J., 2013. PoreFlow: A complex pore-network model for simulation of reactive transport in variably saturated porous media. Comput. Geosci. 61, 160–174. https://doi.org/10.1016/j.cageo.2013.08.005

Raoof, A., Nick, H.M., Wolterbeek, T.K.T., Spiers, C.J., 2012. Pore-scale modeling of reactive transport in wellbore cement under CO2 storage conditions. Int. J. Greenh. Gas Control, CATO: CCS Research in the Netherlands 11, S67–S77. https://doi.org/10.1016/j.ijggc.2012.09.012

Reinecke, S.A., Sleep, B.E., 2002. Knudsen diffusion, gas permeability, and water content in an unconsolidated porous medium. Water Resour. Res. 38, 16-1-16–15. https://doi.org/10.1029/2002WR001278

Reucroft, P.J., Patel, H., 1986. Gas-induced swelling in coal. Fuel 65, 816–820. https://doi.org/10.1016/0016-2361(86)90075-X

Riazi, M.R., Gupta, R., 2015. Coal Production and Processing Technology. CRC Press.

Ringel, M., 2006. Fostering the use of renewable energies in the European Union: the race between feed-in tariffs and green certificates. Renew. Energy 31, 1–17. https://doi.org/10.1016/j.renene.2005.03.015

Robertson, E.P., Christiansen, R.L., 2008. A Permeability Model for Coal and Other Fractured, Sorptive-Elastic Media. SPE J. 13, 314–324. https://doi.org/10.2118/104380-PA

Robertson, E. P., Christiansen, R.L., 2005. Modeling Permeability in Coal Using Sorption-Induced Strain Data. Presented at the SPE Annual Technical Conference and Exhibition, OnePetro. https://doi.org/10.2118/97068-MS

Robertson, Eric P., Christiansen, R.L., 2005. Measurement of Sorption-Induced Strain (No. INL/CON-05-00183). Idaho National Lab. (INL), Idaho Falls, ID (United States). https://doi.org/10.2172/911830

Sampath, K.H.S.M., Perera, M.S.A., Matthai, S.K., Ranjith, P.G., Dong-yin, L., 2020. Modelling of fully-coupled CO2 diffusion and adsorption-induced coal matrix swelling. Fuel 262, 116486. https://doi.org/10.1016/j.fuel.2019.116486

Satter, A., Iqbal, G.M., 2016. 22 - Unconventional gas reservoirs, in: Satter, A., Iqbal, G.M. (Eds.), Reservoir Engineering. Gulf Professional Publishing, Boston, pp. 389–425. https://doi.org/10.1016/B978-0-12-800219-3.00022-X

Sawyer, W.K., Paul, G.W., Schraufnagel, R.A., 1990. Development And Application Of A 3-D Coalbed Simulator. Presented at the Annual Technical Meeting, OnePetro. https://doi.org/10.2118/90-119

Scholtès, L., Chareyre, B., Michallet, H., Catalano, E., Marzougui, D., 2015. Modeling wave-induced pore pressure and effective stress in a granular seabed. Contin. Mech. Thermodyn. 27, 305–323. https://doi.org/10.1007/s00161-014-0377-2

Scholtès, L., Donzé, F.-V., 2013. A DEM model for soft and hard rocks: Role of grain interlocking on strength. J. Mech. Phys. Solids 61, 352–369. https://doi.org/10.1016/j.jmps.2012.10.005

Scholtès, L., Donzé, F.-V., 2012. Modelling progressive failure in fractured rock masses using a 3D discrete element method. Int. J. Rock Mech. Min. Sci. 52, 18–30. https://doi.org/10.1016/j.ijrmms.2012.02.009

Scholtès, L., Donzé, F.-V., Khanal, M., 2011. Scale effects on strength of geomaterials, case study: Coal. J. Mech. Phys. Solids 59, 1131–1146. https://doi.org/10.1016/j.jmps.2011.01.009

Schopf, J.M., 1960. Field description and sampling of coal beds. US Government Printing Office Washington, DC.

Scott, A.C., 1999. TAYLOR, G. H., TEICHMÜLLER, M., DAVIS, A., DIESSEL, C. F. K., LITTKE, R. & ROBERT, P. 1998. Organic Petrology. A New Handbook incorporating some revised parts of Stach's Textbook of Coal Petrology. xvi + 704 pp. Berlin, Stuttgart: Gebrüder Borntraeger. Price DM 196.00, US $116.00 (hard covers). ISBN 3 443 01036 9. Cambridge University Press.

Seidle, J.P., Huitt, L.G., 1995. Experimental Measurement of Coal Matrix Shrinkage Due to Gas Desorption and Implications for Cleat Permeability Increases. Presented at the International Meeting on Petroleum Engineering, OnePetro. https://doi.org/10.2118/30010-MS

Shi, J.Q., Durucan, S., 2004. Drawdown Induced Changes in Permeability of Coalbeds: A New Interpretation of the Reservoir Response to Primary Recovery. Transp. Porous Media 56, 1–16. https://doi.org/10.1023/B:TIPM.0000018398.19928.5a

Shi, J.Q., Durucan, S., 2003a. Changes in permeability of coalbeds during primary recovery–part 1: model formulation and analysis. Proc. 2003 Int. Coalbed Methane Symp. Univ. Ala. Tuscaloosa Ala. 341.

Shi, J.-Q., Durucan, S., Fujioka, M., 2008. A reservoir simulation study of CO2 injection and N2 flooding at the Ishikari coalfield CO2 storage pilot project, Japan. Int. J. Greenh. Gas Control 2, 47–57. https://doi.org/10.1016/S1750-5836(07)00112-0

Singh, P.K., Naik, A.S., 2015. Coal microscopy as a tool to understand the beneficiation problems of Indian Gondwana coals.

Šmilauer, V., Chareyre, B., Duriez, J., Eulitz, A., Gladky, A., Guo, N., Jakob, C., Kozicki, J., Kneib, F., Modenese, C., Stransky, J., Thoeni, K., 2015. Using and Programming. https://doi.org/10.5281/zenodo.34043

Somerton, W.H., SöylemezoǦlu, I.M., Dudley, R.C., 1975. Effect of stress on permeability of coal. Int. J. Rock Mech. Min. Sci. Geomech. Abstr. 12, 129–145. https://doi.org/10.1016/0148-9062(75)91244-9

St. George, J.D., Barakat, M.A., 2001. The change in effective stress associated with shrinkage from gas desorption in coal. Int. J. Coal Geol. 45, 105–113. https://doi.org/10.1016/S0166-5162(00)00026-4

Stevenson, M.D., Pinczewski, W.V., Somers, M.L., Bagio, S.E., 1991. Adsorption/Desorption of Multicomponent Gas Mixtures at In-Seam Conditions. Presented at the SPE Asia-Pacific Conference, OnePetro. https://doi.org/10.2118/23026-MS

Stopes, M.C., 1919. On the four visible ingredients in banded bituminous coal; studies in the composition of coal, No. 1. Proc. R. Soc. Lond. Ser. B Contain. Pap. Biol. Character 90, 470–487.

Sweijen, T., Chareyre, B., Hassanizadeh, S.M., Karadimitriou, N.K., 2017. Grain-scale modelling of swelling granular materials; application to super absorbent polymers. Powder Technol. 318, 411–422. https://doi.org/10.1016/j.powtec.2017.06.015

Tartakovsky, A.M., Meakin, P., Scheibe, T.D., Eichler West, R.M., 2007. Simulations of reactive transport and precipitation with smoothed particle hydrodynamics. J. Comput. Phys. 222, 654–672. https://doi.org/10.1016/j.jcp.2006.08.013

Tarumi, Y., 1988. A GRANULAR ASSEMBLY SIMULATION FOR THE DYNAMIC LIQUEFACTION OF SAND : Nat. Disaster Sci. 10, 45–59.

Thomas, L., 2002. Coal geology Wiley. John Sons Inc.

Thorstenson, D.C., Pollock, D.W., 1989. Gas transport in unsaturated zones: Multicomponent systems and the adequacy of Fick’s laws. Water Resour. Res. 25, 477–507. https://doi.org/10.1029/WR025i003p00477

Tinet, A.-J., Corlay, Q., Collon, P., Golfier, F., Kalo, K., 2020. Comparison of various 3D pore space reconstruction methods and implications on transport properties of nanoporous rocks. Adv. Water Resour. 141, 103615. https://doi.org/10.1016/j.advwatres.2020.103615

Ting, F.T.C., 1977. Origin and Spacing of Cleats in Coal Beds. J. Press. Vessel Technol. 99, 624–626. https://doi.org/10.1115/1.3454584

U.S. Energy information administration, 2010. "Annual Energy Outlook 2010 with Projections to 2035.

Ustinov, E.A., Do, D.D., 2006. Effect of adsorption deformation on thermodynamic characteristics of a fluid in slit pores at sub-critical conditions. Carbon 44, 2652–2663. https://doi.org/10.1016/j.carbon.2006.04.015

Vamvuka, D., Troulinos, S., Kastanaki, E., 2006. The effect of mineral matter on the physical and chemical activation of low rank coal and biomass materials. Fuel 85, 1763–1771. https://doi.org/10.1016/j.fuel.2006.03.005

Vandamme, M., Brochard, L., Lecampion, B., Coussy, O., 2010. Adsorption and strain: The CO2-induced swelling of coal. J. Mech. Phys. Solids 58, 1489–1505. https://doi.org/10.1016/j.jmps.2010.07.014

Vermorel, R., Pijaudier-Cabot, G., 2014. Enhanced continuum poromechanics to account for adsorption induced swelling of saturated isotropic microporous materials. Eur. J. Mech. - ASolids 44, 148–156. https://doi.org/10.1016/j.euromechsol.2013.10.010

Wang, S., Elsworth, D., Liu, J., 2011. Permeability evolution in fractured coal: The roles of fracture geometry and water-content. Int. J. Coal Geol. 87, 13–25. https://doi.org/10.1016/j.coal.2011.04.009

Wang, Z., Cheng, Y., Zhang, K., Hao, C., Wang, L., Li, W., Hu, B., 2018. Characteristics of microscopic pore structure and fractal dimension of bituminous coal by cyclic gas adsorption/desorption: An experimental study. Fuel 232, 495–505. https://doi.org/10.1016/j.fuel.2018.06.004

Ward, C.R., 2002. Analysis and significance of mineral matter in coal seams. Int. J. Coal Geol., Volume 50 50, 135–168. https://doi.org/10.1016/S0166-5162(02)00117-9

Ward, C.R., Suárez-Ruiz, I., 2008. Chapter 1 - Introduction to Applied Coal Petrology, in: Suárez-Ruiz, I., Crelling, J.C. (Eds.), Applied Coal Petrology. Elsevier, Burlington, pp. 1–18. https://doi.org/10.1016/B978-0-08-045051-3.00001-4

Warren, J.E., Root, P.J., 1963. The Behavior of Naturally Fractured Reservoirs. Soc. Pet. Eng. J. 3, 245–255. https://doi.org/10.2118/426-PA

Warwick, P.D., 2005. Coal Systems Analysis. Geological Society of America. https://doi.org/10.1130/SPE387

Wei, X., Massarotto, P., Wang, G., Rudolph, V., Golding, S.D., 2010. CO2 sequestration in coals and enhanced coalbed methane recovery: New numerical approach. Fuel 89, 1110–1118. https://doi.org/10.1016/j.fuel.2010.01.024

Wei, Z., Zhang, D., 2010. Coupled fluid-flow and geomechanics for triple-porosity/dual-permeability modeling of coalbed methane recovery. Int. J. Rock Mech. Min. Sci. 47, 1242–1253. https://doi.org/10.1016/j.ijrmms.2010.08.020

Winschel, R.A., 1990. The Relationship of Carbon Dioxide Emissions with Coal Rank and Sulfur Content. J. Air Waste Manag. Assoc. 40, 861–865. https://doi.org/10.1080/10473289.1990.10466730

Wu, Y., Liu, J., Elsworth, D., Chen, Z., Connell, L., Pan, Z., 2010. Dual poroelastic response of a coal seam to CO2 injection. Int. J. Greenh. Gas Control 4, 668–678. https://doi.org/10.1016/j.ijggc.2010.02.004

Xu, R., Prodanović, M., 2018. Effect of pore geometry on nitrogen sorption isotherms interpretation: A pore network modeling study. Fuel 225, 243–255. https://doi.org/10.1016/j.fuel.2018.03.143

Yang, K., Lu, X., Lin, Y., Neimark, A.V., 2010. Deformation of Coal Induced by Methane Adsorption at Geological Conditions. Energy Fuels 24, 5955–5964. https://doi.org/10.1021/ef100769x

Youjun, J., Vafai, K., 2017. Analysis of pore scale fluid migration in a porous medium-application to coal rock seam. Int. J. Numer. Methods Heat Fluid Flow 27, 1706–1719. https://doi.org/10.1108/HFF-05-2016-0198

Yuan, C., Chareyre, B., 2017. A pore-scale method for hydromechanical coupling in deformable granular media. Comput. Methods Appl. Mech. Eng. 318, 1066–1079. https://doi.org/10.1016/j.cma.2017.02.024

Zhang, J., Standifird, W.B., Roegiers, J.-C., Zhang, Y., 2007. Stress-Dependent Fluid Flow and Permeability in Fractured Media: from Lab Experiments to Engineering Applications. Rock Mech. Rock Eng. 40, 3–21. https://doi.org/10.1007/s00603-006-0103-x

Zhang, Y., Xu, X., Lebedev, M., Sarmadivaleh, M., Barifcani, A., Iglauer, S., 2016. Multi-scale x-ray computed tomography analysis of coal microstructure and permeability changes as a function of effective stress. Int. J. Coal Geol. 165, 149–156. https://doi.org/10.1016/j.coal.2016.08.016

Zhao, Y., Wang, Z., 2019. Multi-scale analysis on coal permeability using the lattice Boltzmann method. J. Pet. Sci. Eng. 174, 1269–1278. https://doi.org/10.1016/j.petrol.2018.11.029

Zimmerman, R.W., Bodvarsson, G.S., 1996. Hydraulic conductivity of rock fractures. Transp. Porous Media 23, 1–30. https://doi.org/10.1007/BF00145263

Zutshi, A., Harpalani, S., 2004. MATRIX SWELLING WITH CO2 INJECTION IN A CBM RESERVOIR AND ITS IMPACT ON PERMEABILITY OF COAL.